2013

Study Regarding Properties of Solid Tumors in Mammals

Long Jian Liu
University of Windsor

Study Regarding Properties of Solid Tumors in Mammals

by

Long Jian Liu

A Dissertation
Submitted to the Faculty of Graduate Studies
through the Department of Physics
in Partial Fulfillment of the Requirements for
the Degree of Doctor of Philosophy at the
University of Windsor

Windsor, Ontario, Canada
2012

Library and Archives Canada

Published Heritage Branch

395 Wellington Street
Ottawa ON K1A 0N4
Canada

Bibliothèque et Archives Canada

Direction du Patrimoine de l'édition

395, rue Wellington
Ottawa ON K1A 0N4
Canada

Your file Votre référence
ISBN: 978-0-494-79145-5

Our file Notre référence
ISBN: 978-0-494-79145-5

“Study Regarding Properties of Solid Tumors in Mammals”

by

Mr. Long Jian Liu

APPROVED BY:

_____

Dr. Mordechay Schlesinger
Supervisor Physics

_____

Dr. Wladyslaw Kedzierski
Internal Program Reader Physics

_____

Dr. Steven Rehse
Internal Program Reader

_____

Dr. Siyaram Pandey
External Program Reader

_____

Dr. J. Carl Kumaradas
External examiner Ryerson University

_____

Dr. Dave Bussiere
Chair

October 23rd, 2012

Declaration of Co-Authorship

I. Co-Authorship Declaration

I hereby declare that this dissertation incorporates material that is result of joint research, as follows: This dissertation also incorporates the outcome of a joint research undertaken in collaboration with Dr. S. L. Brown and Dr. J. R. Ewing under the supervision of professor M. Schlesinger. The collaboration is covered in Chapter 4 of the dissertation. In all cases, the key ideas, primary contributions, experimental designs, data analysis and interpretation, were performed by the author, and the contribution of co-authors was primarily through the provision of advice when needed.

I am aware of the University of Windsor Senate Policy on Authorship and I certify that I have properly acknowledged the contribution of other researchers to my dissertation, and have obtained written permission from each of the co-author(s) to include the above material(s) in my dissertation.

I certify that, with the above qualification, this dissertation, and the research to which it refers, is the product of my own work.

I declare that this is a true copy of my dissertation, including any final revisions, as approved by my dissertation committee and the Graduate Studies office, and that this dissertation has not been submitted for a higher degree to any other University or Institution.

Abstract

Based on the mass balance (conservation) equation and the ubiquitous ¼ power law in biological allometry, we derive a general governing equation for organism growth. It is the same as a previously published model by West et al., which was developed using a conservation of total energy formalism with respect to the maintenance of already existing tissue and newly created one. In the present model, the energy/nutrition (including oxygen) supply or consumption in metabolism is reflected in the production and death rates. We start by dividing an organism into different small systems which have identical cells and then unite them by introducing similarity of growth. Normal cells follow the rules for similarity of growth but tumor cells may not. This model is applied to tumor therapy. We model the response of tumor cells to the major standard tumor treatments: surgery, radiation and chemotherapy. This model explains the survival curves quite well (better than all previous models). Also, it consistently explains cell response to high and low LET (linear energy transfer) radiations. This work shows that the LQ model is an approximate result of the present model under specific conditions.

Tumor interstitial fluid pressure (TIFP) has the potential to predict tumor response to non-surgical cancer treatments such as radiation and chemotherapies. We present the mathematical framework for a quantitative, non-invasive measure of TIFP. It describes the distribution of interstitial fluid pressure in three distinct tumor regions: vascularized tumor rim, central tumor region and normal tissue. We demonstrate that the acquisition of serial images of a tumor after the injection of a contrast agent can provide a non-invasive and potentially quantitative measure of TIFP.

Keywords: organism growth, tumor growth, tumor therapy, high and low LET radiations, surviving fraction, the LQ model, tumor interstitial fluid pressure (TIFP), non-invasive measurement.

Dedication

To my wife, Songzhu Wang, and my daughter, Xinyu Liu. Thank you
for supporting, inspiring and understanding me
in this journey of my life.

Acknowledgements

There are a number of individuals without whom this dissertation would not have been possible. I would like to acknowledge their support and contributions here.

First and foremost, I would like to give my utmost thanks to my advisor and mentor Dr. Mordechay Schlesinger, for his suggestions, patience and care. His academic spirits and interests inspired me throughout my master and Ph. D study programs. I will benefit from his guidance my entire life.

I would like to express my sincere gratitude and deepest appreciation to Dr. Stephen L. Brown from Henry Ford Hospital. His support provides me with an opportunity to engage in some interesting and practical researches in medical physics. His expertise in this field has increased my knowledge.

I owe a special debt of gratitude to Dr. J. R. Ewing, from Henry Ford Hospital, for proving the experimental results on the noninvasive measurement of tumor interstitial fluid pressure (TIFP), which clearly show that the model has the potential for clinical applications.

I would also like to thank my family for their support, encouragement and understanding. They have provided me with an ideal environment, allowing me to concentrate on my work.

Last but not least, I would like to thank my committee members: external examiner Dr. Kumaradas, external reader Dr. Pandey, internal readers Dr. Kedzierski and Dr. Rehse, and committee chair Dr. Bussiere.

Contents

List of Symbols

TIFP—tumor interstitial fluid pressure

LQ—linear-quadratic

LQL—linear-quadratic linear

LPL—lethal and potentially lethal

SF—surviving fraction

α and β are two constants which determine cell response to specific radiation

ADRM—adriamycin

p_v—vascular fluid pressure

π_v—osmotic pressure of the plasma

π—osmotic pressure of interstitial fluid

L—hydraulic conductivity of blood vessels

p_0—tumor pressure barrier

p_∞—the pressure of environment

r_n—radius of the necrotic core

r_0—radius corresponding to pressure barrier p_0

M—asymptotic mass of a cell system

m_0—initial mass of the cell system

$\overline{S}$ — cell production rate (the number of cells produced in a unit volume in unit time)

E— cell death rate (the number of cells died in a unit volume in unit time)

$\overline{K}$ — additional death rate (the number of cells killed in a unit volume in unit time)

C—number density of cells

CHO—Chinese hamster ovary

BLM—bleomycin

ECT—electrochemotherapy

MRI—magnetic resonance imaging

Q_m—maximum fluid drainage of a tumor

Q_c—critical flow rate of a tumor

Chapter 1. Introduction

Tumors are defined as abnormal growth of body tissue. They are life-threatening if they evolve into cancer. Malignant tumors (cancer) are the major cause of premature death in the Western World. They account for 29% of male and 25% of female deaths [1]. If we understand the properties of tumors, their development mechanisms, and their response to treatment, we may predict their growth process and find an efficient therapy for treatment before they evolve into cancer. Modelling is a widely used method in tumor research. It has been applied to tumor growth and metastasis, tumor prognosis, tumor therapy and treatment as well as the corresponding response of tumor cells. Based on our experience of modelling corrosion of magnesium and its alloys, we feel that the governing equation for corrosion might be adopted to describe the process of tumor growth and metastasis. For instance, a diffusion-reaction equation is often used in corrosion modelling. It is also used in tumor research, such as in modelling avascular tumor growth. If we take tumor cell production as the source, tumor cell death as the sink/drain, and tumor cell transport in metastasis as the flux, the idea of the diffusion-reaction equation may be applied to describe the process of tumor growth and metastasis. Tumor interstitial fluid pressure (TIFP) is an important factor in tumor prognosis. It is an early marker of tumor response to therapy and can be practically used to monitor the effect of a specific treatment. Similarly, considering the source and drain of tumor fluid, as well as its transport process, we may use the diffusion-reaction equation to find the distribution of TIFP in a tumor and its interface with normal tissue. This dissertation contains two aspects of tumor study: 1) A general model for describing tumor growth and response to therapies and a discussion of tumor metastasis. 2) A phenomenological model for describing TIFP formation, distribution, as well as a possible noninvasive determination and measurement thereof.

Literally, the word *tumor* originates from Latin and means “swelling” though not all swellings are tumors [2]. Generally, a tumor is an abnormal growth of body tissue, which can be malignant (cancerous) or benign (noncancerous). Cell division is strictly

controlled in normal tissue, as Hershey pointed out: “New cells are created to replace older ones or to perform new functions. Cells that are damaged or no longer needed die to make room for healthy replacements [3].” When cells divide excessively in the body, the balance of cell division and death is disturbed, and a tumor occurs [3]. A tumor has properties of an organism with characteristics such as growth and metastasis. When a tumor grows to a certain stage, tumor cells leave the original organ or part and spread to another non-adjacent organ or part through blood vessels and the lymphatic system.

Researchers in the field of oncology apply experimental techniques and theoretical approaches in the ongoing battle against cancer. They try to understand its mechanisms and principles and establish a mathematical model to quantitatively determine the process of tumor growth, metastasis and response to treatment, as well as tumor prognosis. However, tumor types and locations vary. They have their own properties and characteristics. Many new therapies and strategies are expected to improve and individualize treatment. Thus, modelling is a viable theoretical approach when money, time and energy are limited. Araujo pointed out: “The study of tumor growth and the development of anti-cancer therapies are most worthwhile pursuits, having significant potential to enhance quality of life and increase life-expectancies, which may, in turn, yield considerable economic and social benefits.” [1]

Despite remarkable strides in the treatment of some solid cancers such as breast and prostate, many cancers remain resistant to treatment. As new therapies are developed and medications become increasingly individualized, a need exists for effective prognostic markers of response. Tumor interstitial fluid pressure, TIFP, is a physiological parameter with demonstrated prognostic value. However, its clinical use is limited at present because the techniques available for its measurement are invasive and provide only point-measurements. Methods to detect it by noninvasive means are a popular topic which has attracted many researchers’ attention. If we understand its formation and distribution, we may actualize noninvasive detection and monitor the treatment response process. Then we will have found an efficient treatment strategy.

In summary, tumor studies include the law of tumor growth and metastasis, the responses to tumor treatments and therapies, and connecting tumor interstitial fluid pressure (TIFP)

distribution and non-invasive detecting to improve clinical tumor prognosis. If we can quantitatively determine and predict the process of tumor growth and metastasis, its properties in different stages, and its response to therapy, we may make a prognosis and treat it efficiently. Also, this can benefit the patients the most.

1.1 General Background

1.1.1 Tumor Growth

There are many different models of tumor growth. Here, we introduce some that are widely used in tumor study. Laird [4] first applied the Gompertzian equation to describe tumor growth empirically or phenomenologically (details are given in chapter 2). Subsequently, Lair et al. [5] applied this equation to describe the normal growth of an organism. Since then, Gompertzian equation has been used as an empiric model to explain the growth process of tumors and normal tissues both for theoretical and experimental studies. However, it is noted that the Gompertzian model may cause the proliferation rate of the cellular population to be unbounded, which does not represent that the proliferation rate of the cellular population is ultimately bounded by cell division time [6-8]. Steel [7] and Wheldon [8] noted that Gompertz's function might not be suitable for describing the growth of a small sized tumor. Actually, many mathematical models for tumor growth are derived from a reaction-diffusion differential equation. For many solid tumors, there is a necrotic core where most cells are dead and there are no functional exchange vessels. By viewing a large number of human bronchial cancer samples, Thomlinson and Gray [9] found that the necrotic core enlarges when the tumor cord, the fundamental microarchitectures of solid tumors consisting of a microvessel nourishing nearby tumor cells, grows larger since the distance for oxygen diffusion is limited. Therefore, the thickness of the sheath of viable tumor cells remains nearly constant [10]. Based on experimental investigation, Thomlinson and Gray presented a mathematical model of the diffusion and consumption of oxygen [9]. Burton [11]

developed this model by considering both the distribution of oxygen in a spherical tumor and the "relative radius of the central zone to the total radius" [1]. To explain the existence of a steady-state tumor size, Greenspan [12] extended these models by considering that "a surface tension among the living cancer cells in order to maintain a compact, solid mass" and that "necrotic cellular debris continually disintegrates into simpler chemical compounds that are freely permeable through cell membranes" [1]. However, these models are limited to avascular solid tumors whose nutrition and oxygen are diffused from the stroma. The modeling of avascular tumors is just the first step toward building models for fully vascularised tumors since there are three distinct stages (avascular, vascular, and metastatic) to cancer development [13]. Later, many other models were developed by modifying or extending Greenspan's model. Some new models based on the diffusion-reaction differential equation and mass balance equation also exist [12-21]. In addition, many other empiric and phenomenological models are presented based on random onset and statistics [20-27], as well as curve fittings and experimental data analysis [28-31]. However, all these kinds of models can only qualitatively reflect the process of tumor growth with three distinct phases: "an initial exponential growth phase, followed by some degree of retardation, culminating in a final phase where retardation by both mitotic inhibition and cell death ultimately gave rise to dormancy" [1]. This may explain why the Gompertz function is still an option for describing tumor growth in some cases at present. Based on the conservation of total energy formalism with respect to the maintenance of already existing tissues and newly created ones, and Kleiber law [32] (which is a fundamental biological law), West et al. [33] presented a general model for an organism's growth (details are given in chapter 2). This model seems to provide a universal growth law: mammals, birds, fish, molluscs and even their tumors all follow this growth law. Guiot et al. [34] applied this model to fit some data collected, both in vitro and in vivo, from literature for tumor growth and found that tumor growth also follows this seemingly universal law. Even the growth curves for some small tumors such as 9L and U118 fit West's model very well.

Metastasis means "displacement" in Greek and is now defined as the transfer of disease from one organ or part to another that is not directly connected to it [35]. It is clear that tumor metastasis includes several processes: tumor cell motility/invasiveness,

intravasation, transit in the blood or lymph, extravasation and growth at a new site [36]. The quantitative study of tumor metastasis is different from the study of solid tumor growth in that it is less intensive and comes later both in experiment and theory. Liotta et al. developed an experimental model to quantify some of the major processes initiated by tumor transplantation and culmination in pulmonary metastasis in 1974 [37]. They confirmed the observations in their later study [38]. However, the mechanics of metastasis is still not clear. The primary clinical challenge is that metastasis is unpredictable at the onset. Also, because of its resistance to therapy, metastasis is the major cause of death from cancer [35]. Most models are qualitative. There are few quantitative mathematical models to express the process and mechanics of metastasis since the process is complicated and there are many uncertain factors that enhance the difficulty for quantitative studies.

1.1.2 Tumor Therapies and Cell Survival Response

The three standard therapies in widespread clinical use that are designed to decrease the growth of a tumor are surgery (removing tumor cells and decreasing tumor mass immediately), radiation therapy (killing tumor cells by using ionizing radiation such as x-ray, γ-ray, α-particles and neutrons), and conventional chemotherapy (killing rapidly dividing tumor cells by using chemotherapeutic agents). In addition, antiangiogenic therapy (including metronomic chemotherapy) has gained acceptance in recent years. Surgery is effective and the best therapy for a tumor in its early stage if it is detected in time. For a late stage tumor, especially for metastases, radiation and chemotherapy are effective options, as well as a combination of the two. Relative to conventional chemotherapy, antiangiogenic therapy is promising since it works with fewer toxins.

Surgery removes the majority of the tumor, but depending on the aggressiveness of the cancer, proximity of critical normal tissue, and skill of the surgeon, some tumor cells may remain. Radiation therapy and conventional chemotherapy kill tumor cells, though they

also harm normal cells. Destroying cancer cells via radiation is a stochastic process and the rate of cell death is dependent on the number of cells present. Conventional chemotherapy also kills cells randomly, but cells closer to a blood vessel will be preferentially affected since this kind of therapy targets rapidly dividing cells. Antiangiogenic therapy targets the supplying vasculature, starving the tumor. Antiangiogenic agents prohibit the growth of new blood vessels, so some cancer cells will be unaffected. It is generally accepted that when the doses of conventional chemotherapy are very low, tumor cells are not killed directly. However, the doses are high enough to reduce the growth of new capillaries that will supply nutrition to the tumor.

Often these four therapies are administered in combination. How to optimally combine therapies is still being debated [39] and more study is required.

The effects of therapies/treatments are reflected by cell responses. Ionizing radiations in all their forms are powerful methods used in biology and medicine, especially in cancer and tumor treatment. Generally, the survival curves of cells under radiation possess a characteristic curvature in the initial low dose region and show an almost linear relationship in the high dose region. The width of the curvature varies in different cases. For fitting or explaining experimental data, models like the linear-quadratic (LQ) model [10,40-43], the linear-quadratic linear (LQL) model [40, 44] and the lethal-potentially lethal (LPL) model [44, 45] have been presented and studied (see chapter 2 for details).

The LQ model is widely used and is expressed as $SF = \exp[-(\alpha D + \beta D^2)]$ [10, 40-43] (where SF stands for cell surviving fraction, D is the radiation dose, α and β are constants determined by cell response). However, many researchers noted that the LQ model does not fit the survival curves well, especially in the high dose region [40-45]. Astrahan [40] showed that the survival response for Chinese hamster cells in culture [40,46] does not fit the LQ model in the high dose region (D>7Gy), while Human HeLa cells in culture [10, 40] and DU145 cells in *vitro* [40,42,47,48] do not fit in even the low dose regions (D>2Gy). Garcia et al. [42] studied the behaviour of α, β and α/β in different dose regions by dividing the survival curves into three regions: 1) low-dose

region (LR), 2) linear quadratic or middle dose region (LQR), and 3) high-dose region (HR). These regions in terms of Gy are different for various cells. The conclusion reached is that the constants α, β, and thus α/β, have different values in different regions, which suggests that the LQ model fits the survival curves in the middle dose region but not in the low and high dose regions. They indicated that the mechanism for cell survival in the low dose region might deviate from the LQ model. Thus, some phenomenological models have been suggested for improving the model's ability to reflect cell response to dose regions. Astrahan modified the LQ model phenomenologically and presented an LQ-L model [40]. This empiric model does fit some experimental data but only to an extent. However, it cannot fit the Human HeLa and DU145 cell survival curves in some dose regions, especially for DU145 cells (we will show those details in section 3). Also, the LQ-L model cannot be applied to the survival curves for EMT-6/Ro tumors under aerobic conditions [49]. Guerrero and Carlone [44] analysed the advantages and disadvantages of other models and modified an LQL model by considering a mechanistic formulation in the case of split-dose experiments and exponentially decaying sources (which is compatible with the LQL model). They compared their LQL model with the LPL and LQ models theoretically, and demonstrated better results relative to other models. However, they did not use their model to fit any survival curves directly. Actually, based on five complicated assumptions and three constrained characteristics, the LPL model itself is also a phenomenological model because of the variables and functions chosen for setting up the differential equations [45]. In fact, the initial nonzero slope might not be satisfied. Also, we do not know if the slope of the survival curve is a constant in the extremely high dose region.

Some models for the response of mixed cell populations [50-53] fit the experimental data rather well, though they are empiric models. Skarsgard et al. [50] found that a two-population LQ model (see eq. 2.12 in chapter 2 for details) gave the best fit. Their laboratory studies demonstrated the presence of two types of substructure in the radiation survival response of cultured mammalian cells [52]. However, there are no constraints upon the α and β (or α/β) of different cell populations. This may cause the parameters to be redundant and the number of choices to be greater than one set--αs and βs, as well as

cell fractions *f*s--for the same survival response [50]. Powers and Tolmach [10, 54] reported radiation response in cell populations, which were constituted of solid, subcutaneous 6C3HED mouse lymphosarcomas. Survival is found to follow a multicomponent exponential curve. The results suggested that the survival kinetics were determined mainly by cells of only two sensitivities. Even so, no existing models fit the survival curve, including the two-population LQ model.

It is accepted by many researchers that the effect of radiation are limited by some "radioresistant" cells, such as cancer stem cells [55, 56] and hypoxic/anoxic cells in tumors [41]. Rich [55] and Diehn et al. [56] showed that cancer stem cells are more resistant to radiation than other cancer cells. The partial oxygen pressure in tumor cells is also a parameter that determines response to radiation. There is a subpopulation of tumor cells that exist at low oxygen environment. They are 2 to 3 times more resistant to the damaging effects of radiation than well-oxygenated cells. Acutely hypoxic cells caused by transient flow of blood through vessels also form a resistant subpopulation. These hypoxic cells have their own response to radiation. Wouters and Brown [41] noticed that the hypoxic fraction of cells drastically affects the radiation response. A small fraction of a mixture of hypoxic cells can change the survival curves significantly.

Though chemotherapy has successfully been used clinically and many experiments have been performed, there are relatively few theoretical models for actual response. The survival response of mammalian cells is diverse and complicated since it is strongly dependent on chemotherapeutic agents. Bleomycin and actinomycin D cause a rapid drop in the surviving fraction, which gradually slows down to a linear line with the increase of the agents' doses/concentrations [10,57-59], whereas BCNU, MeCCNU, and PCNU, etc., (see appendix 1 for introduction of these anticancer drugs) cause a survival response similar to that of radiation [10,57,60]. However, Adriamycin shows a different response curve, which combines the features of cell responses to actinomycin D and BCNU [61]. We also investigated the survival responses to some other chemotherapeutic agents and chemotherapies [62-64]. In summary, most survival responses can be divided into three types: (1) the survival response possesses features similar to that caused by bleomycin, as shown in Fig. 1-1(a); (2) the survival response is similar to that caused by BCNU,

demonstrated in Fig. 1-1(b); (3) the survival response possesses features of (1) and (2) in combination, as shown in Fig. 1-1(c).

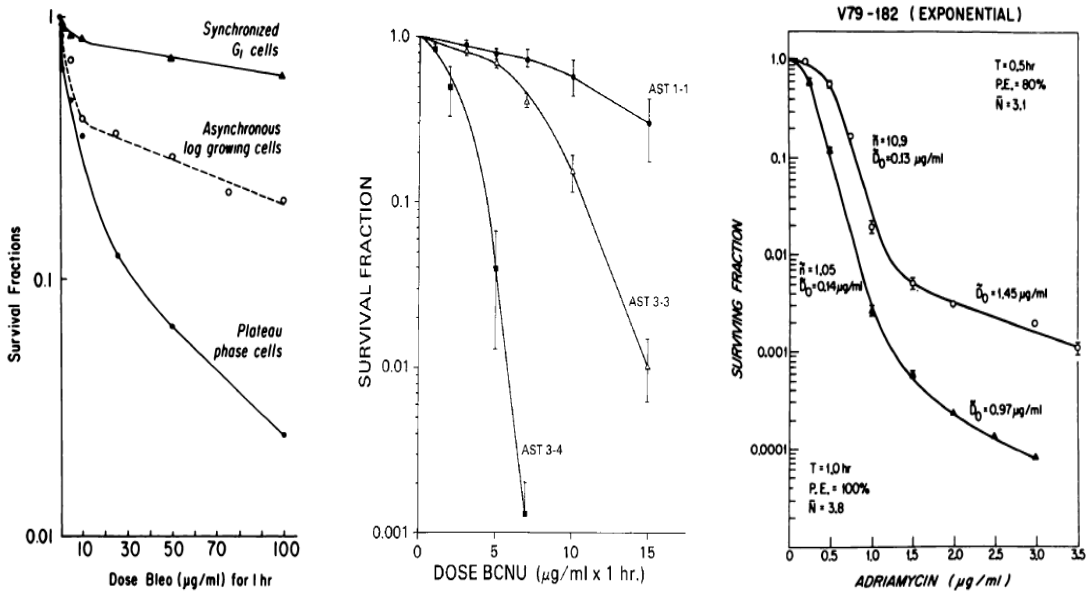

(a) Bleomycin [57] (b) BCNU [60] (c) ADRM [61]

Fig. 1.1 Cell responses to three typical chemotherapeutic agents

For survival response to chemotherapy, the Hill-type model is often applied, in which the surviving fraction is expressed as $SF=1/(1+Ax^m)$, where x is a measure of cellular damage, m and A are constants [65]. Another choice is the exponential kill model [65]. El-Kareh and Secomb [66, 67] presented a model that combined the sigmoidal model with the Hill-type model. It may be the model that fits for experimental data best (more details will be given in chapter 2). However, one can tell that by observing the curves, many experimental data do not fit the model well. Also, this model does not fit cases (1) and (2), which were mentioned above. Compared with cell response to radiation, we assume there are also two kinds of "killing" mechanisms for chemotherapy: one is a "single event killing," the other is a "double event killing," which inactivates cell proliferation by damaging DNA (similar to radiation).

Similar to radiation response, studies [68-71] found that there is a small cell population that is more resistant to chemotherapy than other populations. Awad et al. [68] and Liu et al. [69] showed that some cancer stem cells are more resistant to chemotherapy than other cells. It is established [70, 71] that hypoxic tumor cells are also more resistant to chemotherapy. These effects may lead us to discern the mechanism of cell response to radiation and chemotherapy.

1.1.3 Tumor Interstitial Fluid Pressure and Tumor Prognosis

TIFP is an important parameter in tumor prognosis, therapy and treatment, drug delivery, and tumor metastasis [72-78]. Rofstad et al. [76] showed that radiation resistance may be associated with high TIFP. Ferretti et al. [73] observed the relationship between TIFP and the response to chemotherapy. It is established that TIFP originates mainly from fluid accumulation because of the increase in the capillary permeability and impaired lymphatic drainage in the tumor area. Interstitial fluid pressure (IFP) is elevated in tumors due to abnormal structure and the function of blood and lymphatic vessels [79]. Generally, tumor blood vessels are leaky, while lymphatics are malfunctional in a tumor and enlarged at the tumor's periphery. A high IFP results from leaky vessels, which lack permselectivity (restriction of permeation) and are unable to sustain the hydrostatic and oncotic pressure gradients across the vessel wall. Baxter and Jain [80] presented a model (details are given in chapter 2) to express the transportation of fluid and the distribution of tumor pressure based on Starling's law [72,80], (which connects TIFP p; the surface area A of the blood vessels; the vascular fluid pressure p_v; the osmotic pressure difference $\pi_v - \pi$, between the plasma in the blood vessels and interstitial fluid; the osmotic reflection coefficient σ; the hydraulic conductivity L of the blood vessel [72]), which is adopted to explain the effect of capillary-capillary interaction; and Darcy's law [72, 80], which reflects the porous tissue condition and states that the fluid velocity is proportional to the negative gradient of TIFP. Boucher et al. [81] measured TIFP distribution in tissue-

isolated and subcutaneous tumors to support this model. Jain et al. [82] applied this model to study the "effect of vascular normalization by antiangiogenic therapy on interstitial hypertension, peritumor edema, and lymphatic metastasis". Experiments and theoretical analysis [79-85] report that IFP is uniform throughout the central area of the tumor. There is a steep gradient of IFP in the peripheral area. Baxter and Jain [80] studied two cases. The first was an isolated tumor, where the enhanced TIFP is limited to the tumor. In the special case of an isolated tumor, the TIFP at the periphery rapidly decreases to zero (atmospheric level) or the pressure of the environment. The second was an embedded tumor (enclosed by normal tissue). In this more common situation, the raised TIFP extends beyond the tumor radius into the normal tissues before equilibrating to zero (relative to atmosphere), or the pressure of the environment. The schematic is shown in Fig. 1.2. Here, R represents the radius of a tumor, p_0 is the tumor IFP (TIFP) in the central area and p_∞ is the pressure of the environment (the IFP of normal tissue).

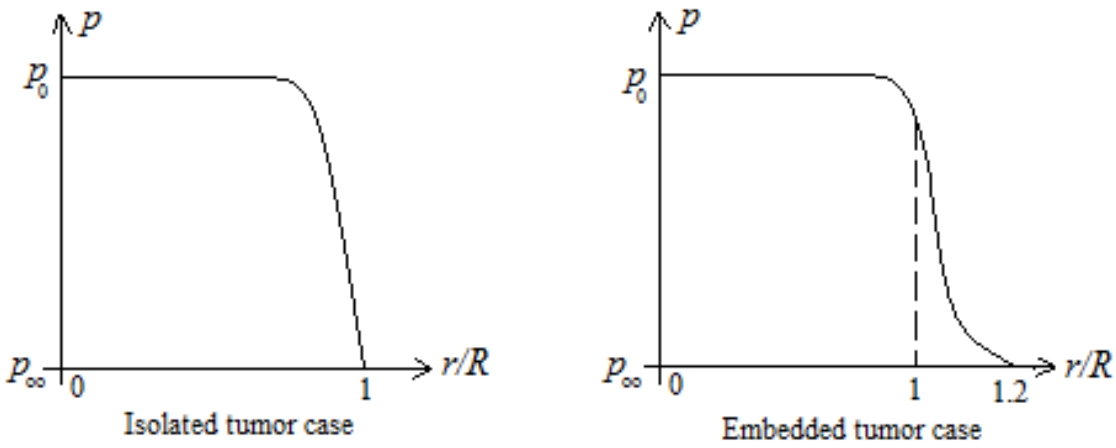

Fig. 1.2 Schematics of tumor interstitial fluid pressure distribution [72]

The factors that lead to an elevated TIFP are known. Although it is recruited from normal vasculature by tumor pro-angiogenic factors, tumor vasculature is abnormal. Tumor microvasculature generally lacks pericytes and is often associated with a damaged basal lamina. Its morphology is usually tortuous, dilated, and saccular. Tumor microvessels are

longer, larger in diameter, and denser than normal microvessels. Importantly, tumor microvessels are generally much more permeable to blood proteins, with all of the mechanisms for transvascular leakage of blood proteins being evidenced, including enlarged fenestrae at the endothelial junctions, and increased vesicular transport. A leakage of proteins, with its corollary decrease in osmotic pressure, an increased blood supply, with its potential for increased vascular pressure, and the general lack of a competent lymphatic system, all contribute to an increased TIFP. This, in turn, collapses the microvasculature, leading to flow that, despite the proliferation of blood vessels, is limited by the TIFP via the Starling effect. As the tumor grows, these factors limit the flow of metabolites to the tumor center, eventually resulting in a necrotic core surrounded by a perfused and growing rim with an elevated interstitial pressure that drops sharply past the boundary of the tumor. However, in the boundary region, the increased interstitial fluid leads to a local ischemia, and a consequent release of the vascular endothelial growth factor (VEGF, a signal protein produced by cells, stimulates the growth of new blood vessels), recruitment of additional blood supply to the tumor, increased vascular permeability, and so on.

The foregoing demonstrates that the distribution and evolution of tumor-associated vasculature influence TIFP distribution and evolution directly and vitally. Extending the single-tube model of Pozrikidis and Farrow [86], Pozrikidis [87] developed a network model that assumes the tumor vasculature is like a branching tree consisting of a cascade of straight bifurcating capillary segments. However, when this model is applied to the spherical symmetric case, it is incompatible with Baxter and Jain's model [80], which considered a greater number of factors. Additionally, the solution of Pozrikidis' model for TIFP may not possess the properties shown in Figs. 1 and 3. Baish and Jain [88] attributed the chaotic, poorly regulated growth of a tumor to "fractal" geometry. We described the chaotic growth of a tumor by comparing its growth to the growth patterns of normal cells and pointed out that "normal cells follow similar growth patterns, but tumor cells may not." Chaplain et al. [89] modeled the angiogenesis of a solid tumor. Dreher et al. [90] investigated tumor vascular permeability, accumulation and penetration of macromolecular drug carriers. Karshafian et al. [91] modeled transit time kinetics in ordered and disordered vascular trees using the simple rules of branching and fractal

geometry in two dimensions. Pindera et al. [92] simulated the angiogenesis using a convected element method. Since the angiogenesis of a tumor is time dependent, the TIFP should be related to the stages of tumor growth. However, no existing TIFP model considered time dependence. Both Pozrikidis and Karshafian et al. view the vasculature system as a treelike branching structure. Normal tissues have an ordered treelike branching pattern, but a tumor vascular network has a chaotic and random nature [87, 91].

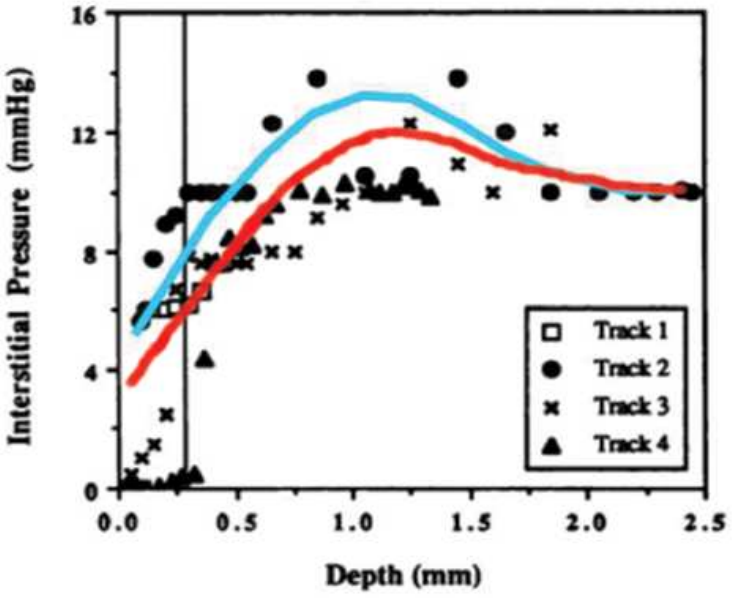

Fig.1.3 Experimental results of TIFP distribution in a s.c. tumor [81] (surface is 0)

Baxter and Jain's model [80] explains the spatial distribution of TIFP. Boucher et al. [81] measured the spatial distribution of TIFP and in some cases the results differ from their predictions. The experimental results for tissue isolated (t.i.) and subcutaneous (s.c.) tumors in Ref. 81 (See Figs. 3B and 6 for a mammary adenocarcinoma R3230AC in Ref. 81) were reported to indicate that the TIFP reached a maximum value at a depth of less than 1mm from the tumor surface, and then the IFP stayed steady and uniform in the central region of the tumor. The best fit through the data suggests otherwise, as shown in Fig. 1.3. Since Fig. 3B of Ref. 81 is typical, we introduce it here in Fig. 1.3. We draw the

best fit curve, which is shown in blue (upper curve) in Fig. 1.3, for the black dots since they are the most complete data in the entire experimental region. Similarly, we can draw the best fit curves for other data. Considering the clear nature of the graph, we do not depict them in Fig. 1.3. We also draw the best fit curve for all data in red (lower curve). TIFP in the central area is steady and uniform with a smaller value relative to the maximum at about 1mm below the surface of the tumor.

1.2 Problems

Though there are various models for tumor growth, tumor metastasis and tumor therapies, these models are mostly limited or isolated to one aspect. A model for tumor growth may not be applied to tumor therapy, and vice versa. A good model should not only be able to reflect the properties of tumor growth and development, but also be able to predict the response to various therapies and treatments. However, so far no model possesses these functions. The models for tumor growth are independent of the models for tumor therapies and/or tumor metastasis. The widely used model for radiation therapy is the LQ model, which is different from the models used for chemotherapy and unrelated to tumor growth. However, if we think about the process for tumor growth and treatment carefully, we should realize that there must be something to connect them to each other. Though varied therapies/treatments have different effects when applied to an entire system of an organism, cell responses to different therapies should share the same mechanism for an organism's growth.

In summary, many models can only quantitatively predict the growth process of a tumor. Also, no single model provides a clear answer for the production and death rates of tumor cells, which are closely connected to tumor growth. Correspondingly, the theoretical principles governing response to therapies are not completely established. Also, those

models were not (or could not be) connected to experimental results; they were not applied to or could not explain many experimental data. Many of them are not practical. Though the Gompertz model has greatly influenced the understanding of organisms and tumor growth, and despite many workers trying to connect their theoretical or experimental results with the Gompertz curve, this model has limitations, especially during the very early stage of growth, as we discussed above. West et al. showed that their model fits the growth process of many different species of organisms. Guiot et al. showed that this model also fits the growth process of many tumors. However, West's model also has its limitation. At first they idealized the entire organism as an identical cell system. Obviously, this is too inexact to describe multicellular organisms. Different tissues/organs have different kinds/types of cells. Malignant tumors are characterised by tumor cell heterogeneity [93, 94]. Also, in one single tumor there are many different regions that cannot be described by a simplified identical cell system. It is well established that tumor cells can be categorized as: a) viable oxygenated, b) viable hypoxic, or c) dying or necrotic, which stay in the tumor and form a necrotic region. These three types of cells have distinctly different growth rates. In addition, when a tumor metastasizes, West's model cannot be applied.

In tumor therapy, no existing theory for cell survival response can explain the experimental data consistently. The LQ model for radiation therapy does not fit many experimental survival curves [40, 42]. In fact, the LQ model is widely used and can be explained as the result of $dN/N = -(aD+b)dD$ (where N represents cell number, and a and b are two constants). The linear term αD (derived from b) is assumed to be the result of the single event killing, and the quadratic term βD^2 (derived from aD) is supposed to come from the double event killing [10]. Obviously, for a bio-system, it is not enough to only consider the terms of "killing." The LPL and LQL models improved the LQ model to some extent. However, they cannot be applied to some cases, especially for samples *in vivo*. Also, some assumptions made in the LPL model may not be satisfied. Still, the two-component LQ model fits some experimental data much better than other models, as αs and βs are not constrained. This causes the parameter to be redundant and one set of experimental data to correspond to more than one set of solutions (e. g. different αs, βs

and cell population fractions for the same survival curve of cell response). The theoretical model for chemotherapy is very limited. Many experimental data cannot be explained by any existing model.

TIFP is an early-response marker of the effectiveness of treatment and may have a promising application for monitoring cell response to the treatment. However, at present a noninvasive prognosticator of tumor response to treatment is not widely available. For the distribution of IFP in a solid tumor, the existing models do not reflect the actual properties and characteristics accurately. Also, no model has considered the time variation; tumors grow. Various stages may have different TIFP distribution. Steady state merely approximates TIFP distribution at a fixed stage (e.g. is a tumor mature and does it metastasize?).

1.3 The Idea of the Present Work

Tumors possess some of characteristics of an organism with specific properties in their growth processes. Various tumors and their specific growth processes make mapping the development of tumors rather complicated. The growth of a tumor mimics the growth of an organism and mathematical models have the potential to predict their curative and sub-curative response to therapies. Also, a good model should reflect the response of the system to treatment. Although no theory can uniformly explain tumor growth, tumor metastasis and the results of tumor therapies, we aim to provide the foundation for a more general equation for these situations. A general model, which possesses the virtues of West's model and can describe practical application, is the goal.

By introducing a production rate, which is defined as the average number of cells produced in a unit volume in unit time, and a death rate, which is defined as the number of cells that died in a unit volume in unit time, based on the mass balance equation, the net growth rate of an organism should be proportional to the difference between the

production rate and death rate. Combining this equation with the ubiquitous ¼ law in biological allometry, which is more general and fundamental, we derive a general equation for organism growth. We will show that it is the same as West's "universal law" for organism growth. We start by dividing an organism into many different small systems that have identical cells and then unite them by introducing similarity of growth. Normal cells grow harmoniously (even in different tissues), but tumor cells may not. For a tumor, there may be many different kinds of cells, with each set of identical cells having its own growth properties. When they can be unified by the rules of similarity of growth, we can express the total growth mass in a uniform equation. Otherwise, the growth process is chaotic. We have to arrive at the solutions separately and then add them together. Many previous mathematical models contained many parameters and factors and made their application complicated. It is true that many factors can influence the growth process of an organism and it is difficult to determine exactly how many of the parameters and which functions of each parameter contribute to growth. However, according to the idea of the present work, no matter how many parameters or ways a parameter may impact the growth of an organism, the consequence will be reflected by its production and death rates. It is the production and death rates that determine net growth and account for the metabolic process. All parameters such as nutrition supply, oxygen diffusion, and growth inhibition, as well as therapy/treatment, can be reflected by production and death rates. This may explain why the present model fits the experimental data very well when we apply it to radiation and chemotherapy.

For understanding the growth process and tumor metastasis, let us see a simple example. We assume that there is a container that does not have a rigid wall.

(1) Let us pour some identical beans into this container. We assume that m_c is the mass of a single bean. The number density C (the number of beans per unit volume) in this system is always a constant. No matter what method is used, the mass change can be expressed by the equation:

$$\frac{dm}{dt} = \frac{d(CVm_c)}{dt} = -m_c C \oiint \vec{u} \cdot d\vec{A}$$

(2) Now each bean in the container proliferates from 1 to 2, 2 to 4, etc. (like a bio-process). As some new beans are reproduced, some old ones die (metabolism). The production and death rates in a unit volume and unit time are supposed to be $\bar{S}$ and E (average number of cells produced and died per unit volume and unit time). The total number of beans in this system is proportional to the total volume of the beans. The rate of increase in net mass is proportional to the difference between the production and death rates, as well as the total volume. It is expressed as $Vm_c(\bar{S}-E)$, where E is a constant but $\bar{S}$ is not. It is an average measurement. We gave detailed expression and process for determining it (as well as E) in section 2. Now the equation is modified as:

$$\frac{dm}{dt}=\frac{d(CVm_c)}{dt}=-Cm_c\oiint\vec{u}\cdot d\vec{A}+Vm_c(\bar{S}-E)=-Cm_c\oiint\vec{u}\cdot d\vec{A}+\frac{m}{C}(\bar{S}-E)$$

(3) If there is no flux term of beans, the above equation is reduced to

$$\frac{dm}{dt}=\frac{m}{C}(\bar{S}-E).$$

(4) Now suppose that there are many different kinds of beans in different compartments (like different cells in different tissues). Though they follow their own growth law, they grow harmoniously. Different beans are relatively restrained in their separate locations. Each set of beans can be expressed as:

$$\frac{dm_k}{dt}=\frac{m_k}{C_k}(\bar{S}_k-K_k)$$

(5) This ideal can be used to deal with the growth of normal cells and tumor cells.

Cell response to therapies is a way to check the model for organism growth. In fact, when dose or dose rate is zero, a model for cell response to therapy should be compatible with the natural growth or death process before treatment is applied, as this model does. However, the LQ and LPL models do not possess this feature. Tumors are specific organisms. As a matter of fact, response to therapies, effect of treatment and prognosis are related to the process of tumor cell growth, as well as tumor metastasis. They can be derived from the governing equation for organism growth. Surgery decreases the mass immediately. Radiation and conventional chemotherapy cause an additional death rate,

whereas antiangiogenic therapy decreases the production rate by prohibiting the growth of tumor vessels that deliver nutrition and oxygen.

Determining a way to model or explain the survival response to radiation and chemotherapy is an important goal and achieving it may lead to a better understanding of effective treatment methods. In this work, starting from a mass balance equation and attributing an additional death rate to therapy, we derive a general equation for response to treatment, which in turn connects the response with a growth process and may be applied to radiation and chemotherapy equally.

When we do curve fitting for cell response to radiation based on the model we present, we find that there are always some (10% flexible) "resistant" cells under both well-oxygenated and hypoxic conditions. If this is indeed the case, then these "resistant" cells should exist and respond differently to chemotherapy, though they may not be more resistant to some agents (e.g. response of EMT6 cells to Mitomycin-C is more resistant under aerated conditions than hypoxic [10]). It is known that there are some "resistant" cells in case of radiotherapy and chemotherapy. Cancer stem cells are hypothesized to be more resistant to radiation than other cancer cells [55, 56]. They are also a chemotherapy-resistant population [68, 69]. Is it perhaps possible that there is a small fraction of stem cells in normal cells as well as cancer stem cells in cancer cells? No matter what the case may be, we cannot ignore the fact that some resistant cells exist.

We also noted that some experimental data for survival response in both radiation and chemotherapy [54, 61] do not fit any existing models. In fact, the LQ equation is an approximate result of the present model under special conditions. When we apply the complete equation to deal with these experimental data, it fits the survival curves well.

Chapter 2. Previous Models and Theories

To chart the growth of an avascular tumor, many mathematical models have been developed based on the diffusion-reaction equation. A typical model is expressed as [16, 17]:

$$\frac{\partial n}{\partial t} + \nabla \cdot (vn) = [k_m(c) - k_d(c)]n \tag{2.1}$$

$$\nabla \cdot v = k_m(c) n V_L - k_d(c) n (V_L - V_D) \tag{2.2}$$

$$\frac{\partial c}{\partial t} + \nabla \cdot (D \nabla c) - [\beta k_m(c) + \gamma(c)]n \tag{2.3}$$

where n, v and c are three unknowns that represent the number of living cells, local growth velocity and nutrient concentration respectively. Here k_m and k_d are the mitosis and death ratios. V_L and V_D represent the living and dead cell volume, and γ and β are the nutrient consumption rates of a cell in interphase and in mitosis, respectively. Also,

$k_m(c) = \frac{A c^{m_1}}{c_c^{m_1} + c^{m_1}}$, $k_d(c) = B(1 - \frac{\sigma c^{m_2}}{c_d^{m_2} + c^{m_2}})$, where c_c and c_d represent the critical concentrations for cell proliferation and cell survival, respectively. $A=k_m(\infty)>0$, $B=k_d(0)>0$ and $k_d(\infty)=B(1-\sigma)$, where $0 \le \sigma \le 1$.

So far, no single diffusion-reaction model is accepted as a general model for an organism's growth since diffusion-reaction models can only qualitatively fit the experimental data. Though many parameters have been considered the aforementioned model, it still may not describe the growth process exactly. We may ask how many parameters should be considered and what the exact pattern for each specific parameter should be. As we mentioned in the introduction, there might be many parameters that influence the growth process. However, no matter how many parameters determine the

growth of an organism, they embody the production and death rates, which reflect metabolism.

Ever since Laird [4] first applied Gompertz's function to fit the growth of tumors in 1964, theoretical and experimental studies have allowed for the application of the Gompertzian function to tumor growth [31, 95, 96]. In fact, the Gompertzian function for tumor growth stems from the Gompertz differential equation:

$$\frac{dm(t)}{dt} = -\chi m(t) \ln\left[\frac{m(t)}{M}\right] \tag{2.4}$$

where M represents the maximum mass that can be reached with the available nutrients and is expressed as $M = \lim_{t\to\infty} m(t)$, and χ a positive constant related to the proliferative ability of the cells. We relate the size of the tumor to the mass $m(t)$. The solution of this equation is

$$m(t) = M \exp[\ln(m_0 / M)\exp(-\chi t)] \tag{2.4′}$$

where m_0=$m(0)$. The problem is that the growth rate in the very early stage may deviate from this function. Wheldon [8] proposed a critical size for applying Gompertz's function. Mathematically, equation (2.4) is the limiting case of the "generalized logistic" differential equation:

$$\frac{dm(t)}{dt} = \chi \upsilon m(t)\left[1 - \left(\frac{m(t)}{M}\right)^{1/\upsilon}\right] \tag{2.5}$$

Here υ is a positive number. When υ is large or $\upsilon\to\infty$, eq. (2.5) becomes eq. (2.4). The models that originate from eq. (2.5) are called "generalized logistic" models [95].

Starting from the conservation of total energy for maintaining and creating tissue, West et al. [33] presented a general model to describe organism growth (mass-time relation) by combining energy conservation with Kleiber's law [32], which reads [33]

$$\frac{dm}{dt} = am^{3/4}\left[1-\left(\frac{m}{M}\right)^{1/4}\right] \tag{2.6}$$

The solution is [33]

$$1-\left(\frac{m}{M}\right)^{1/4} = \left[1-\left(\frac{m_0}{M}\right)^{1/4}\right]\exp\left(-\frac{at}{4M^{1/4}}\right) \tag{2.7}$$

where m_0 is the initial mass, M is the asymptotic mass that corresponds to the maximum size, and a is a parameter that is related to the growth characteristics of the organism or tumor [33, 34]. When $m = (3/4)^4M \approx M/3$, $\mathrm{d}^2m/\mathrm{d}t^2=0$, the growth rate is maximal. West et al.'s model is based on a more fundamental biological law and shows that there is a "universal law" for ontogenetic development. The maximum growth rates for "generalized logistic" curve, Gompertz's curve and West's model happen at $(256/625)M \approx 0.41M$, $(1/e) \approx 0.37M$ and $(81/256) \approx 0.32M$, respectively. The larger the mass, the less the difference amongst these models. Though the "generalized logistic" growth rate can be raised by increasing the value of υ, the limitation with the Gompertz's curve is when $\upsilon \to \infty$. We compare the growth rates of Gompertzian model and West et al.'s model in table 2.1.

Table 2.1 Growth rates of Gompertzian model and West et al.'s model

$m(t)/M$		1/100	1/32	1/16	1/8	1/4	1/3	1/2	3/5	4/5	0.9	1
Growth rate	Gompertz	0.046	0.108	0.173	0.260	0.347	0.366	0.347	0.306	0.179	0.095	0
$\mathrm{d}m/\mathrm{d}t(\chi M)$	West	0.086	0.172	0.250	0.341	0.414	0.421	0.378	0.327	0.184	0.096	0

From table 2.1, we see that the growth rate of Gompertz's model from $M/16$ to $M/4$ fit that of West's model from $M/32$ to $M/8$ quite closely. This means that these two models can fit well in a certain time period by choosing some specific parameters m_0, M and χ. Fig. 2.1 shows that Gompertz's model and West's model can fit very well after $m(t)>M/3$ when we choose a specific m_0. If we want to fit the curve in the early growth stage, we can choose a very small m_0 for both models and adjust the value of χ. However, the

research results of Steel [7] and Wheldon [8] implied that the Gompertz equation might not be good to model the growth of small tumors or organisms.

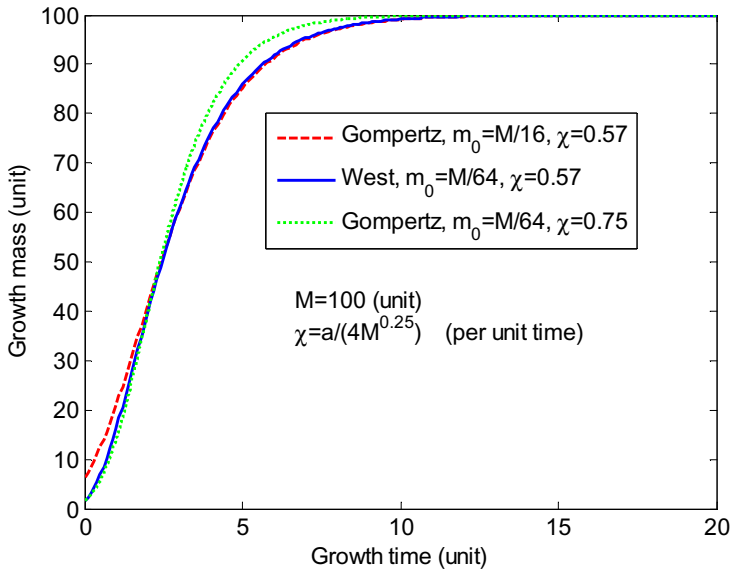

Fig. 2.1 Tumor growth curves for Gompertz and West models

Based on the mass balance equation, we derive a general equation for organism growth (including tumor growth), and show that it is the same as West et al.'s. In this model, we will see that $a=\beta^{\circ}M^{1/4}=4\chi M^{1/4}$, where β° is a constant that controls the harmonious growth of an organism. Compared to Gompertzian and "generalized logistic" models, West et al.'s model as wells as the model we will present, show that the constant $\upsilon=4$ and the product factor is $m^{3/4}(t)$.

As mentioned in chapter 1, for cell response to radiation, the widely used LQ model is expressed as [10, 40-42]:

$$SF = \exp[-(\alpha D + \beta D^2)] \tag{2.8}$$

The α and β reflect cell killing mechanism. The α/β ratio represents the dose at which the linear and quadratic components of the LQ model contribute equally to cell killing [42].

There are also some other models for cell response to radiation. The single-hit, multitarget (SHMT) model is expressed as [50]:

$$SF = 1 - (1 - e^{-D/D_0})^n] \tag{2.9}$$

where n is the number of targets in each cell and D_0 the dose for an average of one hit per target. The RMR (repair-misrepair) two-parameter and RMR three-parameter models are expressed respectively as [50]:

$$SF = e^{-\delta D}\left(1 + \frac{\delta D}{\varepsilon}\right)^{\varepsilon} \tag{2.10}$$

$$SF = e^{-\delta D}\left(1 + \frac{\delta TD}{\varepsilon}\right)^{\varepsilon\phi} \tag{2.11}$$

where $T = 1 - e^{-\lambda t}$, λ is the linear self-repair coefficient, $\varepsilon=\lambda/\kappa$ is repair ratio, κ the coefficient for cooperative repair, ϕ is the probability that self-repair are all perfect. Since the LQ model does not fit many survival curves well, it has been modified to other forms. The two-population LQ model is described as [50]

$$SF = fe^{-\alpha_s D - \beta_s D^2} + (1 - f)e^{-\alpha_r D - \beta_r D^2} \tag{2.12}$$

where f and 1-f represent the fractions of sensitive and resistant cells respectively. The subscript "s" and "r" are used to identify the parameters for sensitive and resistant cells. Skarsgard et al. [50] compared the SHMT, RMR two-parameter, RMR three-parameter, LQ and two-population LQ models by applying them to fit the survival curves of asynchronous V79 cells. They found that the two-population LQ model fits best. Next is the RMR three-parameter model, and then the LQ model. The RMR two-parameter model is the worst fit. However, the two-population LQ model may cause parameters to become redundant since the αs and βs are not constrained.

In order to fit the survival curves better, Astrahan [40] modified the LQ model and presented it as the LQ-L model empirically. In this model, the author introduced a dose D_T and used a segment function to describe the surviving fraction under radiation:

$$SF = \begin{cases} e^{-\alpha D - \beta D^2} & for \quad D < D_T \\ e^{-\alpha D_T - \beta D_T{}^2 - \gamma (D - D_T)} & for \quad D > D_T \end{cases} \tag{2.13}$$

When dose is smaller than D_T, the survival response follows the LQ model. When dose is greater than D_T, the logarithm of the surviving fraction versus the dose (ln*SF*—*D*) has a linear relation. D_T is defined as the dose at the tangent point of the LQ curve and the linear ln*SF*—*D* line. However, this model does not fit some cases, which will be shown later.

Curtis [45] presented an LPL (lethal and potential lethal) model that is based on five major assumptions. Mathematically, it is described as follows:

1) During the irradiation:

$$\frac{dn_{PL}(t)}{dt} = \eta_{PL}\dot{D} - \varepsilon_{PL} n_{PL}(t) - \varepsilon_{2PL} n_{PL}{}^2(t) \tag{2.14}$$

$$\frac{dn_L(t)}{dt} = \eta_L \dot{D} + \varepsilon_{2PL} n_{PL}{}^2(t) \tag{2.15}$$

where n_{PL} and n_L represent the mean numbers of potentially lethal and lethal lesions, respectively, during the irradiation period, ε_{PL} and ε_{2PL} are the rates per unit time of correct repair and binary misrepair, respectively, for the potentially lethal lesions. The η_L and η_{PL} are the rates per unit absorbed dose for production of the lethal and potentially lethal lesions, respectively. The initial conditions are $n_{PL}(0)=n_L(0)=0$ since no lesions are assumed to be present at the start of the irradiation. The solutions are:

$$n_{PL}(t) = \frac{2\eta_{PL}\dot{D}(1 - e^{-\varepsilon_0 t})}{\varepsilon_0 + \varepsilon_{PL} + (\varepsilon_0 - \varepsilon_{PL})e^{-\varepsilon_0 t}} \tag{2.16}$$

$$n_L(t) = \eta_L D + \varepsilon \ln\left[\frac{2\varepsilon_0}{\varepsilon_0 + \varepsilon_{PL} + (\varepsilon_0 - \varepsilon_{PL})e^{-\varepsilon_0 t}}\right] + \frac{(\varepsilon_0 - \varepsilon_{PL})^2 t}{4\varepsilon_{2PL}} - n_{PL}(t) \tag{2.17}$$

where $\varepsilon_0 = (\varepsilon_{PL}{}^2 + 4\varepsilon_{2PL}\eta_{PL}\dot{D})^{1/2}$, and $\varepsilon = \varepsilon_{PL}/\varepsilon_{2PL}$.

2) After the irradiation:

Assuming that the irradiation stops at time T, then

$$\frac{dn_{PL}(t)}{dt} = -\varepsilon_{PL} n_{PL}(t) - \varepsilon_{2PL} {n_{PL}}^2(t) \tag{2.18}$$

$$\frac{dn_L(t)}{dt} = \varepsilon_{2PL} {n_{PL}}^2(t) \tag{2.19}$$

Now the initial conditions for eqs. (2.18) and (2.19) are $N_{PL}=n_{PL}(T)$ in eq. (2.16) and $N_L=n_L(T)$ in eq. (2.17). Similarly, we can solve these two eqs. and get the formulae for n_{PL} and n_L after irradiation:

$$n_{PL}(t) = \frac{N_{PL} e^{-\varepsilon_{PL} t_r}}{1 + N_{PL}/\varepsilon(1 - e^{-\varepsilon_{PL} t_r})} \tag{2.20}$$

$$n_L(t) = N_L + N_{PL}(1 + \frac{N_{PL}}{\varepsilon}) \frac{1 - e^{-\varepsilon_{PL} t_r}}{1 + N_{PL}/\varepsilon(1 - e^{-\varepsilon_{PL} t_r})} - \varepsilon \ln[1 + N_{PL}/\varepsilon(1 - e^{-\varepsilon_{PL} t_r})] \tag{2.21}$$

where t_r is the time available for repair after the end of the exposure. So the total mean number of lethal lesions per cell is

$$n_{tot}(T + t_r) = n_L(T + t_r) + n_{PL}(T + t_r) \tag{2.22}$$

Using the Poissonian assumption for the distribution of lethal lesions per cell, we write the survival as the probability that a cell has no lethal lesion:

$$SF = e^{-n_{tot}(T+t_r)} = e^{-n_L(T+t_r) - n_{PL}(T+t_r)} = e^{-N_{tot}} [1 + N_{PL}/\varepsilon(1 - e^{-\varepsilon_{PL} t_r})]^{\varepsilon} \quad (N_{tot}=N_L+N_{PL}) \tag{2.23}$$

This model has three characteristics: 1) There is an initial nonzero slope. 2) There is a region of the survival curve at low dose that can be approximated by a linear-quadratic function in the absorbed dose. In other words, the LQ model is approximately satisfied. 3) At high doses, the slope of the survival curve approaches a constant, which is a measure of the total number of initial biological lesions created by the radiation and corresponding survival response [45]. However, the first characteristic may not be satisfied in many survival curves. The other two characteristics can be included in the LQ-L model. The

typical results of the LPL model are shown in Fig. 2.2. This model gives the linear survival response under low dose rate condition and the LQ survival response under high dose rate condition.

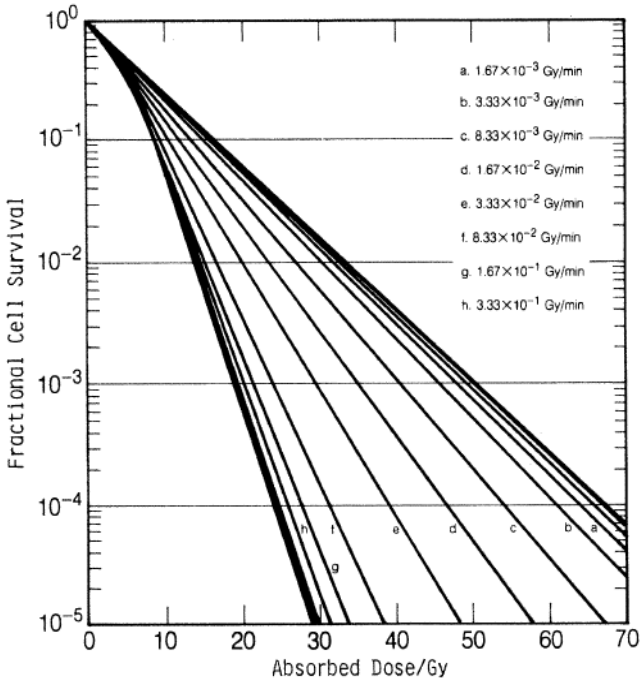

Fig. 2.2. A family of survival curves as given from the LPL model [45]

After considering the mechanistic formulation of Astrahan's LQ-L model and the method of the LPL model, Guerrero and Carlone presented their LQL model. Similar to the LPL model, the basic equations of the LQL model are described as:

$$\frac{dL(t)}{dt} = 2pR(t) - \mu L(t) - p\varepsilon_{LQ}R(t)L(t) \tag{2.24}$$

$$\frac{dL_f(t)}{dt} = \alpha R(t) + p\varepsilon_{LQ}R(t)L(t) \tag{2.25}$$

where $L(t)$ represents repairable lesions, $L_f(t)$ fatal or irreparable lesions, $R(t)$ the dose rate, p the yield of lesions per unit dose, ε_{LQ} the probability of an existing lesion forming

a new lesion, μ the repair rate, and α the usual LQ parameter. This model combines the virtues of the LQ-L and LPL models theoretically. However, none of these models can completely fit or explain some of the radiation survival curves, as we will later show.

Though many chemotherapeutic agents have been developed and corresponding survival responses have been tested, the mechanism used in chemo's killing is not clear and theoretical models are limited. The survival curves are various for diverse chemotherapeutic agents. Responses of Chinese hamster and HeLa cells to doxorubicin can be fitted approximately with the exponential model, which is expressed as [66]:

$$SF = e^{-kt_{\exp}c_e} \tag{2.26}$$

where SF is survival relative to controls, k is a parameter that depends on the cell line, $t_{\exp}$ is exposure time, and c_e is extracellular drug concentration.

Empirically, survival curves for chemotherapy can be well fitted with the Hill equation, which is expressed as [66]:

$$SF = \frac{1}{1 + A \cdot D^n} \tag{2.27}$$

D represents the cellular damage, which is a function of drug concentration and exposure time. A and n are constants. Many different formulae are given by modifying the function D with various contents.

For the distribution of TIFP, the typical model was presented by Baxter and Jain [80]. They introduced a spherical model and used Starling's law to estimate fluid leaking from blood vessels and Darcy's law to estimate flow through a porous medium. Mathematically, it is expressed as:

$$-K\nabla^2 p_i = \phi_V(r) - \phi_L(r) \tag{2.28}$$

where K is the hydraulic conductivity of the interstitium, p_i represents the interstitial pressure, r is the radial position, $\phi_V(r)$ is the fluid source term and $\phi_L(r)$ is the lymphatic

drainage term. The source term can be described by Starling's law and the drainage term is assumed to be proportional to the pressure difference between the interstitium and the lymphatics. Mathematically, they are expressed as:

$$\phi_V(r) = \frac{L_p S}{V}[p_V - p_i - \sigma_T(\pi_V - \pi_i)] \qquad \text{for } r \geq r_n \qquad (2.29)$$

$$\phi_L(r) = \frac{L_{pL} S_L}{V}(p_i - p_L) \qquad \text{for } r \geq r_n \qquad (2.30)$$

$$\phi_V(r) = \phi_L(r) = 0 \qquad \text{for } r < r_n \qquad (2.31)$$

where S/V is the surface area per unit volume for transport in the tumor, L_p and L_{pL} are the hydraulic conductivities of the microvascular wall and the lymphatic wall, p_v is the vascular pressure, p_L is the hydrostatic pressure of the lymphatics, σ_T is the average osmotic reflection coefficient for plasma proteins, and π_v and π_i are osmotic pressures of the plasma and the interstitial fluid, respectively.

The boundary conditions are: 1) $\nabla p_i\big|_{r=0} = 0$; 2) $p_i\big|_{r=R} = p_\infty$ for an isolated tumor, or $-K_T \frac{dp_i}{dr}\Big|_{r=R^-} = -K_N \frac{dp_i}{dr}\Big|_{r=R^+}$ and $p_i\big|_{r=R^-} = p_i\big|_{r=R^+}$ for an embedded tumor. K_T and K_N are the hydraulic conductivities of the tumor and normal tissue, respectively.

Chapter 3. A general model for solid tumor growth and response to therapies

3.1 The Present Model (Our Model)

We assume that all cells in a specific organ/tissue are identical and treat them as a system. We use the subscript k to identify the system. In this small system, cells have a constant number density C_k and the mass of a cell is m_{ck}. When they grow, the number density does not change or changes little. This causes both the volume and mass to increase. Organism growth is the process of biological metabolism in terms of cell division. Some fluids such as blood and interstitial fluid may flow in and out in a balanced way, maintaining the metabolism by supplying nutrients and draining waste. Suppose at time t, the volume of this system is V_k, the number of cells that died in a unit volume in unit time is E_k, and the average number of cells produced in a unit volume in unit time is $\overline{S}_k$. The mass is $m_k=V_kC_km_{ck}$. In the natural growth process, cells in a specific tissue/organ are relatively steady. They do not flow from one tissue to another. Therefore, the cell flux is zero. The only exchange with the outside is when nutrition is supplied or when wastes are drained, maintaining the metabolism. This process embodies the production and death rates of cells, which determines the growth of the system. Since the cell flux is zero, the growth rate of this system can be written as:

$$\frac{dm_k}{dt} = m_{ck}V_k(\overline{S}_k - E_k) \tag{3.1.1}$$

In fact, eq. (3.1.1) is a mass balance equation. The system's net growth rate is proportional to the difference between the production and death rate. This way, it is easier to control or influence the growth of the system by changing a term or both the production and death rate. We will see the advantage in doing so later in application to tumor therapies.

In a tumor, normal cells and tumor cells (which are usually pleomorphic) may coexist. Human solid tumors often possess heterogeneity of both neoplastic and normal cells. A tumor can also be divided into different systems since it may be composed of various tumor cells [93, 94], each made of identical cells. Similarly, we can use eq. (3.1.1) to describe the growth of each small system in a tumor before metastasis since there is no tumor cell flux during this growth stage. For an identical system, we can use the number of cells (which is the most common method), mass, or volume to express its growth. Once we know the percentage of specific cells in a tumor at a certain time, we can estimate the amount of those cells later on.

Tumor blood vessels are larger, longer and denser than normal microvessels [72]. They are abnormal and leaky. On one hand, this results in elevated tumor interstitial fluid pressure; on the other hand, this may be a source of nutrition for tumor growth (which is angiogenesis dependent) that is reflected by the production and death rates. Eq. (3.1.1) can be applied before metastasis occurs. However, according to the activity of cells, a tumor may be divided into three regions: a necrotic core where most tumor cells are dead, a quiescent cell region where most cells are non-proliferating, and a well-vascularized region where tumor cells are active [72]. Tumor cells have different growth environments and nutrition supplies in different regions. Consequently, parameters such as $\overline{S}_k$, E_k are not the same. Some environments may even cause additional cell death rate. In the quiescent cell region, $\overline{S} \approx E$ (the production and death rates are almost balanced). In the necrotic core, it is probable that $\overline{S} < E$ (cells are dying or dead). In the well-vascularized region, $\overline{S} > E$ (where tumor cells contribute the most towards tumor growth), which means we should concentrate on them. Nevertheless, in tumor therapy, the quiescent cells cannot be ignored since quiescent cells may be radioresistant and become active again under certain conditions.

Now, let us determine the death rate E_k and production rate $\overline{S}_k$. For convenience, we ignore the subscript *k* from now on unless it is needed for identification. We adopt West's viewpoint: "the cell death rate is proportional to the number of cells present" [33]. In a specific system, the average lifetime of every single cell is fixed, and so is the number of cells in a unit volume *C*. Thus, it is reasonable to assume that the death rate *E* of cells in a

unit volume in unit time is a constant in this case. The most important matter is to determine the production rate $\bar{S}$. Most biological phenomena scale as a quarter power of the mass [32, 33, 97-102]. Though this is an empirical law that is similar to but more general than Kleiber's law, it is ubiquitous in biological allometry. Based on the ¼ power law, some empirical equations fit the ontogenetic growth trajectories for organisms better than any biological model [33, 103-106]. West et al. indicated that "rates of cellular metabolism and heartbeat [scale] as $M^{-1/4}$ and whole-organism metabolism rate as $M^{3/4}$." [97] Considering the general ¼ power law in biological allometry, the production **rate** of cells during metabolic processes should be the reciprocal of the ¼ power of the mass, namely,

$$\bar{S} \propto 1/m^{1/4} \quad \text{or} \quad \bar{S} = \Gamma m^{-1/4}, \tag{3.1.2}$$

where Γ is a proportionality factor. Also, considering the condition that $m=M$ at $dm/dt=0$, we have $\Gamma = EM^{1/4}$. Thus,

$$\bar{S} = E\left(\frac{M}{m}\right)^{1/4} \tag{3.1.3}$$

where M is the maximum mass reached asymptotically among species within a system [33], which corresponds to the mass when $dm/dt=0$. The production rate is much greater than the death rate at an early growth stage. It slows down gradually while the mass increases. When the mass reaches the asymptotic mass, the production rate equals the death rate. Substituting equation (3.1.3) into equation (3.1.1) results in

$$\frac{dm}{dt} = \frac{E}{C} m\left[\left(\frac{M}{m}\right)^{1/4} - 1\right] \tag{3.1.4}$$

Next we will show that equation (3.1.4) is exactly the same as West's equation [33]. West et al. consider a whole organism as a system composed of identical cells. In this case, the present model (ours) can be applied. Assume the initial, or birth, mass is m_0. Then the solution of equation (3.1.4) is,

$$1-\left(\frac{m}{M}\right)^{1/4}=\left[1-\left(\frac{m_0}{M}\right)^{1/4}\right]\exp\left(-\frac{Et}{4C}\right)=\left[1-\left(\frac{m_0}{M}\right)^{1/4}\right]\exp\left(-\frac{\Gamma t}{4CM^{1/4}}\right) \tag{3.1.5}$$

For a tumor, m_0 and M are the initial and final masses respectively [34]. In reference [33], West et al. discussed the death rate of cells and discovered that death rate in the entire system is $aM^{-1/4}N_c$, where N_c is the total cell number. It should be equal to EV in the present model. In this case, $EV = aM^{-1/4}N_c$. Since $C=N_c/V$,

$$\frac{E}{C}=aM^{-1/4} \quad \text{and} \quad \frac{\Gamma}{C}=a \tag{3.1.6}$$

Thus, equation (3.1.4) is the same as equation (2.6). Correspondingly, equation (3.1.5) is the same as equation (2.7). From the discussion above, we see that there is a direct method to derive the universal law for organism growth based on the mass balance equation. For a specific system, the number density of cells, the mass of a cell, as well as the average production and death rates are all fixed in the absence of therapy. When the environment is fixed, the growth law of the cell system is also fixed.

West et al. view all cells in an organism as the same. However, as we have remarked above, cells of one tissue are different from those of another. Therefore, the number density, the production and death rate, and the mass may all be different. Each specific tissue has its own asymptotic maximum and initial mass. Generally, for tissue k, we can write the governing equation for growth as:

$$\frac{dm_k}{dt}=\frac{E_k}{C_k}M_k^{1/4}m_k^{3/4}\left[1-\left(\frac{m_k}{M_k}\right)^{1/4}\right] \tag{3.1.7}$$

Then, the growth equation for the entire organism may be expressed as:

$$\frac{dm_t}{dt}=\frac{d}{dt}\left(\sum_{k=1}^{N}m_k\right)=\sum_{k=1}^{N}\frac{E_k}{C_k}M_k^{1/4}m_k^{3/4}\left[1-\left(\frac{m_k}{M_k}\right)^{1/4}\right] \tag{3.1.8}$$

Here, N is the amount of different types of tissue in a given organism. Let us assume that

all types of tissue grow harmoniously, and that there is a standardized mass $m^{\circ}(t)$. The relationship between it and the mass of each tissue is $m_k(t) = w_k m^{\circ}(t)$. Thus, $M_k = w_k M^{\circ}$ and $m_t = m^{\circ}(t)\sum_{k=1}^{N} w_k$, which can lead to $M_t = M^{\circ}\sum_{k=1}^{N} w_k$. We call this the similarities of growth. Here w_k is the proportionality coefficient of growth of tissue k and M° is the asymptotic mass of $m^{\circ}(t)$. Since the death rate of cells is proportional to the number of cells, cells in a tissue with a higher number density also have a higher death rate. In each specific tissue, the number density C_k is fixed. It is reasonable to suppose that $E_k/C_k=\beta^{\circ}$. Different tissues share the same β°. For a specific organism, β° of its various tissues should remain constant; otherwise, the entire system could not grow harmoniously or isotropically. Based on these two assumptions, we have:

$$\frac{dm_t}{dt} = \beta^{\circ}(M^{\circ})^{1/4}(m^{\circ})^{3/4}\left[1-\left(\frac{m^{\circ}}{M^{\circ}}\right)^{1/4}\right]\sum_{k=1}^{N} w_k = \beta^{\circ} M_t^{1/4} m_t^{3/4}\left[1-\left(\frac{m_t}{M_t}\right)^{1/4}\right] \qquad (3.1.9)$$

By comparing eq. (2.6) with eq. (3.1.4), β° can be determined by the relation $\beta^{\circ}= E/C =aM^{-1/4}$. The value of β° reflects the relative death rate. For the entire organism to follow the growth law, it is necessary for different tissues to share a similarity in growth. M°, m° and β° should be the parameters of the original cells, which are often stem cells, of an organism. According to the explanation of West et al. [33], the asymptotic maximum mass M of an organism is constant at extreme nutrition condition. However, the asymptotic maximum mass of each tissue might be affected by the nutrition supply. This makes the growth of an entire organism complicated.

Based on the rules for similarity of growth and eq. (3.1.5), it is easy to prove that the fractions of different cells in a system are invariable if assorted cells have the same $\beta^{\circ}=E/C$ and their asymptotic masses share the same fractions ($M_k=x_kM$). For instance, if a system is composed of two kinds of cells with fractions $x_1=9x_2$, then $M_1=9M_2$ and $a_1\approx 1.732a_2$ (since $\beta^{\circ}_1=\beta^{\circ}_2$).

Nutrition supply might be spatially dependent. Tumor cells proliferate and grow actively when they are close to a source of nutrition (including oxygen). Thomlinson and Gray recognized that the necrotic center enlarges when a tumor cord grows larger so that the thickness of the sheath of viable tumor cells remains essentially constant [9, 10]. In fact, the asymptotic mass is nutrition dependent. We can take it as a function of nutrition. Cells that are close to a nutrition source have plenty of nourishment. Correspondingly, they have a larger asymptotic mass M and growth parameter a than cells that are farther away. Based on eq. (3.1.7), it is easy to conclude that they grow faster. Even so, it does not mean that these cells will crowd around the nutrition source and be scattered if they are away from the source. In fact, all cells still have the same size and density (Here is the case for one type of cell system). They distribute evenly and, following eq. (3.1.9), grow harmoniously. This is a very important point. It makes a system have a constant (or relatively steady) density and death rate, whereas the production rate, and correspondingly the net growth rate, change spatially based on the distribution of nutrition. This is the real meaning of harmonious growth. In fact, eq. (3.1.9) is an average effect. According to the rules for similarity of growth, if the nutrition supply is spatially dependent, the proportionality coefficient w will also be spatially dependent. The sum of w_k ($\sum w_k$) becomes an integral ($\int dw$). The total asymptotic mass is $M_t=M\,°\int dw$ and total instant mass is $m_t=m°_t\int dw$. If we know the distribution function of w, we can find the integral. The M_t and m_t still follow eq. (3.1.9). Similarly, for multicellular population systems, $M_t=M\,°\Sigma\int dw_j$ and $m_t=m°_t\,\Sigma\int dw_j$. If these cells follow the rules for similarity of growth, eq. (3.1.9) is satisfied. Things might become complicated if identical cells are separated by other cells spatially (e.g. tumor metastasis). They may grow at different times and growth rates.

3.2 Application of Present Model to Tumor Growth and Metastasis

The theory that tumors originate from tumor stem cells is gaining acceptance [107-110]. This, in turn, implies that tumor growth is an ontogenetic process in an independent system. Tumor growth is also the process of cell proliferation, which is embodied in cell production and death. Therefore, tumor growth also follows the "universal" law for organism growth [34]. Multicellular organisms are composed of various organs/tissues. Consuming nutrients and excreting waste are necessary in order to maintain a regular metabolism. They are included in the production and death rates. West's model applies to organism growth in an unrestricted dietary condition, which makes the asymptotic mass M maximum [33, 34]. Any lack of nutrition causes the asymptotic mass to decrease. Correspondingly, the production rate $\overline{S}$ decreases. Once the asymptotic mass becomes smaller than the present mass $m(t)$, the production rate becomes smaller than the death rate ($\overline{S} < E$); then the growth rate is less than zero ($dm/dt<0$).

3.2.1 Primary Tumor Growth

In the case of a primary tumor, no tumor cell flows or diffuses into it from the outside. Also, no tumor cells flow out before metastasis. Therefore, eq. (3.1.7) can be applied. If we let $E_k / C_k = \beta_k^{\circ}$, the equation can be rewritten as:

$$\frac{dm_k}{dt} = \beta_k^{\circ} m_k \left[\left(\frac{M_k}{m_k} \right)^{1/4} - 1 \right] \tag{3.2.1}$$

In a tumor mass, there may be both normal and tumor cells. For normal cells, no matter how many different types there are, they all have the same β° and follow equation (3.1.9). We use subscripts "N" and "T" to identify the normal cells and tumor cells respectively. Assume there are G kinds of tumor cells. They all follow eq. (3.1.7) and/or (3.1.8), but may or may not follow equation (3.1.9). Therefore, the total mass of the entire tumor m_t is: $m_t = m_N + m_T = m_N + \sum_{j=1}^{G} m_j$. Here, we only discuss two special cases:

(1) All normal and tumor cells of the tumor follow the rules for similarities of growth. Therefore, tumor growth follows equation (3.1.9) and can be expressed as:

$$\frac{dm_t}{dt} = \beta^\circ m_t \left[\left(\frac{M_t}{m_t} \right)^{1/4} - 1 \right] \tag{3.2.2}$$

where $\beta^\circ = \frac{\overline{E}}{\overline{C}} = \frac{E_N + E_T}{C_N + C_T}$. This may be the case for benign tumor or hyperplasia. The entire system still grows harmoniously and is under control. The solution for the equation above is:

$$1 - \left(\frac{m_t}{M_t} \right)^{1/4} = \left[1 - \left(\frac{m_{0t}}{M_t} \right)^{1/4} \right] \exp\left(-\frac{\beta^\circ t}{4} \right) \tag{3.2.3}$$

(2) All tumor cells obey the rules for similarities of growth, but $\beta_T{}^\circ$ is different from $\beta_N{}^\circ$.

$$\frac{dm_T}{dt} = \beta_T{}^\circ m_T \left[\left(\frac{M_T}{m_T} \right)^{1/4} - 1 \right] \tag{3.2.4}$$

The solution for tumor cells is:

$$1 - \left(\frac{m_T}{M_T} \right)^{1/4} = \left[1 - \left(\frac{m_{T0}}{M_T} \right)^{1/4} \right] \exp\left(-\frac{\beta_T{}^\circ t}{4} \right) \tag{3.2.5}$$

We ignore the mass of normal cells in the tumor and use equation (3.2.5) to approximate the growth of the entire tumor when tumor cells dominate tumor growth ($m_T >> m_N$). $m_{0T} \approx m_{0t}$, $M_T \approx M_t$. Most tumors probably belong to this case. We may use equation (3.2.5) to express the growth of tumors modeled in reference [34]. The cases are: tumor cells in vitro (9L, SNB19 and U118), as well as those in vivo for rodents (Fibro, Walker, KHJJ, C3H, EMT6, NCTC2472, Osteo, C33ISS) and for patients (breast tumor and prostate tumor). Table 3.2.1 shows the parameters for various tumors.

Table 3.2.1 Values of some tumor parameters [34]

Tumor	SNB19	Fibro	Walker	KHJJ	C3H	EMT6	NCTC2472	Osteo	C3H ISS	Human breast	Human prostate
$\beta_T°$ (day $^{-1}$)	0.057	0.037	0.440	0.19	0.14	0.38	0.30	0.0762	0.22	0.16	0.083
m_{T0}(g)[34]	0.025	1	0.348	.0012	.0348	.00135	0.052	0.0058	0.2	1	1
M_T(g)[34]	3	200	150	2	5	3	7	7	8	646	641

Let $r=(m_T/M_T)^{1/4}$ and $\tau=\frac{1}{4}\beta_T°t-\ln[1-(m_{T0}/M_T)^{1/4}]$. Equation (3.2.5) is reduced to $r=1-\exp(-\tau)$. It fits the curves that Guiot et al. present in reference [34]. Here we introduce them into Fig. 3.2.1.

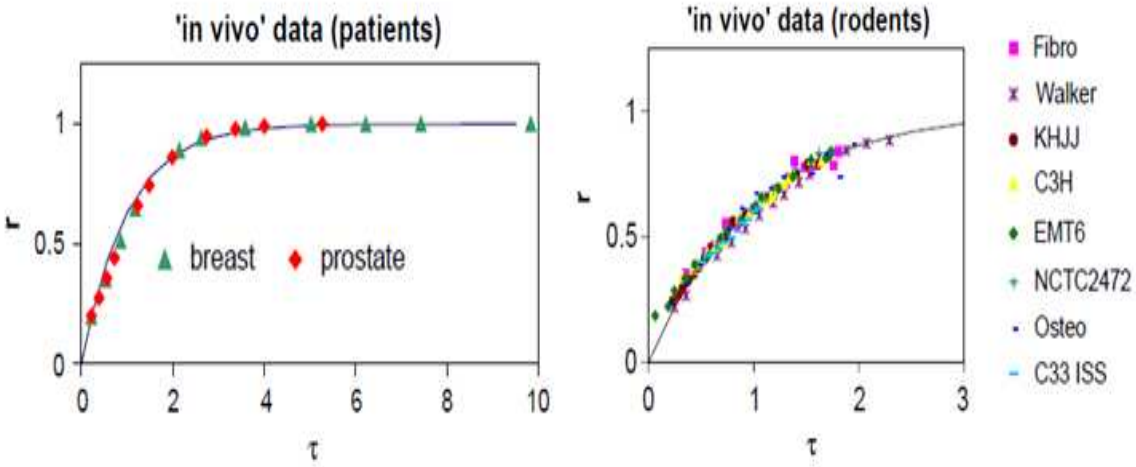

Fig. 3.2.1 Tumor growth curves (real line curves represent r =1-exp(-τ)) [34]

In other cases, since different tumor cells do not have the same β°, they cannot be unified by the rules of similarity of growth. We cannot express the total tumor mass in a uniform equation. Instead, we must find the solutions separately and then add them together. In this case, the growth process is complex, though each set of identical cells still follow the growth law for organisms in its own way. It is even more complicated when tumor cells metastasize to different locations and have different growth rates in various systems, especially when the growth time is asynchronous.

3.2.2 Secondary Tumor Growth

Despite the fact that no tumor cell can flow or diffuse into a primary tumor from the outside, some may flow out or diffuse into either blood vessels or lymphs once the tumor reaches a certain size. Some of them will be carried out of the primary tumor or even transported to other normal organs where the conditions are better for their growth (i.e. passive and active transport). This process should be related to the transport path and the environment. However, once a "seed" is planted into good "soil", the growth process of this secondary tumor should follow the same pattern/equation as that of primary tumor growth. However, parameters such as number density, death and production rates may not be the same. Demidem et al. [96] studied the growth of secondary tumors and found that their growth curves also fit the "Gompertz" function. We use equation (3.2.5) to perform curve fitting for the data in Ref. [96]. The result is shown in Fig. 3.2.2. The symbol "♦" represents data that we obtained from Fig. 6 of Ref. 96 by measuring the coordinates (We choose this particular one as an example of a complex system). The curve represents equation (3.2.5). They fit rather well when some parameters are chosen. Here we let the first experimental point be the initial point.

The complexity is that the suitable “soil” and paths between the source (primary tumor) and the “soil” may cause more than one “seed” to grow in that location. Also, the growth of these metastases will likely not follow the rules for similarities of growth.

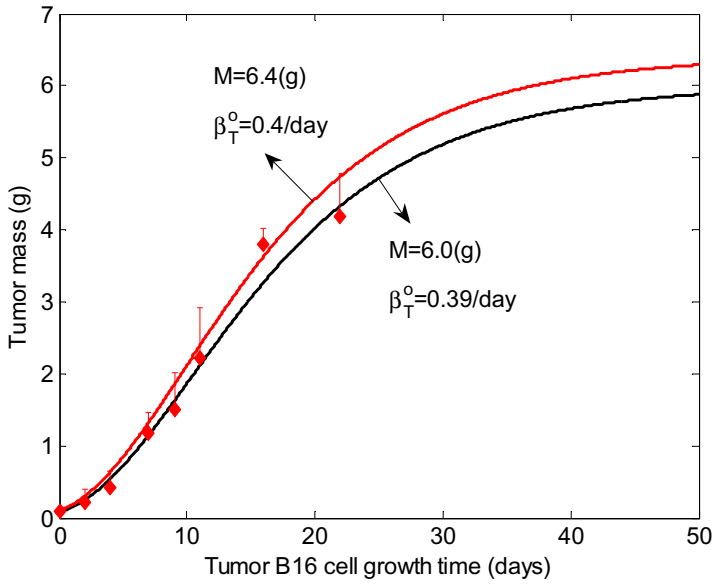

Fig. 3.2.2 Growth curves of a secondary tumor

3.2.3 Tumor Metastasis

When metastasis occurs in a primary tumor, some cells flow out of the system. Therefore, assuming that all tumor cells spread out of the system, no cells can flow in. A mass flux exists and equation (3.1.1) must be modified to:

$$\frac{m_{ck}C_k dV_k}{dt} = -C_k m_{ck} \oiint \vec{u}_k \cdot d\vec{A}_k + V_k m_{ck}(\bar{S}_k - E_k) \tag{3.2.6}$$

$$-C_k m_{ck}\int \nabla_k \cdot \vec{u}_k dV_k = -C_k m_{ck}\oiint \vec{u}_k \cdot d\vec{A}_k + cons. \quad \text{(Divergence theorem)}$$

where $\vec{u}_k$ is the velocity of cells spreading out of the tumor in system k, A_k is the closed surface of V_k and the direction of $\vec{A}_k$ is the outward-pointing normal of A_k. Equation (3.1.3) should still be satisfied if the nutrition supply and growth environment do not change. Since $\vec{u}_k$ is usually spatially and temporally dependent, there is no analytic solution. Here we consider two simple cases:

1) The outflow rate of tumor mass is a constant μ (u is a constant) and there is only one kind of tumor cell. Then, eq. (3.2.6) can be rewritten as:

$$\frac{dm_T}{dt} = -\mu + \beta_T \circ m_T \left[\left(\frac{M_T}{m_T} \right)^{1/4} - 1 \right] \tag{3.2.7}$$

There is an equilibrium mass M_{eq}. When $m_T = M_{\text{eq}}$, $\mathrm{d}m_T/\mathrm{d}t = 0$, which means the primary tumor will not grow. When $m_T > M_{\text{eq}}$, $\mathrm{d}m_T/\mathrm{d}t < 0$, and the primary tumor decreases. The "unknown primary origin" cancers [111, 112] may relate to this case. When $m_T < M_{\text{eq}}$, $\mathrm{d}m_T/\mathrm{d}t > 0$, causing the primary tumor to increase until it reaches a specific size. M_{eq} satisfies the following equation:

$$\beta_T \circ M_{eq} - \beta_T \circ M_T^{1/4} M_{eq}^{3/4} + \mu = 0 \tag{3.2.8}$$

This case may not be maintained if there is no external force.

2) $\nabla \cdot \vec{u} = cons.$ This causes the outflow rate of tumor mass to be proportional to the mass. This case is still for one type of tumor cell. Now equation (3.2.6) can be rewritten as:

$$\frac{dm_T}{dt} = -\mu m_T + \beta_T \circ m_T \left[\left(\frac{M_T}{m_T} \right)^{1/4} - 1 \right] \tag{3.2.9}$$

where μ is a proportionality constant. Let $\mathrm{d}m_T/\mathrm{d}t = 0$, we can find the equilibrium mass M_{eq},

$$M_{eq} = \left(\frac{\beta_T^{\circ}}{\beta_T^{\circ} + \mu} \right)^4 M_T \tag{3.2.10}$$

3.2.4 Modification of Tumor Mass

When a tumor grows to a specific stage, it connects to other systems through blood vessels, lymphs etc. Fluid flows in and out in a balanced way in normal tissues. This maintains a normal metabolism. The balance may be upset in tumors and we must consider the issue of net inflow. In a primary tumor, the fluid that comes from blood vessels does not proliferate and eq. (3.2.6) is simplified to:

$$\frac{\partial V_F}{\partial t} = -\oiint \vec{u}_F \cdot d\vec{A}_F \tag{3.2.11}$$

Solving equation (3.2.11) depends on the distribution and direction of the fluid's velocity on the closed surface of the volume. The high capillary permeability and low lymphatic drainage of a tumor may cause fluid accumulation. According to Starling's law, the net fluid flux across the capillary walls is expressed as:

$$J = LA(p_V - p - \Delta p_O) \tag{3.2.12}$$

where L is the hydraulic conductivity of the capillaries, A their surface area, p_v the vascular fluid pressure (pressure in the capillaries), p the interstitial fluid pressure, and Δp_o the osmotic pressure difference. Here we consider a very simple situation by assuming that all fluid is accumulated in the tumor area. Then,

$$V_F(t) = \int_0^t J dt = \int_0^t LA(p_V - p - \Delta p_O) dt \tag{3.2.13}$$

While spreading, the fluid meets resistance from the environment. We suppose that the pressure $p(t)$ is proportional to the amount of accumulated fluid [72].

$$p(t) = \gamma V_F(t) = \gamma \int_0^t LA[p_V - p(t) - \Delta p_O]dt \tag{3.2.14}$$

where γ is a proportionality coefficient. The differential form of equation (3.2.14) is

$$\frac{dp(t)}{dt} = \gamma LA[p_V - p(t) - \Delta p_O] \tag{3.2.15}$$

In the beginning, fluid flows in and out of the tumor in a balanced way, so there is no accumulated fluid. The initial value of IFP is zero, which is the same as that of normal tissue. So,

$$p(t) = (p_V - \Delta p_O)(1 - e^{-\gamma LAt}) \tag{3.2.16}$$

Comparing equations (3.2.11) and (3.2.13), we can get the direction of the normal component of fluid velocity:

$$u_{F\perp}(t) = L(p_V - \Delta p_O - p) = L(p_V - \Delta p_O)e^{-\gamma LAt} = u_0 e^{-\gamma LAt} \tag{3.2.17}$$

And $$m_F(t) = m_{cF} C_F V_F(t) = \frac{m_{cF} C_F (p_V - p_0)}{\gamma}(1 - e^{-\gamma LAt}) \tag{3.2.18}$$

Note that the starting point in time for tumor mass and fluid mass may not be the same. Suppose that m_F starts to accumulate t_0 units later than the tumor (it may depend on the condition of the interface between tumor and normal tissues). The total mass of a tumor can be expressed as:

$$m_t(t) = \begin{cases} m_N(t) + m_T(t) & t \le t_0 \\ m_N(t) + m_T(t) + m_F(t - t_0) & t > t_0 \end{cases} \tag{3.2.19}$$

Tumor growth and fluid flow follow different laws. Therefore, unbalanced fluid flux causes the growth of some tumors in certain growth processes to not completely follow the “universal” law for organism growth. At steady state, the fluid leaked out from the vasculature is balanced with that which flows out of the tumor. The amount of fluid accumulated in the tumor is fixed.

3.3 Application to Tumor Therapy

There are three widely used therapies for tumor treatment: surgery, radiation and chemotherapy. Each has its own properties and can be modelled. Different from conventional chemotherapy, antiangiogenic therapies like metronomic chemotherapy is a relatively new and promising treatment. However, its mechanisms are not completely clear, though we know it works by controlling vasculature growth. Cell survival response to these therapies is still a popular topic. Many experimental data cannot be explained by applying the existing models. How to combine these therapies to benefit patients the most is still being debated.

All therapies are designed to reduce tumor growth, either directly or indirectly, and can be modeled by tumor cell production and death rate as well as flux term. Radiation therapy and conventional chemotherapy change the death rate, whereas antiangiogenic therapy controls the production rate. The effect of surgery is different. It changes the mass of the tumor directly so that the growth rate is negatively and drastically changed, though the death rate may not be affected. These therapies have different mechanics and should be discussed separately. The therapeutic approaches are modeled mathematically in this section.

3.3.1 Surgical Therapy

The response of a tumor following surgery is the immediate loss of most of the cells that comprised the tumor. Often, the growth rate of a tumor after surgery is greater than that of the original tumor [113]. To model the loss of tumor mass through surgery, assume

that the removed tumor mass is M_R. Assuming all tumor cells are identical, the governing equation for the growth of remaining cells can be expressed as:

$$\frac{dm}{dt} = \frac{E(m - M_R)}{C}\left[\left(\frac{M}{m - M_R}\right)^{1/4} - 1\right] \tag{3.3.1}$$

Focusing on the growth process of the remaining cells after surgery, the following transformation can be made: $m' = m - M_R$, where m' follows equation (3.1.4). If $M_R = m$, it means that the surgery has effectively eliminated all tumor cells, so $dm'/dt = 0$. In this case, the tumor will not grow any more. On the other hand, if some tumor cells remain, they will grow, typically at an accelerated rate. Even so, the growth rate dm'/dt may be very small if the remaining mass is very small. For example, a fibro tumor with M =200g, m=150g before surgery has a remaining mass $m' = m - M_R$=1/1000g after the operation. The production rate before surgery (m=150g) is $\bar{S} \approx 1.075E$ (unit) and the growth rate is dm/dt =11.2E/C. The production rate after surgery becomes $\bar{S}' \approx 21.15E$ (unit) and the growth rate becomes dm'/dt=0.020E/C. Only when the remaining mass is (81/256)M can the growth rate be maximum, which is (27/256)ME/C. Therefore, whether the growth rate of a tumor after surgery is greater or smaller than the original tumor's growth rate depends on the time and amount of tumor removed. If surgery is applied when the tumor is mature, the growth rate of a tumor after surgery will likely be greater than the original tumor growth rate.

3.3.2 Radiation Therapy

When ionizing radiations such as x-rays or α-particles interact with cells in a bio-system, some kinetic energy is being deposited in the system causing possible damage. Linear energy transfer (LET) is the measure of the energy deposited per unit length (kev/μm) of the radiation/particles' track [10]. Depending on the value of LET, ionizing radiation may be divided into two types: low and high LET emissions. For cell response to a low LET

radiation such as x-ray, the linear quadratic (LQ) model is widely used [10, 40, 50, 114]. Many survival curves fit the LQ or two component LQ model [50]. However, many researchers noted that the LQ model does not fit the survival curves well, especially in the high dose region [40-42, 44, 45].

Unlike x-ray, alpha particle emission causes a linear survival curve in most cases [10,115,116]. Barendsen et al. [115] studied human cell response and corresponding oxygen-enhancement ratios (OER, which is the ratio of doses administered under hypoxic to aerated conditions needed to achieve the same biological effect) to α-particles with different energy. Instead of using air, Barendsen et al. used nitrogen for hypoxic condition. The results are summarized in table 3.3.1.

Table 3.3.1 Biological effect of human cells after α-particles radiation

Energy (Mev)	2.5	3.4	4.0	5.1	8.3	25
LET (kev/μm)	166±20	140±20	110±10	88±6	61±5	26±2
OER	1.0±0.1	1.1±0.05	1.3±0.1	1.7±0.15	2.05±0.25	2.4±0.3
$\log_{10}(SF)$~D fit	linear	linear	linear	linear	linear	LQ

LET increases to 166kev/μm while the kinetic energy of each particle decreases to 2.5Mev. Correspondingly, OER decreases to 1.0. The survival curves fit almost linearly when the kinetic energy is less than 8.3 Mev and LET is greater than 61kev/μm. An α-particle has a typical energy of 5 Mev (usually between 3-7 Mev) and is composed of two protons and two neutrons. Relative to other particles such as neutrons, protons and electrons, α-particle is of a large size and mass, which make it have low penetration depth. Therefore, the energy of α-particles is absorbed by tissues (cells) within a short range. This makes it extremely dangerous once the source is ingested or inhaled since all the particles stay. The damage of biological effects is about 20 times as that caused by an equivalent amount of gamma or beta radiation (e.g. number of cells killed in 1Gy =1J/kg dose). While interacting with cells, α-particle transfers most of its energy in a small region. Therefore, the localized DNA damage is difficult to repair or is even irreparable. Studies [10, 115] show that the OER is 1.0 when LET is greater than 165 kev/μm. Generally, the OER decreases with the increase of LET [117]. When LET is between 61 and 110 kev/μm, the OER is from 2.0 to 1.3, though the survival response is still linear.

When LET reduces to 26 kev/μm, the OER increases to 2.4 and the survival curve shows features of the LQ model.

Assuming that a double strand break in the DNA helix is the critical damage, Chadwick and Leenhouts statistically derived the LQ equation and approximated it as [114]:

$$SF = \exp[-k_1 \Delta D - k_2 (1-\Delta)^2 D^2] \tag{3.3.2}$$

where SF represents cell surviving fraction, k_1, k_2 are two constants, D is the absorbed dose; Δ is a proportion of dose D that is inactivated via single event killing (meaning both strands of the DNA double helix are broken in one radiation event), and 1-Δ is the proportion that is inactivated via double event killing (meaning each strand of DNA double helix is broken independently during different radiation events). Here Δ is LET related. This model implied that Δ increases when LET increases. The linear term exp(-$k_1\Delta D$) dominates survival at low doses. With increase in LET or Δ, the quadratic term exp[-k_2(1-Δ)$^2D^2$] plays an increasing role [114]. The LQ model may be applied for cell response to high LET radiations such as α-particles if the quadratic term is ignored.

However, there are some experimental data that do not fit the LQ model (including the linear limitation) and its multi-component forms. For cell response to α radiation, many survival curves fit a linear line and some might follow the LQ model, while other survival curves do not belong to either of these two cases. For example, Hieber et al. [118] showed that the response of C3H 10T1/2 cells to α radiation deviates upward from the linear line after 1.5 Gy. Beaton et al.'s experiment for A-549s's cell response to α radiation [119] showed a similar result. According to the description for setting up the experiments, the results could not be merely explained as "unattached mitotic cells not reached by the α-particles". From the experimental result given by Durante [120] for H184B5 F5-1 M/10 cell response to α-particles, we can also summarize that the curve is different from either the linear or the LQ model. Some additional experiments [116, 121-125] also showed that the survival curves deviate upwards from a linear line. Some experimental results, such as the survival of asynchronous V79 cells vs. DNA-incorporated activity [126] after 30-min exposure to ^{211}AtdU (5-[211At]astato-2'-deoxyuridine), may be explained by introducing the two-component exponential model

[126, 127]. However, the experimental data in references [118] and [119] do not fit the linear model, its two-component form or any other previous model. For cell response to x-ray radiation, Powers and Tolmach [54] reported the survival of subcutaneous 6C3HED mouse lymphosarcomas and suggested that the survival kinetics were determined mainly by two cell populations. Even so, no existing models fit the survival curve, including the two-population LQ model. Explaining all these survival curves consistently may lead us to propose a general model for cell response to radiation. In fact, all previous models are derived from statistical theory. In the LQ model, the surviving fraction is expressed as $SF = e^{-\alpha D - \beta D^2}$, where α and β are two parameters that are determined by cell response. It is assumed that the factor $e^{-\alpha D}$ comes from single event killing, and the factor $e^{-\beta D^2}$ is derived from double event killing [10, 114]. This implies that high LET radiations such as α-particles cause mainly single event killing. In fact, alpha radiation causes more serious damage to cell nuclei (mainly DNA) than other kind of radiations. High LET radiation increases the complexity of lesions due to the formation of multiply damaged sites [128]. The damage caused by DNA double strand breaks are considered important, and can be seen from evidence relating to cell lethality [128, 129]. In addition, when dose or dose rate is zero, a model for cell response to therapy should be compatible with the natural growth or death process before treatment is applied. However, previous models did not relate to this aspect.

Damage to DNA such that proliferating cells lose reproductive integrity (often after a few cell divisions) is the cause of radiation cytotoxicity. The effect of radiation depends on conditions such as radiation dose, the fractionation schedule and environmental conditions, particularly the oxygen partial pressure of cells. Killing cells through radiation is not a direct process of removal of mass like surgery, but rather the indirect removal of mass via cell loss processes such as necrosis, apoptosis, and autophagy. No matter what the detailed procedure is, it results in the death of cells and the decrease in growth rate. We assume that the average additional death rate caused by radiation during treatment period is $\overline{K}$. It represents the average additional number of dead cells in a unit volume per unit time. It is noteworthy that cells, and by extension organisms, have a smaller death rate when they grow or die/shrink with no radiation or chemotherapy

applied. The treatments cause additional death rate. If the production rate is greater than the total death rate, an organism grows; otherwise, it shrinks or even dies. Here, we are only interested in the behaviour of tumor cells and view all tumor cells as the same. Namely, for a uniform system composed of identical cells that respond equally to radiation. Thus, when treatment is applied, the equation for tumor cell growth is amended to read:

$$\frac{dm}{dt} = \frac{m}{C}\left[E\left(\frac{M}{m}\right)^{1/4} - E - \overline{K} \right] \tag{3.3.3}$$

This is a general expression for cell response to treatment. For radiation such as x-rays and α-particles, the dose in a unit time (dose rate) can be selected or controlled and set as a constant since the energy per particle and the distance of target are fixed (dose rate $\dot{D} = dD/dt$ is set as a constant, where D represents radiation dose and mainly uses Gy=J/kg as its unit. If dose rate is not a constant [44, 45], the additional death rate will be complicated and we will not discuss it here). In a specific treatment period, the average dose rate is practically a constant. Therefore, the dose absorbed by an organism or a cell system is proportional to the amount of time it is exposed to radiation ($D = \dot{D}t$). We employ a general relation $t = \lambda D$, where g is the reciprocal of dose rate. Thus, eq. (3.3.3) becomes:

$$\frac{dm}{dD} = \frac{m\lambda}{C}\left[E\left(\frac{M}{m}\right)^{1/4} - E - K \right] \tag{3.3.4}$$

K is a key parameter for determining the survival response. Different cell "killing" styles may give various patterns of K. A correct pattern should reflect the experimental results. Here we discuss three cases (according to the LET value).

a) When LET is greater than a specific value L_0 (LET>L_0) in a given cell system, the energy deposited is large enough to destroy all localized cells present equally (regardless whether the cells are hypoxic or oxygenated). The damage done to most cells is irreparable, or more accurately, the number of repairable damaged cells is much less than that of the irreparable ones. Therefore, the number of repairable cells may be ignored.

The additional death rates are proportional to the quantity of cells present, which should be constant since the cell density is constant. In this case, the OER is equal to 1.0.

b) When LET is smaller than L_0 but greater than a given value L_1 (L_1<LET<L_0), the energy deposited is still large enough to cause serious damage immediately while interacting with cells and most damage is still irreparable. However, the energy deposited is not large enough to destroy all localized cells with the same effect. It is oxygen dependent. The damage under well-oxygenated condition is larger than that under hypoxic condition. The ratio of damage varies from one fold to nearly three folds. The exact value for a given cell system is LET dependent [10, 115, 117]. The number of cells killed is still proportional to the number of cells present, but the proportionality varies for cells under normoxic and hypoxic conditions. Therefore, the additional death rate is still constant (though the value is oxygen dependent) since the number density of cells is constant. In this case, the OER is greater than 1.0.

c) When LET is smaller than L_1 (LET<L_1), the energy deposited is not large enough to destroy all localized cells immediately. The mechanism of cell killing is the same as that for cells under low LET radiation. There is a time accumulating effect. We classify it as a linear-quadratic case.

We accept the view that DNA double strand breaks cause critical damage to cell proliferation. In cases a) and b), the LET is large enough such that the localized nuclei of cells are damaged by breaking DNA double–strands immediately. There is no time accumulating effect. In this case, the additional death rate caused by α-particles is proportional to the cells present. For a specific kind of cell, the number density C is fixed. Thus, the additional death rate is a constant ($K=\nu$). The solution of eq. (3.3.4) is:

$$E-(E+\nu)\left(\frac{m}{M}\right)^{1/4}=[E-(E+\nu)\left(\frac{M_0}{M}\right)^{1/4}]\exp(-\frac{E+\nu}{4C}\lambda D) \tag{3.3.5}$$

The surviving fraction is

$$SF=\frac{m}{M_0}=\frac{M}{M_0(E+\nu)^4}\{E-[E-(E+\nu)(\frac{M_0}{M})^{1/4}]\exp(-\frac{E+\nu}{4C}\lambda D)\}^4 \tag{3.3.5′}$$

where M_0 is the mass of cells when radiation starts. In actuality, M_0/M can be determined theoretically by comparing two identical cell systems. Radiation is applied to one but not

the other. Usually, the additional death rate caused by alpha radiation is much greater than the production rate in a cell system, namely $(E+\nu)(m/M)^{1/4} >> E$ is satisfied. In this case, it gives an approximately linear cell survival curve and is expressed as

$$SF = \frac{m}{M_0} = \exp(-\frac{E+\nu}{C}\lambda D) \qquad (3.3.5'')$$

Fig. 3.3.1 depicts log(SF) vs. D with various values of $E\lambda/(4C)$, $\nu\lambda/(4C)$ and M_0 based on eq. (3.3.5′).

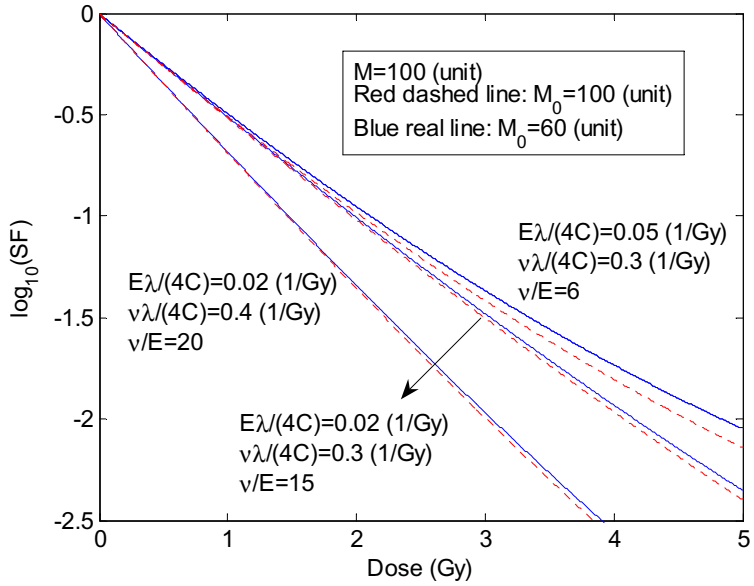

Fig. 3.3.1 General cell response to α-particle radiation with different parameters

Regarding cell response to α-particle radiation, the present model is compatible with all existing models. However, for C3H 10T1/2 cell response to α radiation given in reference [118], the experimental data cannot be fitted by any previous models, even considering the form for two component cell system. The energy of α-particles is 2.7Mev, their dose mean is LET 147 kev/μm, and frequency mean of LET is 144 kev/μm. When we apply eq. (3.3.5′) to the experimental data, it fits well. According to the description of the experiment, the abnormal experimental result cannot be explained due to the fact that unattached mitotic cells cannot be reached by the α-particles. Here we choose M_0/M=25%

since the plating efficiency of control cultures in the experiment was 20-30%. The result is shown in Fig. 3.3.2.

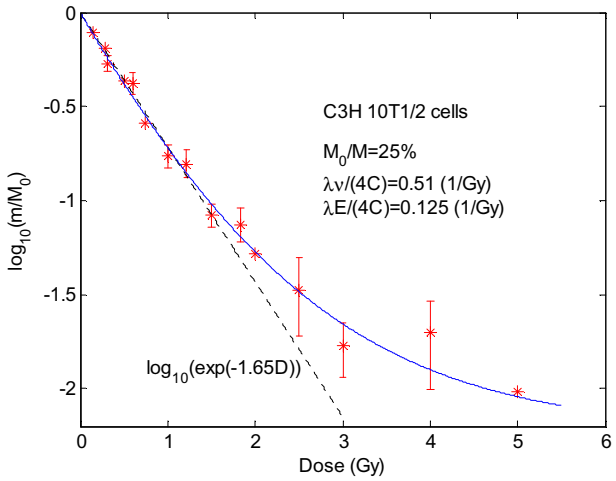

Fig. 3.3.2 C3H 10T1/2 cell response to α-particle radiation

Similarly, for A-549s's cell response to α-particle radiation in reference [119], the survival curve deviates away from the linear line. The last experimental point does not fit a linear response at all. However, eq. (3.3.5′) fits the experimental points well, which is shown in Fig. 3.3.3.

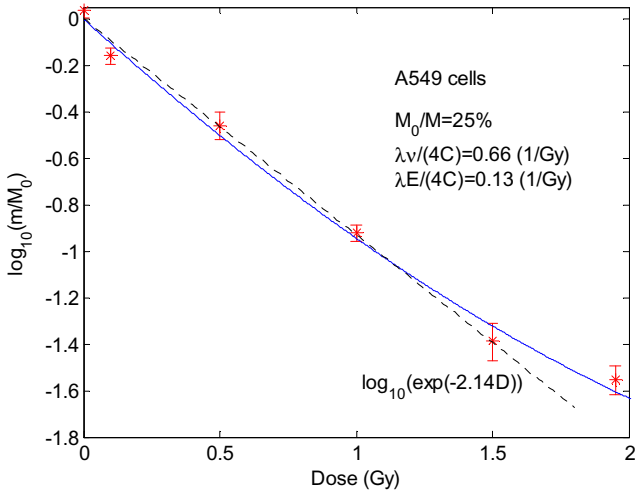

Fig. 3.3.3 A549s cell response to α-particle radiation

For H184B5 F5-1 M/10's cell response to α-particle radiation in reference [120], we can see that a linear line does not fit some experimental points well. Eq. (3.3.5′) fits the experimental points better, as show in Fig. 3.3.4.

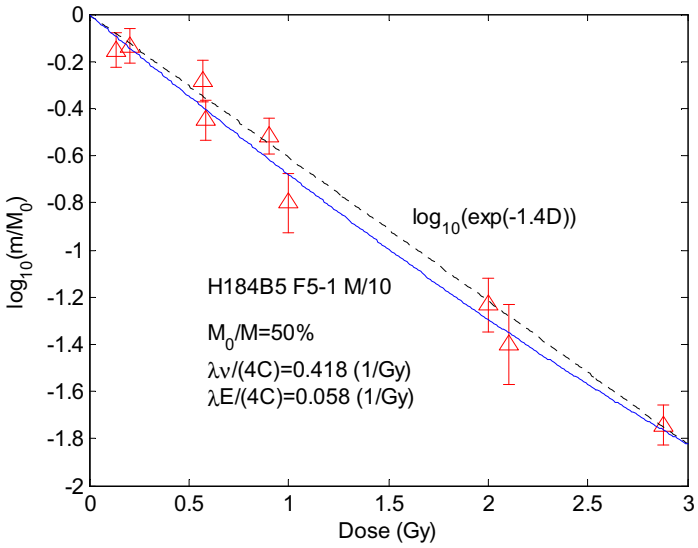

Fig. 3.3.4 H184B5 F5-1 M/10 cell response to α-particle radiation

For comparison, here we calculate the root-mean-square (RMS) differences based on the formula $RMS=\sqrt{\frac{1}{m}\sum_{i=1}^{m}(\log SF_i-\log SF_{fit})^2}$ [50]. We also calculate $\chi^2=\sum_{i=1}^{m}\frac{(\log SF_i-\log SF_{fit})^2}{\sigma_i^2}$ if we know the variance of each experimental point, where σ_i represents the variance of $\log SF_i$. We do so since the increments of $\log SF$ are equally spaced and the differences of $\log SF_i$-$\log SF_{\rm fit}$ are "more easily correlated to the goodness of fit that is visually apparent in the usual semi-log plot of SF vs. D [50]". The results are listed in table 3.3.2. It shows that the present model fits the curves better.

Table 3.3.2 The goodness of linear fit and the fit of the present model

Cells	The present model (free fit)		The linear fit	
	RMS	χ^2	RMS	χ^2
A549s	0.0464	5.69	0.110	22.28
H184B5	0.0730	5.416	0.0888	5.717

For case c), the transferred energy is not large enough to damage some of the targeted nuclei immediately. The DNA damage of nuclei has a time accumulating effect. Since the energy deposited is not large enough, one attack does not break DNA double strands, so there is no serious damage to cells. With time accumulating, the number of DNA double strand breaks increases. The damage of some cells is proportional to the time. Therefore, the additional death rate also has a time accumulating effect. Mathematically, the LQ model is equivalent to the equation $dN/N = -(\alpha + 2\beta D)dD$. The constant term α creates surviving fraction proportional factor $e^{-\alpha D}$, which is assumed to originate from single event killing. The term $2\beta D$ causes surviving fraction proportional factor $e^{-\beta D^2}$ and is assumed to be derived from double event killing [10, 114]. In fact, the term $2\beta D$ contains the time accumulating effect since $D = \dot{D}t$. Also, accumulation of DNA single strand break can cause DNA double helix break. Studies show that α-particles cause much more serious damage in the nuclei than low LET radiations, such as x-ray [10]. DNA double strand breaks are the primary critical lesion for cell killing [128, 129]. Considering these effects, we assume that some of the nuclei are damaged immediately, causing a constant additional death rate ν, while others are damaged gradually under low LET radiation. With time or radiation dose accumulating, more and more DNA double strands are broken and nuclei are damaged correspondingly, which causes on average an additional death rate κD. Therefore the total additional death rate in this case is expressed as $K = \kappa D + \nu$, where κ and ν are two constants for a specific radiation and target. Now we rewrite eq. (3.3.3) as:

$$\frac{dm}{dD} = \frac{\lambda m}{C}\left[E\left(\frac{M}{m}\right)^{1/4} - E - \kappa D - \nu\right] \tag{3.3.6}$$

The complete solution can be expressed by using the confluent hypergeometric function, or it can be given numerically. However, in radiation, the conditions $\overline{K} >> \overline{S} = E(M/m)^{1/4}$ and $\overline{K} >> E$ are usually satisfied. Then, equation (3.3.7) is reduced to:

$$\frac{dm}{dD} = -\frac{\lambda}{C} m(\kappa D + \nu) \tag{3.3.7}$$

The solution is:

$$SF = \exp[-\lambda(\tfrac{1}{2}\kappa D^2 + \nu D)/C] \tag{3.3.8}$$

By way of comparison, we have:

$$\alpha = \nu\lambda / C\,,\ \beta = \tfrac{1}{2}\kappa\lambda / C\,,\ \alpha/\beta = 2\nu/\kappa\,.$$

The α, β and C are fixed for a specific target. Therefore, smaller λ (corresponding to a larger dose rate $\dot{D}$) causes larger κ and ν. Besides using α-particles, Barendsen et al. [115] also used deuterons and neutrons to irradiate T-1g cells in culture under oxygenated condition (with air) and hypoxic condition (with nitrogen). For deuterons, when the LET is 20kev/μm, the survival curves are almost straight lines. However, when the LET is 5.6kev/μm, they are not straight anymore. Here we apply the LQ model (eq. 3.3.8) to fit the experimental data. The result is shown in Fig. 3.3.5. Similarly, for the survival curves under 25 Mev α-particles with LET 26±2kev/μm, they cannot be fitted linearly, especially for the survival curve under hypoxic condition. We use the LQ model to fit the survival curves. The result is shown in Fig. 3.3.6. Obviously, it shows that the survival curves' response to heavy particles such as α-particles and deuterons also have the characteristics of x-ray when LET is low.

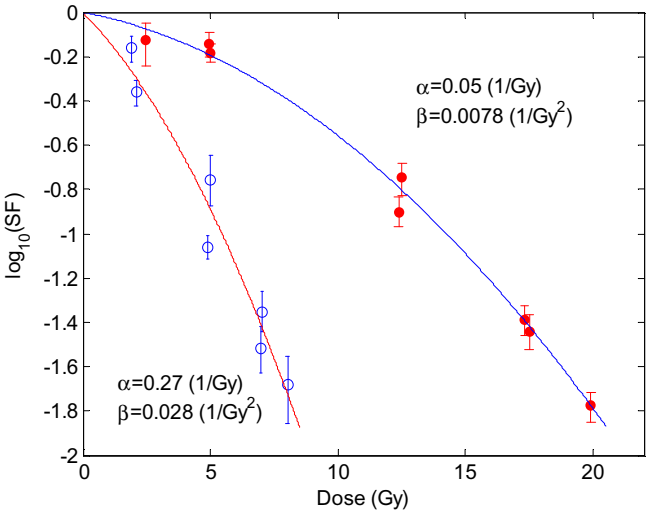

Fig. 3.3.5 T-1g cell response to deuterons (14.9Mev) with air (open circles) and nitrogen (closed circles). LET: 5.6±0.3kev/μm; OER: 2.6±0.3

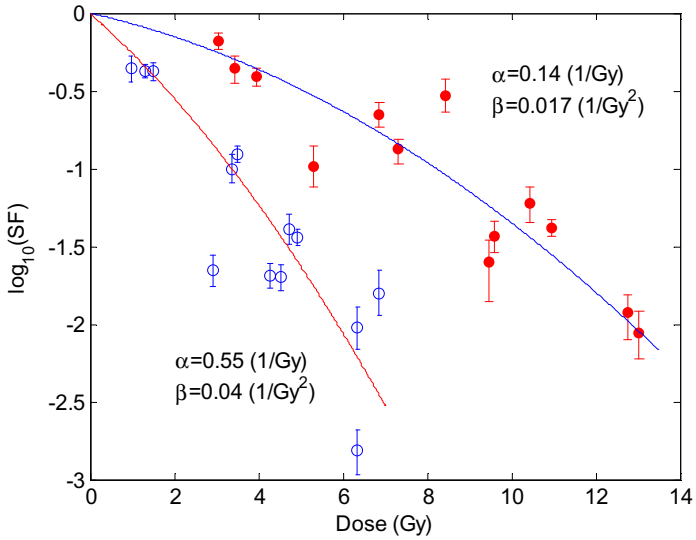

Fig. 3.3.6 T-1g cell response to α-particles (25Mev) with air (open circles) and nitrogen (closed circles). LET: 26±2kev/μm; OER: 2.4±0.3

For a multicell system, different kinds of cells (which grew harmoniously before therapy) may have different λ/C, but they have the same or proportional value of ν to κ (and correspondingly α to β) under equal radiation or chemotherapeutic treatment with identical environmental conditions. It means that the additional death rates of different populations should be equal or proportional when they are under the same radiation field or chemotherapeutic agent treatment. Though ν and κ are still variables dependent on specific tumors and radiation conditions, they relate both α and β (and correspondingly the response to radiation therapy) to the number density of tumor cells, C.

As we know, a small fraction of radioresistant cells can change the survival curves significantly. We consider a general situation. Suppose a system is composed of more than one type of cell. For the sake of convenience, we take two different kinds of cells as an example, one "regular" and the other "resistant". Let the fraction of "resistant" cells be x (making the fraction of "regular" cells 1-x). Similarly, we can also use this method if there are more than two types of cells. If there are only "regular" cells, x=0. For convenience's sake, we use subscript 1 to represent "regular" cells and 2 for "resistant"

ones. The initial amount of cells in the system is M_0. The final amount of cell 1 is m_1 and cell 2 is m_2. Here M_0, m_1 and m_2 can be the mass or number of cells since the mass of identical cells is proportional to the number of cells. Fraction 1-x and x must coincide with $m_{01}=M_0(1-x)$ and $m_{02}=xM_0$ respectively. It is easy to show that the fractions of different cells in a system before therapy (K=0) are constant if various cells have the same E/C and their asymptotic masses share the same fractions. These two conditions (E_k/C_k constant and $M_k=xM$) ensure that the cells grow harmoniously before treatment. The different responses to therapy enable us to detect the existence of various cell subpopulations. If radiation is applied, the surviving fractions for cell 1 and cell 2 can be expressed respectively as:

$$(SF)_1=\frac{m_1}{M_0(1-x)}=\exp[-\gamma_1(\alpha+\beta D)D] \tag{3.3.8′}$$

$$(SF)_2=\frac{m_2}{M_0 x}=\exp[-\gamma_2(\alpha+\beta D)D] \tag{3.3.8″}$$

Here, we use the same α and β for both cells 1 and 2 since they are subjected to the same radiation field; γ_1 and γ_2 are two relative coefficients which reflect the different responses of dissimilar cells to radiation. We can set γ_1=1 and ignore the subscript of γ_2. Then, the total surviving fraction of the system is:

$$SF=\frac{m_1+m_2}{M_0}=(1-x)\exp[-(\alpha+\beta D)D]+x\exp[-\gamma(\alpha+\beta D)D] \tag{3.3.9}$$

Eq. (3.3.9) is the same as eq. (2.12) under the condition that $\alpha_s/\beta_s=\alpha_r/\beta_r$. In Ref. [50], the authors applied eq. (2.12) to fit the experimental data. They expected approximately comparable numbers of sensitive and resistant cells in their experiment. Setting x=0.5, they found that α_s=0.2414, β_s=0.1006, α_r=0.0886, and β_r=0.0345. Thus, α_s/β_s=2.40 and α_r/β_r=2.57, which are close. The difference might be because the fractions of the two components are not exactly the same. In the free fitting case, they found that x=0.63, α_s=0.2064, β_s=0.1218, α_r=0.1402, and β_r=0.0318, which gives α_s/β_s=2.69 and α_r/β_r=4.41. The authors also tried a forced fit by letting x=0.37, and found that α_s=0.2492, β_s=0.0874,

α_r=0.0231, and β_r=0.0378, which gives α_s/β_s=2.85 and α_r/β_r=0.611. The values of α_s/β_s and α_r/β_r in these two cases are distinctly different.

Based on the discussion above, we use the same α and β for different cell populations in eq. (3.3.9). The difference in response is reflected by γ. This makes the model that we have presented different from any other two- or multi-component LQ model [50-53]. Those models may give various cell fraction x by choosing different values of α and β [50], due to the fact that the αs and βs for different cell populations are not constrained. In the present model, since the αs and βs are constrained, only a unique x can give the best fit. In some cases, when the production rate is large, we may have to solve eq. (3.3.3)/(3.3.4) or (3.3.6) to find the surviving fraction. Because the value γ has an exponential effect on the surviving fraction, it may have a strong influence on the surviving fraction of the entire system. Fig. 3.3.7 shows this state of affairs. In fact, the red curve shows common features of many different radiation survival curves.

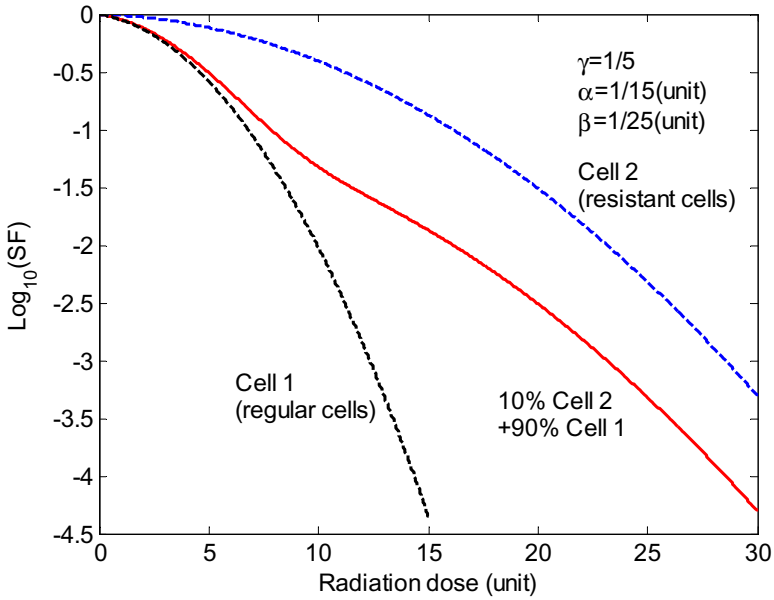

Fig. 3.3.7 Comparison of the survival curves of cell 1, cell 2 and a mixture of both

If we rewrite eq. (3.3.9) in the form of the LQ equation,

$$e^{-(\alpha'+\beta' D)D} = (1-x)e^{-(\alpha+\beta D)D} + xe^{-\gamma(\alpha+\beta D)D}$$

we get:

$$\alpha' D + \beta' D^2 = \alpha D + \beta D^2 - \ln[1 - x + xe^{(1-\gamma)(\alpha+\beta D)D}]$$

Obviously, α' and β' are the functions of α, β, γ, x and D. For a specific species and radiation field, α, β, γ, and x are fixed. Therefore, α' and β' are functions of D. Many models introduce a G factor to the term β'.

We must consider two components of cell population in order to fit the survival curves for radiation. To correctly determine the fractions of each cell population, we need accurate experimental data. Astrahan plotted Elkind and Sutton's experimental data [46] into an enlarged logarithmic coordinate system to show that Chinese hamster cells in culture closely fit the LQ model up to a dose of 6 Gy, but then starts to deviate from the LQ curve [40]. Here we use the data from reference [40] and fit the curve based on equation (3.3.9). The results are shown in Fig. 3.3.8 with the best fit curves. We also tried x=0.04, but we do not show it in this graph for the sake of clarity. It is close to the case where x=0.05. Fig. 3.3.8 shows that the curves for $x \leq 0.03$ do not fit the experimental data well. We estimate that the fraction x of "resistant" cell population should be between 0.04 and 0.1. However, the result of equation (3.3.9) fits well over the entire dose range. The "linear" property of the survival curve is the total effect of "radio-resistant" cells (which have a smaller γ value compared to that of "regular" cells) and the "regular" cells expressed in equation (3.3.9). As noted above, even a small portion of "radio-resistant" cells can greatly influence the surviving fraction. We also apply equation (3.3.9) to Human HeLa cells in culture (using data from Fig. 3B in reference [40]) and DU145 cell line *in vitro* (using data from Fig. 4A in reference [40], though it was originally from reference [42]). The curves fit better than the LQ model and Astrahan's LQ-L model, especially for DU145 (relative to the dots if there are error bars). The results and corresponding parameters are shown in Figs. 3.3.9 and 3.3.10 respectively. All parameters are chosen to get the closest fitting curve.

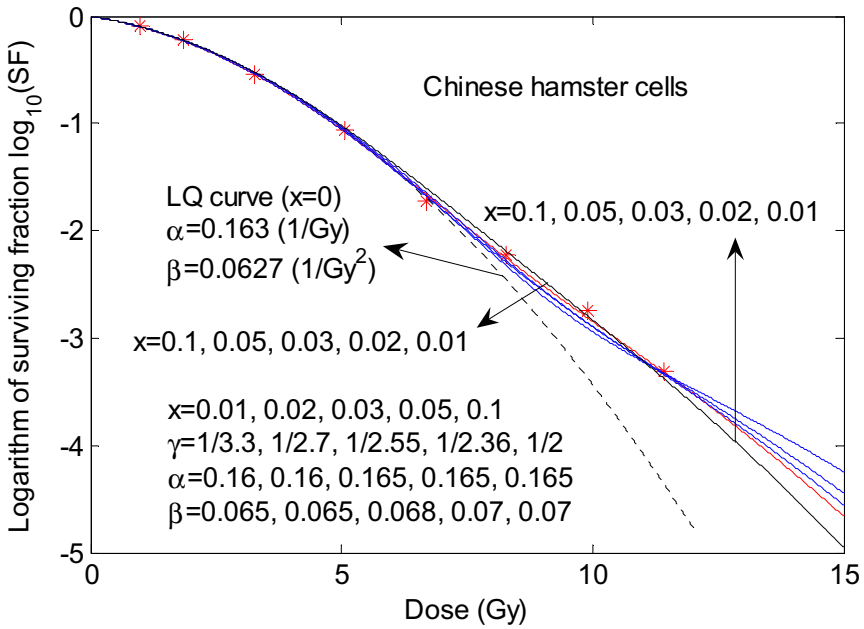

Fig. 3.3.8 Survival curves of Chinese hamster cells with different components of "radio-resistant" cells

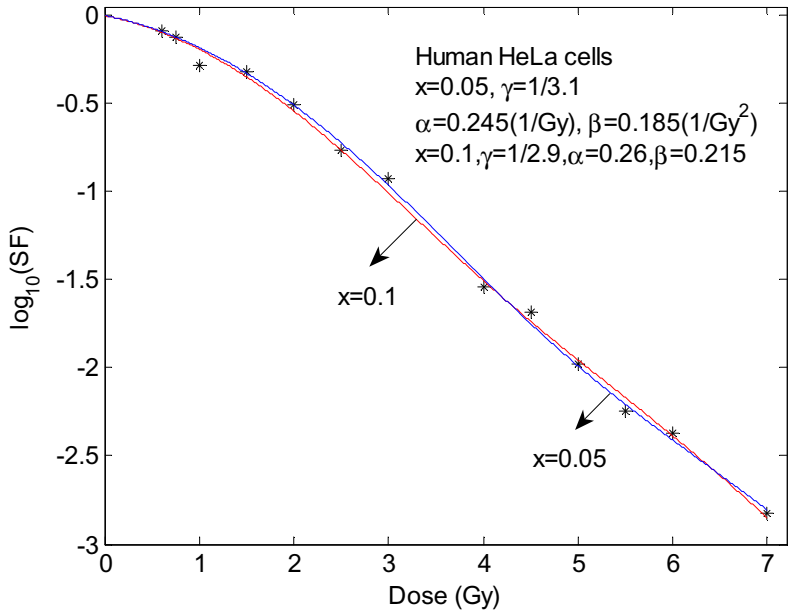

Fig. 3.3.9 Survival curve of Human HeLa cells in culture

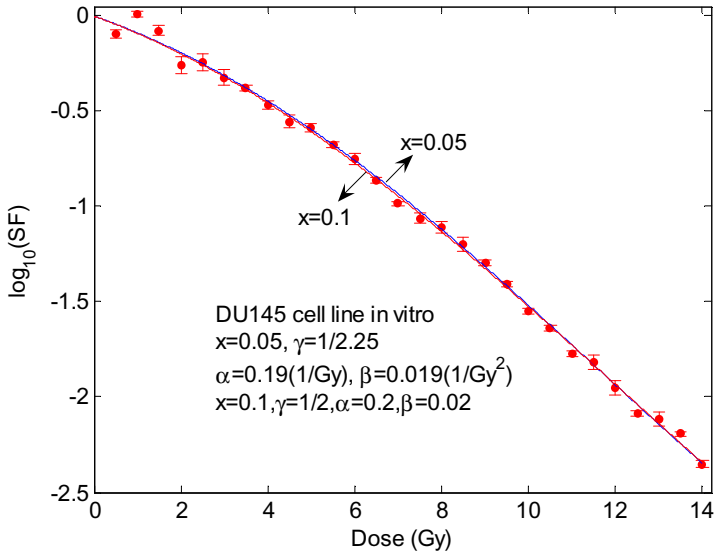

Fig. 3.3.10 Survival curve of DU145 cell line *in vitro*

Figs. 3.3.8 to 3.3.10 clearly show that some "radio-resistant" cells exist in culture and in vitro for both normal and cancer cells. Studies show that cancer stem cells are more resistant to radiation than other cancer cells [55, 56]. A similar argument can be made for any sub-population of cells that are radioresistant. Currently there is considerable debate over the importance of tumor stem cells to radiation response. If tumor stem cells are indeed resistant to the damaging effects of ionizing radiation, the discussion above regarding radioresistant cells may be similar to one concerning stem cells. As we mentioned above, different cell populations in one system can grow harmoniously before treatment and may not be identified. However, different cell populations respond differently to therapy and can be discovered.

For comparison, we display the curve fitting graph (Fig. 4-A in Ref. [40]), which is based on the LQ-L model for DU145 cell line in vitro, in Fig. 3.3.11. The blue (upper) dashed line is the best LQ-L fit and the red (lower) dashed line only constrains γ, which is approximately the slope of the line tangent to the LQ curve at dose D_T, where the curve becomes linear [40]. Obviously, the blue (upper) dashed line does not fit the survival curve well in the lower dose region (2.0-4.5 Gy) and the red (lower) dashed line does not fit the survival curve well in the middle dose region (8.0-9.5 Gy). Also, the LQ-L model

does not fit the survival curves well for Human HeLa cells in culture from 1.5-3.0 Gy and C3H 10T1/2 cells in culture from 4.5-8.0 Gy (see Fig. 3-B and D in reference [40]). Here we calculate the root-mean-square (RMS) differences based on the formula $RMS=\sqrt{\frac{1}{m}\sum_{i=1}^{m}(\log SF_i-\log SF_{fit})^2}$ [50]. We can also calculate $\chi^2=\sum_{i=1}^{m}\frac{(\log SF_i-\log SF_{fit})^2}{\sigma_i^2}$ if we know the variance of each experimental point, where σ_i represents the variance of $\log SF_i$. We do so since the increments of $\log SF$ are equally spaced and the differences of $\log SF_i$-$\log SF_{\text{fit}}$ are "more easily correlated to the goodness of fit that is visually apparent in the usual semi-log plot of SF vs. D [50]". The results are listed in table 3.3.3, and we can see that the present model fits better than the LQ-L model. We can see that the surviving fraction of the second point in the graph below for DU145 is 1.0215, which is most likely an impossible value. If we take this point out, the fit for the present model will be even better than it does now.

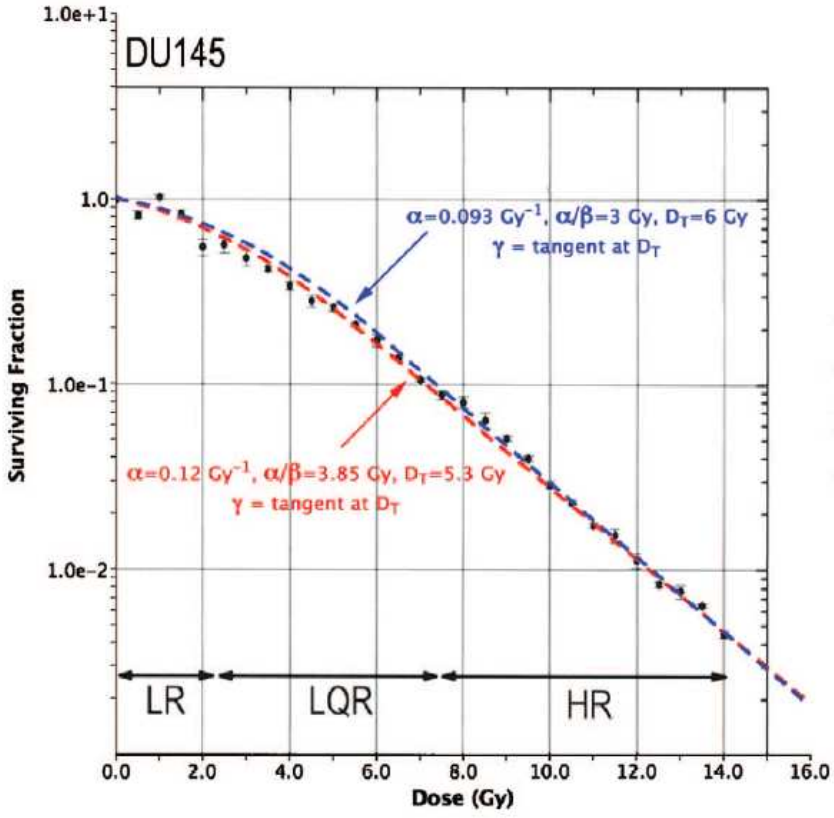

Fig. 3.3.11 Curve fitting based on the LQ-L model for DU145 cell line *in vitro* [40]

Table 3.3.3 The goodness of fit for different models (x=0.1)

	The present model (free fit)		The LQ-L Model		
	RMS	χ^2		RMS	χ^2
Human HeLa	0.04725			0.05651	
DU145	0.03580	90.26	Upper dashed blue line	0.05590	168.76
			Lower dashed red line	0.04536	113.37

We also applied eq. (3.3.9) to fit the survival curve for C3H 10T1/2. The data is digitized from Ref. [40] and the result is shown in Fig. 3.3.12. Similarly, we extracted the experimental data for CP3 (a human prostate carcinoma cell line) and U-373MG (a human glioblastoma cell line) from Fig. 1 (a) and (b) in reference [42], and applied equation (3.3.9) to fit the survival curves. The results are shown in Figs. 3.3.13 and 3.3.14. Since the errors of these three survival curves are relatively large, we only give graphs with the case of x=0.1. Generally, the survival curves fit these experimental data quite well. Garcia et al. [42] analysed these data in different dose regions and noticed that the dependence of the fitted α and β on the dose range has an impact on the α/β ratio, which is determined from the survival data. Here we found the cause and a method for solving it.

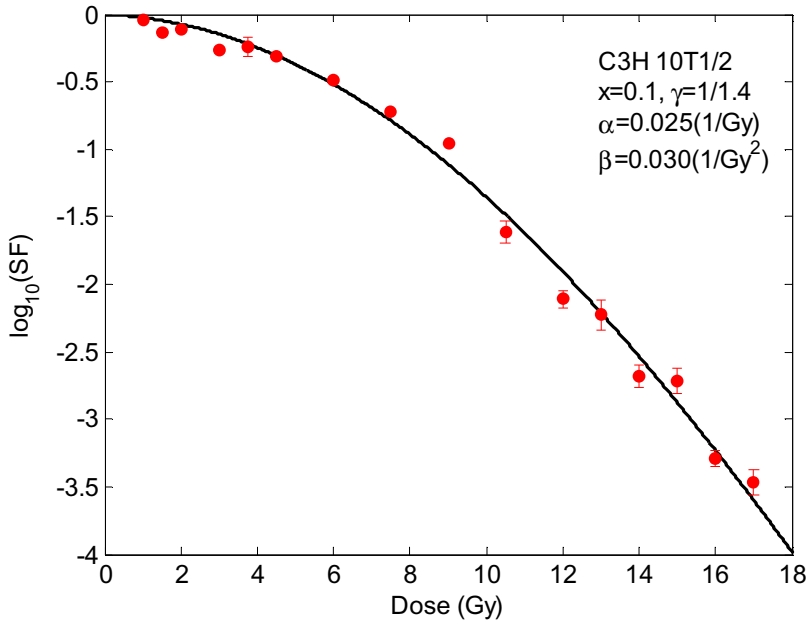

Fig. 3.3.12 Survival curve for mouse C3H 10T1/2 cells in culture

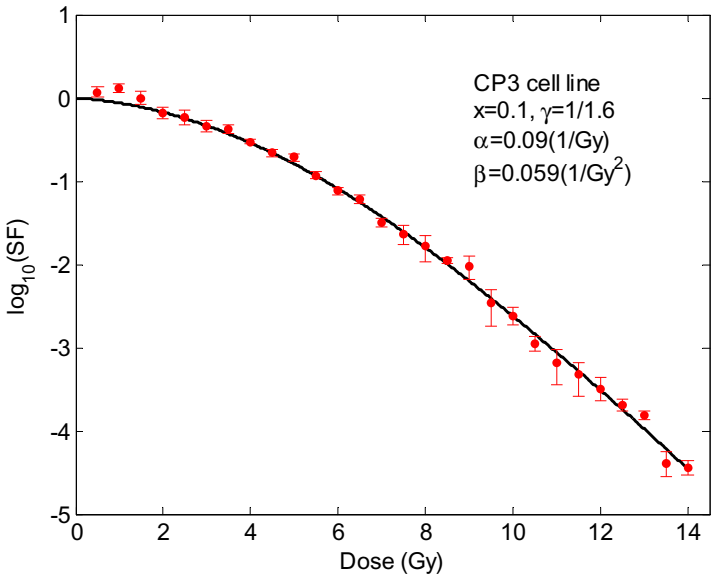

Fig. 3.3.13 Survival curve for CP3 human prostate carcinoma cell line

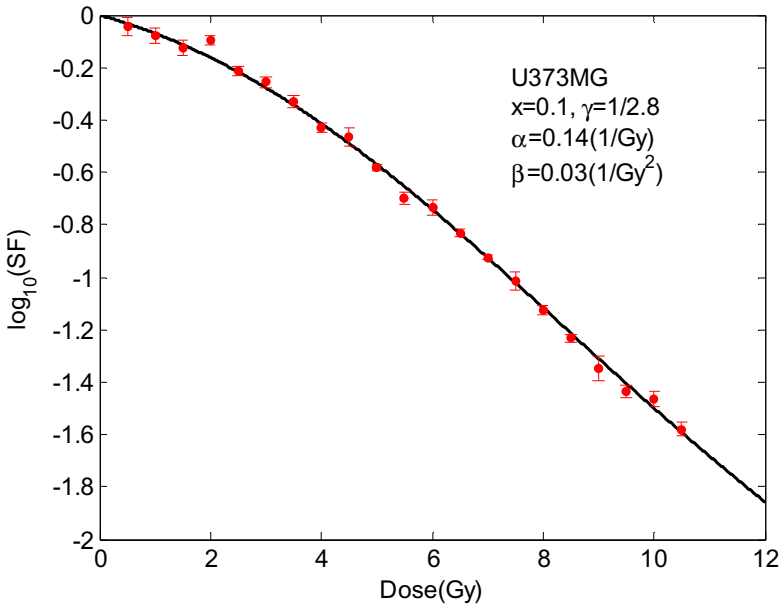

Fig. 3.3.14 Survival curve for U373MG human glioblastoma cell line

All curve fittings show that there are some "resistant" cells in both tumor and normal cells. Let us apply eq. (3.3.9) to fit the survival curves for EMT-6/Ro tumors under aerobic and anoxic conditions in order to verify the existence of "resistant" cells. The

data are digitized from Fig. 3 in reference [49]. The results are shown in Fig. 3.3.15. This graph shows that there are some "resistant" cells in the cases under aerobic conditions. Obviously, the survival curves under aerobic conditions do not satisfy the LQL nor LPL models, though the surviving friction of a tumor under anoxic condition can approximately be fitted by the LQ model.

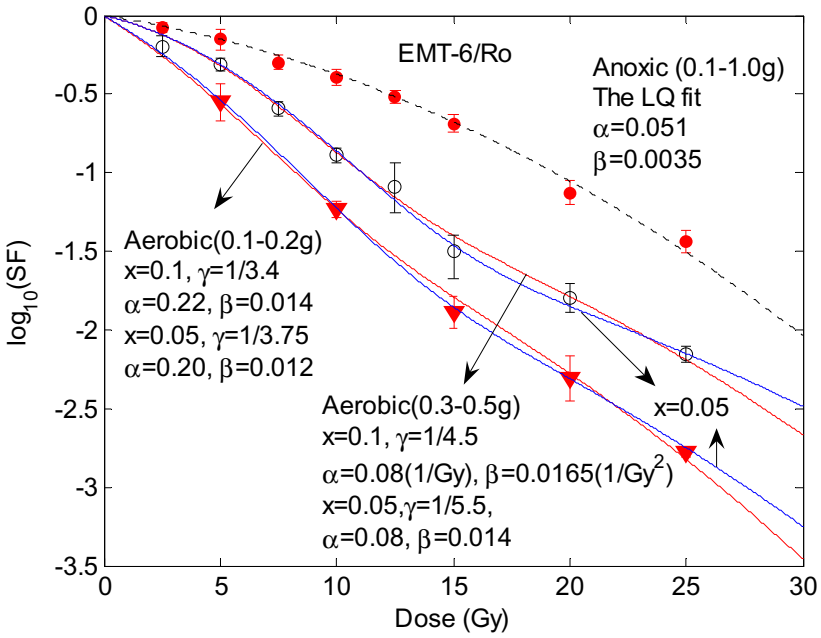

Fig. 3.3.15 Survival curves for EMT-6/Ro tumors under aerobic or anoxic conditions

Eqs. (3.3.8) and (3.3.9) are the results of $K >> \bar{S}$ and $K >> E$. These two conditions may be satisfied in most cases. However, there may be some cases where they may not be satisfied in the low dose region or in early growth stage, where M_0 is small. Therefore, we have to solve eq. (3.3.6) numerically for $K=\kappa D+\nu$. Powers and Tolmach [10, 54] reported the survival response of 6C3HED mouse lymphosarcoma cells to radiation in vivo. They plotted several sets of experimental data on a graph and fitted the curve by eye. It is impossible to fit the data when we try other models such as the LQ, LQL or multi-component LQ model. However, when we apply eq. (3.3.6) to this case, it fits well. The results are shown in Fig. 3.3.16. The points are digitalized from reference [54]. Here

we did not use various symbols to identify the data for different experiments. The responses of the same cells to a specific radiation are similar, though the data are taken from different experiments.

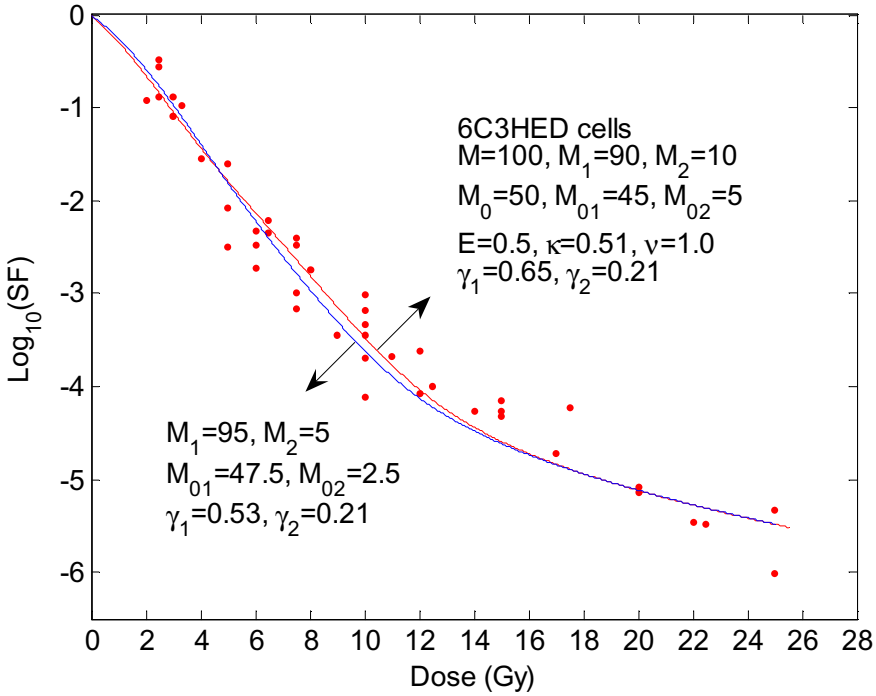

Fig. 3.3.16 Survival of 6C3HED mouse lymphosarcoma cells irradiated in vivo. The dots represent experimental data that are digitalized from Fig. 1 in reference [54].

Since an organism has various production rates at different growth stages, cell response to therapy should differ in each stage. The present model reflects this effect. However, the LQ, as well as other models, cannot. We take the two most radio-resistant cases, EMT-6 mouse tumor and MO16 human glioblastoma, which were thought to be incompatible with the LQ models [40], as an example and use eq. (3.3.6) to fit the experimental data. The results are shown in Fig. 3.3.17. The survival curves are different for various M_0. In these two cases, the change of ν (and correspondingly α) is not sensitive enough to affect the survival curves since κ (and correspondingly β) is relatively large, which places $\kappa D >> \nu$ in the experimental dose region. This might be a common property for radioresistant cases. In Fig. 3.3.17, we use the parameters for one kind of cell population to fit the survival curves. It means that the difference between

"regular" and "resistant" cells is small. In this case, the "radiation shoulder" will be wide. The two most radio-resistant cases in Fig. 3.3.17 might have this condition.

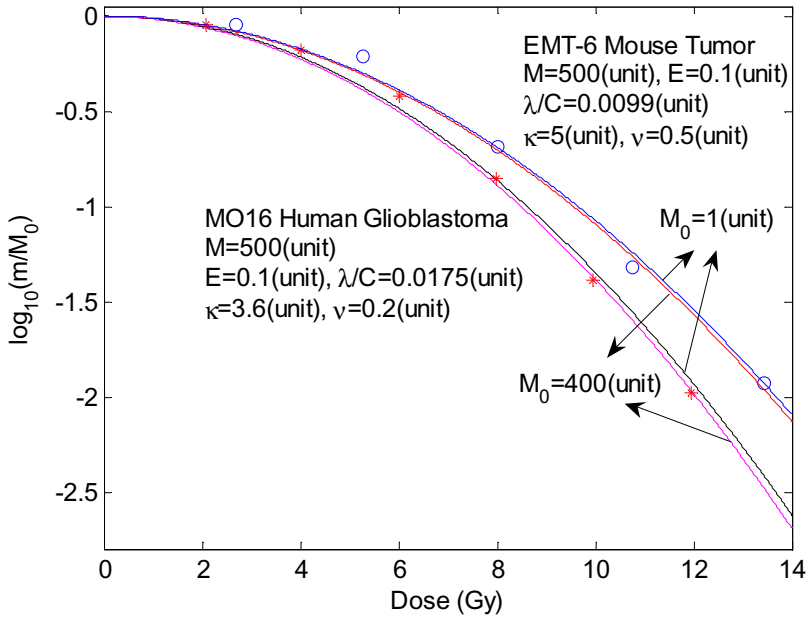

Fig.3.3.17 Curvature of surviving fraction vs. radiation dose for radio-resistant cases

Eq. (3.3.9) is a single-valued function and can be used to determine the fraction x of cell population and the response coefficient γ for a certain system (α and β are known for a particular radiation or chemotherapy). However, in the present situation, the x and γ are unknown, so we have to use this equation to fit the survival curve. When both α and β are small and in the low or even middle dose region, we have:

$$SF \approx \exp[-(\alpha+\beta D)D]+x(1-\gamma)(\alpha+\beta D)D+\cdots$$

When we choose x and γ, it may cause $x(1-\gamma)$=constant, which means that many sets of x and γ correspond to the same surviving fraction.

Garcia et al. [42] noticed that the LQ model only fits the survival curves in the middle dose region. In the low dose region, it cannot even explain the mechanism for cell survival. Many experimental data show that surviving fractions in the low dose region fluctuate. Some of them are even greater than 100%. This can be explained based on the present model. When the dose is low, the additional death rate is small. The total death

rate approximately balances the production rate so that if one weighs a bit more, it may cause opposite results. If the environment or conditions for cell population are slightly different and the cell growth is slightly uneven, the response to radiation is entirely different. In some cases, the production rate may even be greater than the total death rate, causing the system to grow and the surviving fraction to become greater than 1, as shown in Fig. 3.3.18 schematically.

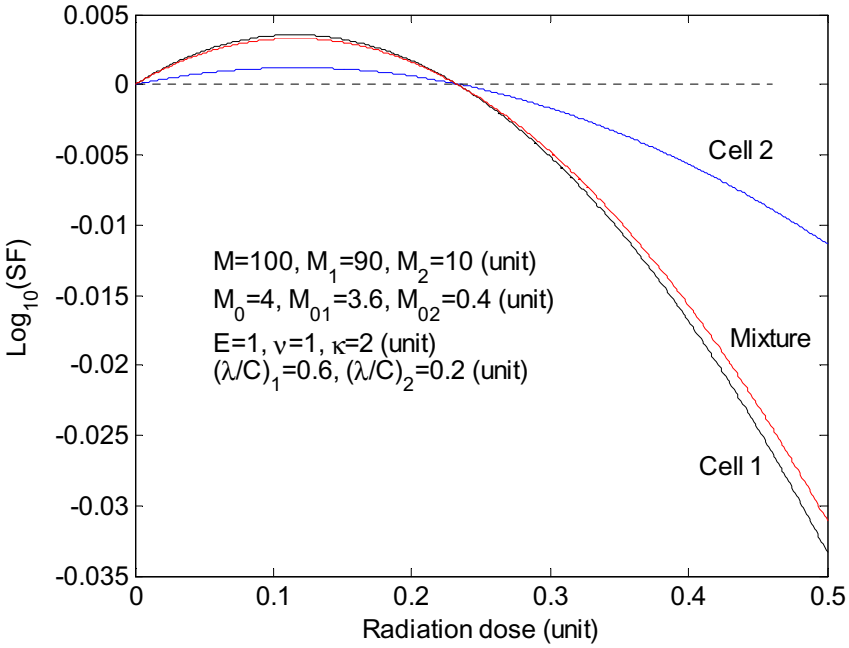

Fig.3.3.18 Schematic of survival response in the low dose region where $K+E< S$

If the LET is large enough to kill all localized cells equally, the additional death rates are proportional to the amount of cells present and have a relationship of $\nu_{res}/C_{res}=\nu_{reg}/C_{reg}=\theta$ for different kinds of cells. For cells in the same tissue or from the same source which grow harmoniously before therapy, condition $E_{res}/C_{res}=E_{reg}/C_{reg}=\beta^{\circ}$ should be satisfied. Also, $M_{res}=xM$ and $M_{0res}=xM_0$. Thus we have,

$$SF=\frac{m_{res}+m_{reg}}{M_0}=\frac{M}{M_0(\theta+\beta^{\circ})^4}\{\beta^{\circ}-[\beta^{\circ}-(\theta+\beta^{\circ})(\frac{M_0}{M})^{1/4}]\exp[-(\theta+\beta^{\circ})\lambda D/4]\}^4 \quad (3.3.10)$$

In this case, the consequence is the same as eq. (3.3.5′) for single cell component system. When the total death rates are much greater than the production rates for both cell populations, we have:

$$SF = \exp[-(\theta + \beta^{\circ})\lambda D] \qquad (3.3.10')$$

Eq. (3.3.10′) shows a linear relation of $\log(SF)\sim D$. For cells that do not grow harmoniously before therapy, we have to use eq. (3.3.5′) for calculating the masses separately and then obtain the total surviving fraction of cells $SF=(m_{res}+m_{reg})/M_0$. Since M, M_0 and β° are not related for different cell populations, the situation is complicated. If LET is not large enough, $\nu_{res}/C_{res}\neq\nu_{reg}/C_{reg}$ since the number of reparable cells for one or even both subpopulations cannot be ignored. In this case, eq. (3.3.10) may not be satisfied.

3.3.3 Chemotherapy

Cell survival responses to chemotherapy are complicated. Different kinds of chemotherapeutic agents show varied cell killing patterns [17-21]. For tumor cells in an organism, the effects of chemotherapeutic agents depend upon absorption (the process of a drug entering blood circulation), distribution (the dispersion or dissemination of a drug throughout the fluid and tissues of the body), metabolism, and excretion [35]. For cell survival experiment in vitro, there are usually two cases: 1) cells are in the growing media with various drug concentrations for the same length of time; and 2) cells are in the growing media with the same drug concentration for different lengths of time. The metabolism and excretion can be ignored and drug concentration changes little during the experimental period. Analogous to radiation, chemotherapy also causes DNA damage. The difference is that radiation can bring the dose (energy) into a cell directly, whereas chemotherapy may accumulate the dose through diffusion and osmosis. Dose absorption

for radiation is time related. Considering the drug delivery process, absorption of chemotherapeutic agents is also time dependent and causes DNA damage in cells. Therefore, the additional death rate K should relate to the absorbed dose, which is defined as the product of drug concentration and the amount of time the cells are immersed, which is shown by the equation $D=n\cdot t$ [17, 20]. We assume that the additional death rate has a linear relation to the absorbed dose: $K=\kappa D+\nu=\kappa n t+\nu$. Here, ν should be related to drug concentration. For a fixed concentration, ν is constant. Term ν is from single event killing, and term $\kappa n t$ derives from double event killing. When the concentration is fixed, the dose is proportional to time. Therefore, eq. (3.3.3) becomes

$$\frac{dm}{dt}=\frac{m}{C}\left[E\left(\frac{M}{m}\right)^{1/4}-E-\kappa n t-\nu\right] \tag{3.3.11}$$

Usually, eq. (3.3.11) only has a numerical solution and can be expressed as a confluent hypergeometric function (see appendix 2).

$$m=\left(\frac{EM^{1/4}}{4C}\right)^4\exp[-\frac{\kappa n}{2C}(t+\frac{E+\nu}{\kappa n})^2]\{a_0+(t+\frac{E+\nu}{\kappa n})M[\frac{1}{2},\frac{3}{2},\frac{\kappa n}{8C}(t+\frac{E+\nu}{\kappa n})^2]\}^4 \tag{3.3.12}$$

where $a_0=\frac{4C}{E}\left(\frac{M_0}{M}\right)^{1/4}\exp[\frac{(E+\nu)^2}{8C\kappa n}]-\frac{E+\nu}{\kappa n}M[\frac{1}{2},\frac{3}{2},\frac{(E+\nu)^2}{8C\kappa n}]$

In the case of fixed time, we can find the relationship between the mass/number of cells and the concentration of chemotherapeutic agent. Note that $\nu=\nu(n)$.

When $\kappa n=0$ (this may occur since some drugs only cause single event killing), eq. (3.3.11) has a complete analytic solution:

$$E-(E+\nu)\left(\frac{m}{M}\right)^{1/4}=[E-(E+\nu)\left(\frac{M_0}{M}\right)^{1/4}]\exp(-\frac{E+\nu}{4C}t) \tag{3.3.13}$$

or
$$m=\frac{M}{(E+\nu)^4}\{E-[E-(E+\nu)(\frac{M_0}{M})^{1/4}]\exp(-\frac{E+\nu}{4C}t)\}^4 \tag{3.3.13′}$$

In the case of fixed drug concentration, ν should be a constant. The effect of treatment depends on ν and M_0 (the mass or number of cells when a treatment starts). Fig. 3.3.19

shows that the result is opposite if M_0 is different, even if all other parameters are the same.

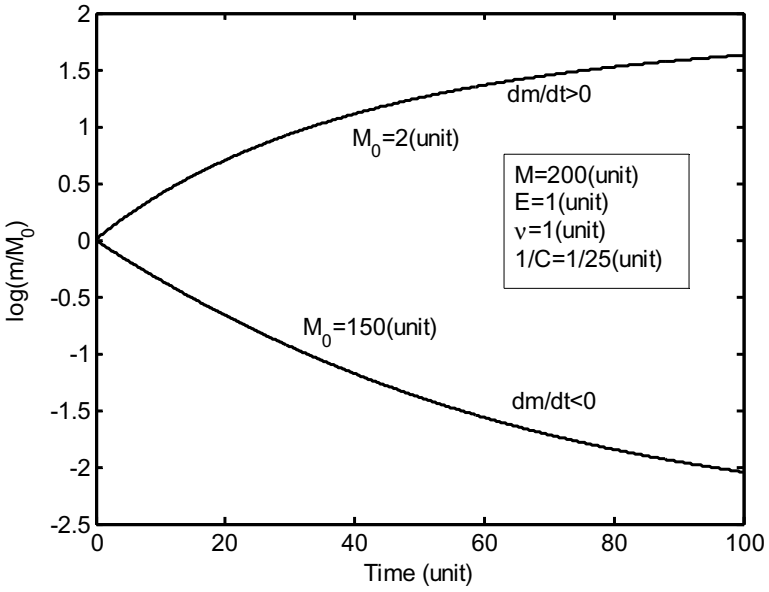

Fig. 3.3.19 Survival curve of tumor cells with different initial masses (M_0)

When condition $E+\kappa nt+\nu >> E(M/m)^{0.25}$ is satisfied, eq. (3.3.11) is reduced to

$$\frac{dm}{dt} = -\frac{m}{C}(E + \kappa nt + \nu) \tag{3.3.11′}$$

The solution of eq. (3.3.11′) is

$$m = \exp[-\frac{(E+\nu)t}{C} - \frac{\kappa nt^2}{2C}] \tag{3.3.14}$$

When the amount of time for cell treatment in the drug medium is fixed, the mass or number of cells that survived is a function of drug concentration.

1) Assume $\nu(n)=\delta n$, where δ is a constant

In this case, eq. (3.3.14) gives $m = M_0 \exp(-\alpha n - \chi)$. Term χ is from the natural death rate, which is small. It might be balanced by the production rate in some cases. When we

did curve fitting for cell response to radiation, we found that there are always some "resistant" cells. If this is true, then resistant cells should also exist and respond differently to chemotherapy, though they may not be as "resistant" to some agents (e.g. response of EMT6 cells to Mitomycin-C is more "resistant" under aerated condition than hypoxic [10]). Similarly, we assume that there is x fraction of "resistant" cells. The surviving fraction is

$$SF = (1-x)\exp(-\alpha n - \chi) + x\exp[-\gamma(\alpha n + \chi)] \tag{3.3.15}$$

2) Assume $\nu(n)=\delta n^2$

In this case, eq. (5.14) gives $m = M_0 \exp(-\alpha n - \beta n^2 - \chi)$. If there is x fraction of "resistant" cells, the surviving fraction is

$$SF = (1-x)\exp(-\alpha n - \beta n^2 - \chi) + x\exp[-\gamma(\alpha n + \beta n^2 + \chi)] \tag{3.3.16}$$

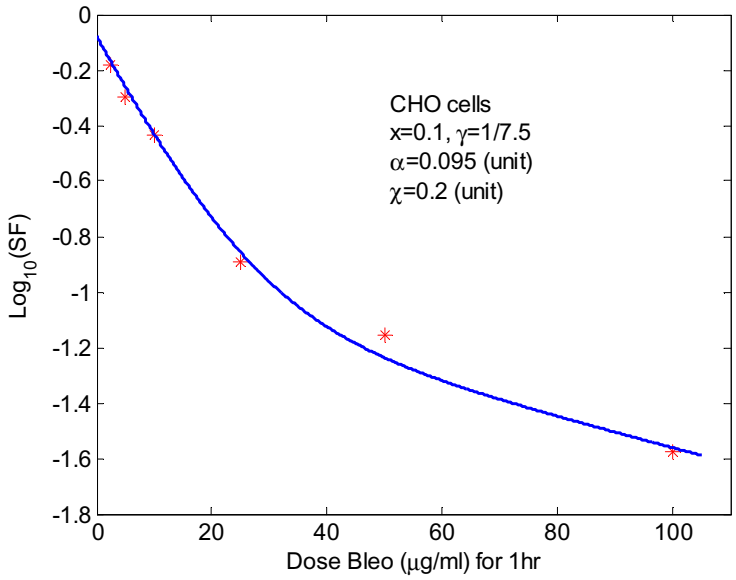

Fig. 3.3.20 Survival curve of CHO cells treated by BLM (Bleo) in the plateau phase

When we use eq. (3.3.11), (3.3.15) or (3.3.16) to fit the survival curves for chemotherapy, there is no way to fit the curves if we assume that only one kind of cell exists. However,

the curves fit well if we assume that there are two different kinds of cells which coexist in the system. We apply eq. (3.3.15) to fit the survival curve for Chinese hamster ovary (CHO) cells treated by BLM (bleomycin) [57]. The result is shown in Fig. 3.3.20. The experimental data are from Chart 2 of reference [57], which gives the effect of BLM on survival of CHO cells treated in the plateau phase. In this case, the value of χ might be from the natural death rate E. We also apply eq. (3.3.15) to fit the survival curve for V79 hamster cells treated with graded doses of BLM for 4 hrs at 37.5°C [58]. The result is shown in Fig. 3.3.21, and the coordinates are digitalized from Fig. 2 of reference [58] under hypoxic condition.

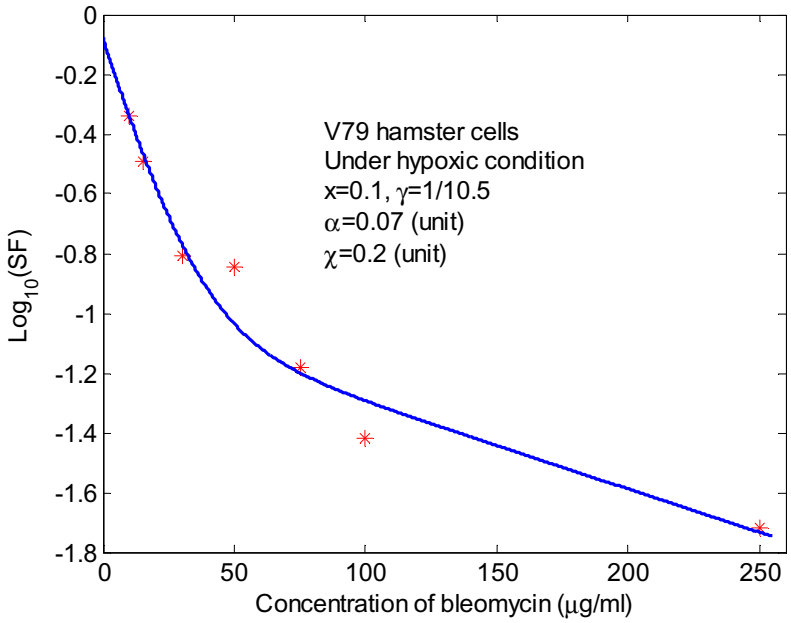

Fig. 3.3.21 Survival curves for V79 hamster cells treated with graded doses of BLM for 4 hrs

We also apply eq. (3.3.15) to fit the survival curves of human melanoma SK-MEL28 cells after Cisplatin (CDDP) treatment and electrochemotherapy (ECT) with CDDP. The experimental data are digitalized from reference [63], and the results are shown in Fig. 3.3.22.

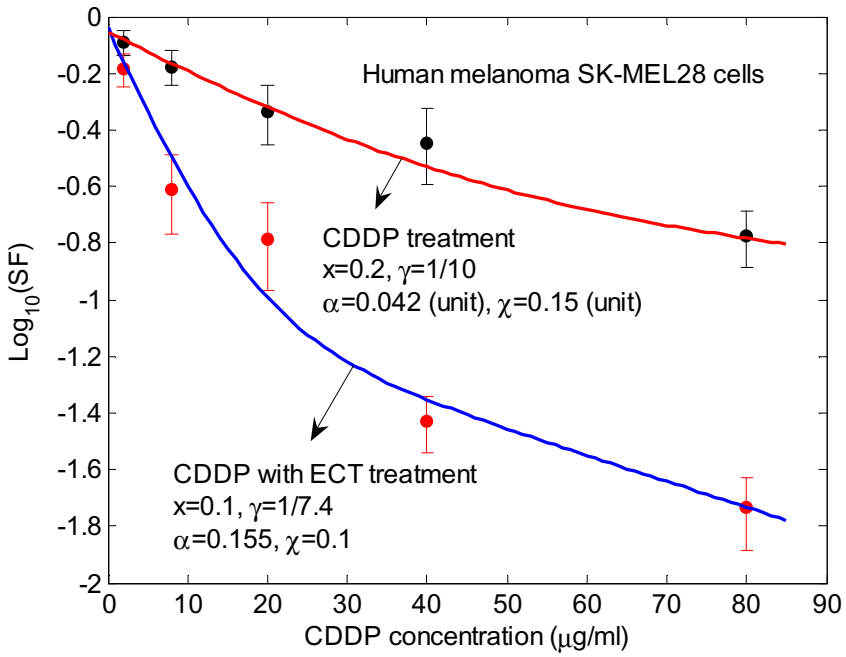

Fig. 3.3.22 Surviving fractions of SK-MEL28 cells after CDDP treatment and ECT with CDDP

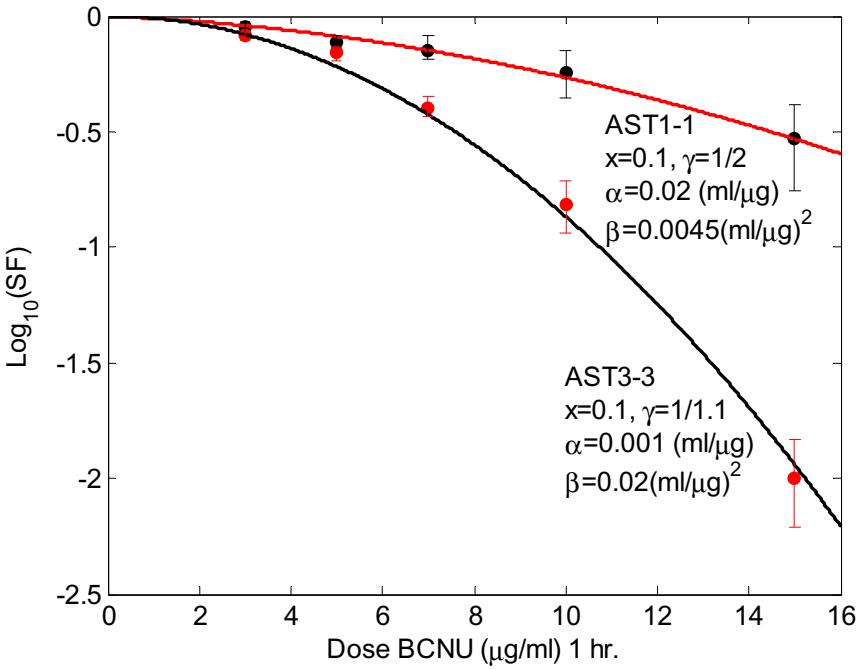

Fig. 3.3.23 Survival responses of human astrocytoma clones to BCNU

Some chemotherapeutic agents such as BCNU and PCNU [60] cause cell survival response to be similar to that under radiation. We apply eq. (3.3.16) to fit the survival responses of human astrocytoma clones to BCNU and PCNU [60]. The experimental data are digitalized from Figs. 1 and 3 in reference [60]. The results are shown in Figs. 3.3.23 and 3.3.24, from which we can see that 10% of "resistant" cells exist. When clone AST3-3 is treated by BCNU, the difference of λ/C between "regular" and "resistant" cells is small; yet when it is treated by PCNU, the difference is large. We set χ=0 in both Figs. 3.3.23 and 3.3.24.

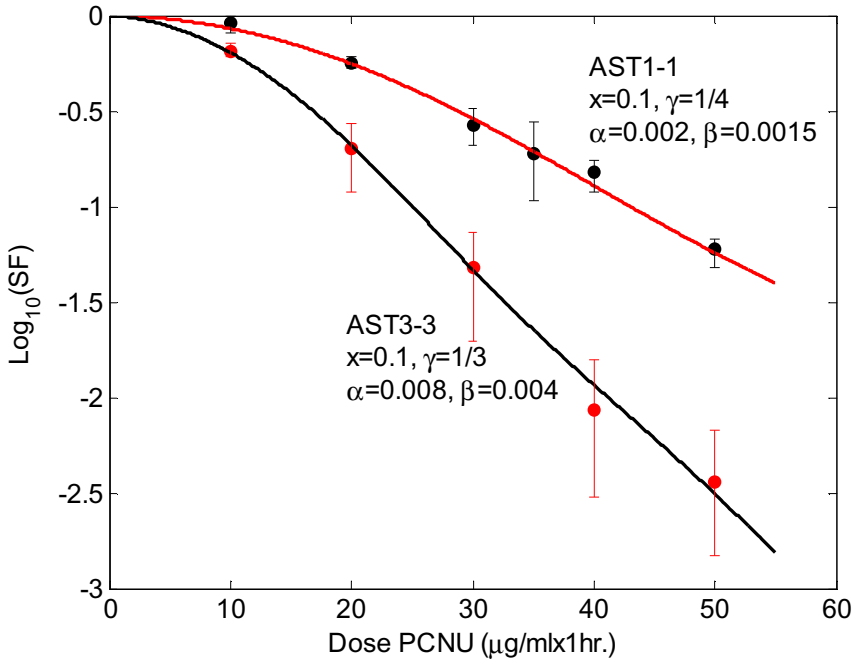

Fig. 3.3.24 Survival responses of human astrocytoma clones to PCNU

However, we have to use eq. (3.3.11) for the survival response of V79-182 Chinese hamster cells to Adriamycin (ADRM) [10, 61]. In this case, the concentration of chemotherapeutic agent is fixed, which makes ν a constant. Belli and Piro [61] gave a surviving fraction vs. time graph for V79 under a constant concentration of Adriamycin agent. Here we use eq. (3.3.11) to fit the experimental data of Chart 2 in reference [61]. The result is shown in Fig. 3.3.25.

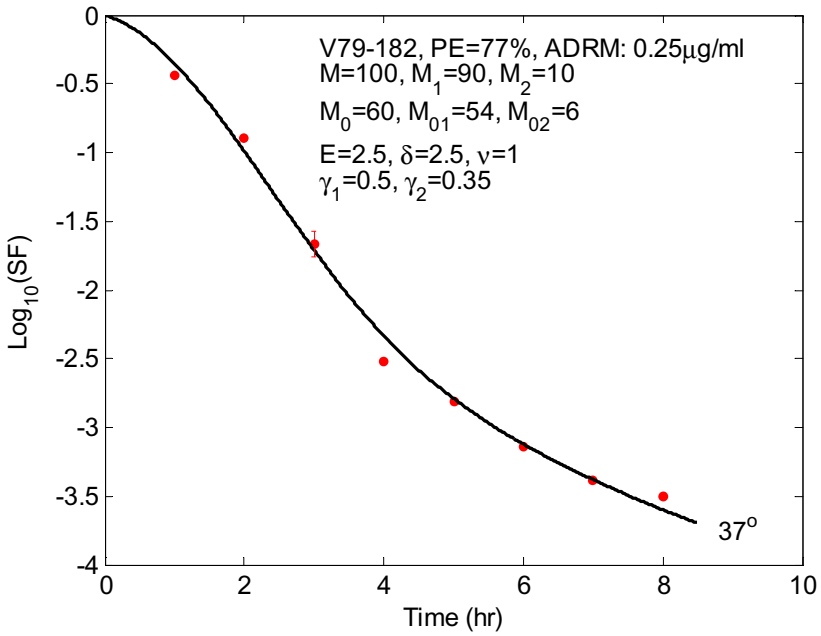

Fig. 3.3.25 Survival response of V79 cells to ADRM

Conventional chemotherapy works mainly by killing tumor cells that actively proliferate, whereas metronomic chemotherapy works through reducing nutritional supply. Consequently, conventional chemotherapy directly causes an additional death rate $\overline{K}$, whereas metronomic chemotherapy decreases the production rate $\overline{S}$. The average production rate is determined by the biological death rate, the current mass and the asymptotic mass of the tumor. As we have discussed above, the asymptotic mass correlates to the nutrition supply [33, 34]. It means that we can control the production rate by restricting the source of nutrition supply (including oxygen). Therapies that target the supplying vasculature, and thus starving the tumor, are trying to solve the problem from the source. In fact, a solid tumor is spatially heterogeneous. The outer region has many exchange vessels. There is plenty of nutrition supplied to the tumor; therefore, it has rapidly dividing cells in this region.

From eq. (3.3.3) or (3.3.11), we know that tumor mass (or surviving fraction) decreases exponentially when additional death rate is much greater than the production rate, which is shown as $\overline{K} >> \overline{S}$. This condition may need a very strong dose of therapy in order to

kill tumor cells. The problem is that a strong dose also kills many normal cells. It causes permanent negative effects on the human body. Additionally, if we only care about the additional death rate and ignore the production rate, it may cause the so-called "objective tumor response". It will benefit patients the most if we can control the production rate and use a therapy that kills cells in a balanced way. According to equation (3.3.3), the growth rate is less than zero ($dm/dt<0$) when the production rate is smaller than the death rate ($E\left(\frac{M}{m}\right)^{1/4} < E + \overline{K}$). It means that the tumor mass decreases, which shows us that we should also control the production rate of tumor cells. Antiangiogenic therapy, such as metronomic chemotherapy (involving minimally toxic doses on a frequent or continuous schedule), is used to decrease the production rate of tumor cells by affecting the endothelium of growing tumor vasculature and stimulating the anticancer immune response [130, 131]. In fact, based on eq. (3.3.3), when we apply metronomic chemotherapy or antiangiogenic therapy to control the production rate of a tumor, which gives $E\left(\frac{M}{m}\right)^{1/4} - E \approx 0$, and therefore $\frac{dm}{dt} \approx -\frac{m}{C}K$. It means that a small additional death rate (correspondingly, a small amount of damage to the human body) can cause the mass of a tumor to decrease exponentially. This is much better for decreasing the mass of a tumor than applying a therapy that causes a large additional death rate K (therefore a large amount of damage to human body). If the condition $E\left(\frac{M}{m}\right)^{1/4} - E < 0$ is satisfied by applying metronomic or antiangiogenic therapy to control the production rate of tumor cells, the mass of a tumor will decrease naturally. For antiangiogenic therapy, the additional death rate can be taken as $K \approx \nu$ since the dose is small. Also, the constant ν is small because antiangiogenic agents have a much lower toxicity. The main purpose of antiangiogenic therapy is to decrease the production rate by controlling the nutrition and oxygen supply. $M=M(t)$ is expected to become a decreasing function once the therapy has been applied.

The production rate $\overline{S}$ is much greater than the death rate at the early stage; therefore, the model suggests that use of metronomic chemotherapy is warranted if surgery cannot

be applied. At the late stage, the production rate of a tumor is small; therefore, the model suggests the use of a therapy that kills tumor cells. Then, antiangiogenic therapy should be used again to ensure that there will be no growth of new tumor capillaries. In fact, the inequation above is very important. Inability to satisfy it implies that the tumor growth process is not really controlled.

In the central area, many tumor cells may be "dormant" due to nutrition shortage. In this area, $\overline{S} \approx E$. The problem with using chemotherapy on these tumor cells is that the delivery of a chemotherapeutic drug is as difficult as the delivery of nutrition to this region. Thus, chemotherapy may not cure a tumor but rather control its growth, despite the fact that more than 90% of tumor cells respond to this treatment. The practice of combining chemotherapy with other therapies, such as surgery or radiation, is supported by this model.

Different stages of tumor growth have distinct production rates. Therefore, treatment strategies should be dissimilar at various tumor stages. Fig. 3.3.19 shows how the results of chemotherapy could be opposite, even if all other parameters are the same. The sole exception is the initial mass, according to eq. (3.3.13). If a tumor is at an early growth stage, the model suggests the required dose is higher than expected since a large ν is needed to control its growth.

Up till now, we have discussed the processes of tumor growth and cell response to therapies (e.g. radio- and chemotherapy). However, the effects of therapies differ depending on the situation. For instance, what are the dose and strategy that can benefit the individual the most? Usually, tumor treatments need a combination of therapies (e.g. surgery with radiation and/or chemotherapy). How to combine therapies for the most effective treatment? If we can get feedback regarding the results of clinical therapy in time, a proper and suitable strategy for treatment may be determined efficiently, which is necessary for saving the life of a cancer patient. Studies show that TIFP is a physiological parameter that has been shown to correlate inversely with tumor responsiveness to treatment. It is also an early marker of tumor response to radiotherapy and chemotherapy. The effects of treatments can be reflected by TIFP. Also, reduced TIFP allows increased delivery and treatment efficacy of drugs. Despite the importance of TIFP, its

measurement is, at present, limited to invasive point measurements. This kind of invasive measurement limits its clinical application. Therefore, studying the properties of TIFP and understanding its formation and distribution mechanisms are helpful in actualizing TIFP noninvasive measurement, which has the potential for clinical application.

Generally, the mechanism for TIFP distribution is the formation of a pressure barrier in the well-vascularised region, created by the tumor-associated vasculature. Before the conditions for steady state are satisfied, the pressure in the central area is less than the pressure in the pressure barrier. The exact value depends on the state of the central region. At steady state, the pressure is uniform in the entire central area, while pressure in the periphery is dependent on the environmental conditions. The fluid flux follows Darcy's law (an equation for fluid flowing within a porous medium) and the pressure is constrained by the continuity conditions. Based on this idea, once the conditions in the central, well vascularised and peripheral regions are known, the pressure distribution is set. We find that it is possible to detect TIFP noninvasively. Not only can noninvasive measurement be applied to measure the TIFP of a place where an invasive measurement cannot reach, but it can also be applied to monitor the development process and response to a specific treatment.

Imaging technologies such as MRI and US are the primary means of detecting tumor, and may be promising tools for actualizing TIFP noninvasive measurement. Based on this purpose, we will concentrate on TIFP formation and distribution, as well as its possible noninvasive measurement in the next chapter. Also, the principles of MRI application in medicine will be introduced. As an example, we will demonstrate the consequences of high TIFP on contrast agent kinetics in a rat's 9L cerebral glioma, which is acquired using a seven-Tesla MRI.

Chapter 4. TIFP Distribution and Its Noninvasive Measurement

Tumor interstitial fluid pressure (TIFP) is an important marker of tumor response to treatment. If we can determine its distribution by estimating some tumor parameters, we may actualize the noninvasive measurement of TIFP and effectively develop the best treatment strategy. Based on this purpose, we propose a simple but practical model to explore the relationship between TIFP and fluid flow, and derive the distribution of TIFP in different regions. It relates to the structure of a tumor, the source of interstitial fluid, as well as the path and method for fluid transport.

Since the denseness of vascular networks in the central region is completely different from that in the peripheral area, the activity of cells may be different. For simplicity's sake, we model a tumor as a spherical structure. Later, we will explain why it is not necessarily limited to a spherical case. Tumor cells proliferate and grow actively only if they are close to a supply of nutrients and oxygen from the stroma [9, 10]. For avascular tumors, the nutrition and oxygen supply comes from diffusion. When a tumor grows larger, the necrotic center also enlarges since the efficient nutrient and oxygen supply is limited within a certain distance (about 70 μm). For a vascularised tumor, most vessels are in the peripheral region. Therefore, the result is similar: the larger the tumor, the bigger the necrotic core. Considering the differences in vascular network distribution and cell activity in various regions, especially the change in TIFP, we divide a tumor into three regions: (1) the necrotic core ($r<r_n$) where most cells are dead; (2) the well perfused periphery ($r_n<r<R$), which is composed of some quiescent tumor cells, a few abnormal vessels, and a peripheral well-vascularized rim with active tumor cells; (3) the intermediary region ($r>R$). It is assumed that there are no functional lymphatics within the tumor, though some enlarged lymphatics exist near the periphery. In the necrotic core, there are some dead cells but almost no functional exchange vessels. The existence of so-

called super capillaries in tumors is inefficient at best in regard to nutritional delivery and waste removal. Therefore, there is no source or drain in the necrotic core region. In the blood vessel area, there is fluid source but not an effective drainage system. We assume that the drain exists near the edge of the tumor. Outside the tumor (in the normal tissue), there are drains because of the functional lymphatics in normal tissue. In the well vascularized area, blood vessels or capillaries are very abundant (much more so than that in the normal tissue). They form a chaotic vascular network, which may maintain a pressure distribution in the tumor. The schematic is shown in Fig. 4.1.

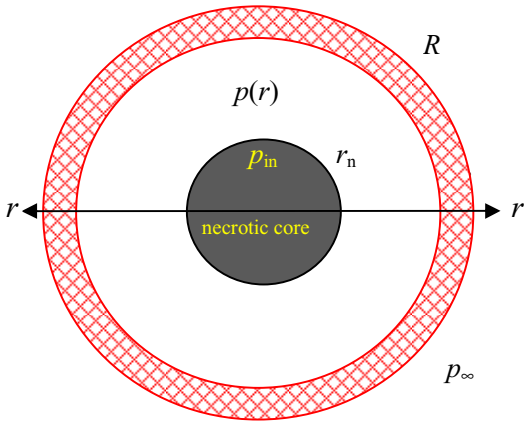

Fig. 4.1 Schematic of tumor structure

Usually, tumor tissues can be divided into three subcompartments: vascular, interstitial and cellular. The interstitial space is mainly composed of collagens and elastic fiber networks [132]. It can be divided into two compartments: the interstitial fluid and the structural molecules of the interstitial or the extracellular matrix [133]. The fluid that leaks out from blood vessels is inevitably met by resistance from the surroundings.

Let us now show how the pressure forms in detail. According to Starling's law, the net fluid flux J_s (m^3/s) across the wall of a blood vessel is expressed as [80, 83]:

$$J_s = LA[p_V - p - \sigma(\pi_V - \pi)] \tag{4.1}$$

where L (m^2s/kg) is the hydraulic conductivity of the blood vessel, A (m^2) the surface area of the blood vessel wall, p_V (mmHg) the vascular fluid pressure (the pressure in the

blood vessel), p (mmHg) the TIFP, σ the osmotic reflection coefficient, π_V (mmHg) the osmotic pressure of the plasma, and π the osmotic pressure of interstitial fluid. In a tumor, L and A are much greater than that in normal tissue. Equation (4.1) describes the source of TIFP. The detailed distribution of TIFP depends on the drain/sink and the conditions of outflow flux.

4.1 The IFP of Vascularized Spherical Shell

In our model, blood vessels are mainly distributed in the periphery region. There must be a fluid resistance or pressure barrier that makes the leaked fluid contribute to the elevated pressure in the central region. At first, let us imagine that the vascularized region is isolated. Suppose there is no necrotic core in the tumor's central area (meaning that there is only a vascularized spherical shell). If both inner and outer spherical surfaces of the vascularized region are closed and no fluid can flow out, then the IFP at steady state is $p_m=p_V-\sigma(\pi_V-\pi)$. When TIFP reaches this value, no fluid flows out from blood vessels. When there are openings on each spherical surface, the pressure from the two surfaces to the central area of the vascularized region will be modified. With increase in the width of openings, the pressure decreases, as shown in Fig. 4.2. Therefore, it forms a pressure barrier in the leaking (vascularized) region. In the maximum pressure region, the fluid remains still (velocity $u(r)=0$ because there is no pressure difference). The maximum pressure region becomes narrower when the openings become larger. Correspondingly, the flow rates on these two surfaces increase. Gradually, the maximum pressure region is narrowed down to a point when the openings widen to a critical value. If the openings continue to become wider, the highest pressure p_0 becomes smaller than p_m. The bigger the openings, the smaller the p_0. The maximum value of IFP at steady state is between 0 and p_m ($0<p_0\leq p_m$). Considering the fact that more functional blood vessels are distributed in the periphery region, we draw the highest pressure point closer to the tumor periphery. The exact value of p_0 depends on the conditions, such as the pressure p_v within blood

vessels, the lymphatic drainage ability, and fluid flow rate through the openings. The pressure at r_n depends on the pressure in the necrotic core p_{in}, and the pressure at R depends on the conditions of the environment. We will discuss them in detail later. Though p_0 is higher when there is more accumulated fluid, it is noteworthy that this pressure is not caused by gravity on the collected fluid. In fact, it is from the resistance caused by collagen and elastic fiber network, as well as their interactions. Though we focus on the case of a tumor with a necrotic core, the results may also be applied to the case of one with a non-necrotic core, where r_n=0.

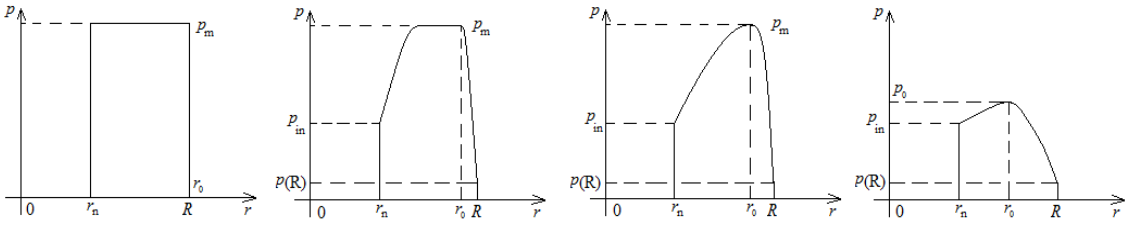

TIFP in vascularized region with closed boundary

TIFP in vascularized region with open boundary (opening increasing from left to right)

Fig. 4.2 Schematics of pressure modification for different boundary conditions in vascularized region

4.2 TIFP in the Central Area

In our model, there is a pressure barrier p_0 in the vascularized region, as shown in Fig. 4.2. In the beginning, the pressure in the necrotic core is smaller than p_0. The leaked fluid flows into this area. Since there is no lymphatic system (drain/sink), more and more fluid accumulate in this area. The pressure in this region gradually increases. It reaches p_0 once the fluid fills up this area, after which no more can flow into it. It maintains a constant pressure p_0. Then, all leaked fluid will flow outward. We assume that the radius

corresponding to the pressure barrier p_0 is r_0, and that fluid flows into the necrotic core with velocity u_{in} across the core radius r_n. Fig. 4.3 shows the schematic structure.

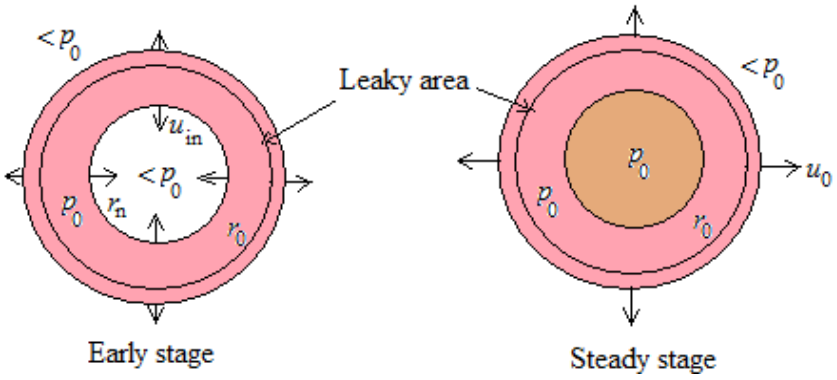

Fig. 4.3 Schematic of change in TIFP

We may take the vascularized region as a porous medium and use Darcy's law to describe fluid flow in this region since the cells are alive. However, we may not take the necrotic core as a porous medium since there are dead cells. Instead, we take it as a uniform homogeneity. If we ignore gravity, we have the relation

$$u(r) = -K\frac{dp(r)}{dr} \tag{4.2}$$

where K is the hydraulic conductivity of the interstitium. The pressure in the necrotic core should be the same as that on the surface $r = r_n$, where the fluid flows in. The more fluid accumulates in this region, the higher the pressure will become. Correspondingly, the pressure difference between $p_0(r_0)$ and $p(r_n)$ becomes lower and lower. Therefore, fluid velocity across the surface ($r = r_n$) of the necrotic core will be slower. When $p(r_n)=p_0$, the pressure difference is zero so no more fluid flows in. Then, the pressure within the region $r<r_0$ reaches p_0. In fact, at $r=r_0$, the pressure p_0 is at the maximum, so $dp/dr\big|_{r_0} = 0$, $u(r_0) = 0$. This is consistent with the view that we have discussed above. The increased pressure in the necrotic core ($r<r_n$) should be proportional to the amount of fluid inflow, so

$$p_{in}(t) - p_{in}(0) = \gamma 4\pi r_n^{\,2} \int_0^t u_{in}(t)dt \tag{4.3}$$

Here, γ is a proportionality coefficient. Its unit is mmHg/cm^3. Equation (4.3) can be rewritten as:

$$\frac{dp_{in}(t)}{dt} = \gamma 4\pi r_n^{\,2} u_{in}(t) \tag{4.3′}$$

In equation (4.2), K can be taken as a constant when r_0-r_n is small (blood vessels are distributed in a narrow spherical shell) and the pressure varies linearly with radius. Thus,

$$\bar{u} = \frac{u(r_0) + u(r_n)}{2} = \frac{u_{in}(t)}{2} = K\frac{p_0 - p_{in}(t)}{r_0 - r_n} \tag{4.4}$$

Combining equations (4.3′) and (4.4), we have

$$p_{in}(t) = p_0 - [p_0 - p_{in}(0)]e^{-\alpha t} \qquad (r < r_{in}) \tag{4.5}$$

where

$$\alpha = 8\pi\gamma K\frac{r_n^{\,2}}{r_0 - r_n}$$

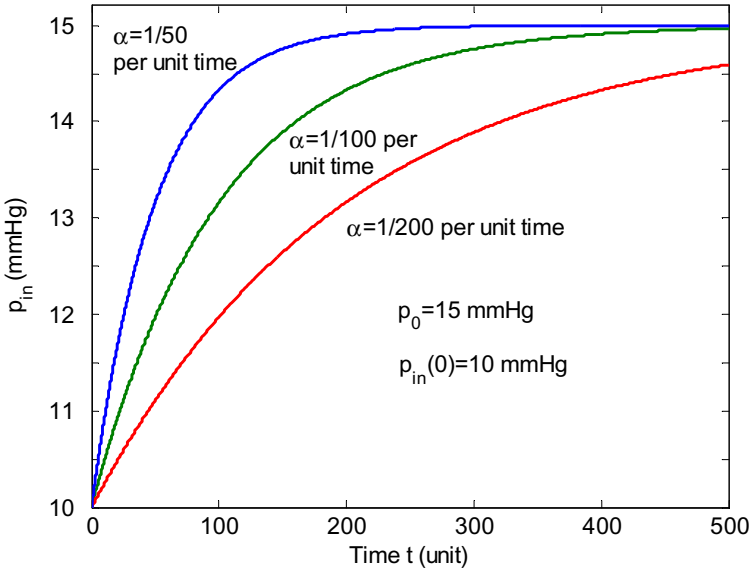

Fig. 4.4 TIFP of the necrotic core ($r \le r_n$) vs. time

Equation (4.5) shows that the IFP $p_{in}(t)$ in the necrotic core may be close to p_0 asymptotically. The actual situation depends on the initial pressure $p_{in}(0)$ of this region and the time constant α. The pressure reaches p_0 at steady state. This corresponds to the

experimental results, which are given in reference [81]. If we let p_0=15mmHg and $p_{in}(0)$=10mmHg, we can get the $p_{in}(t)$ graph for different values of α, as shown in Fig. 4.4. The graph includes the results given in reference [83]. Equation (4.5) may also be applied to a contrast agent if one is used. In this case, the time constant is related to contrast agent, and the unit of time is seconds.

The region inside r_0 is a fluid reservoir. We assume the fluid is incompressible. Some of the fluid flows into this region until the pressure is balanced (at a steady state) and reaches p_0. During this process, less fluid will flow inside and more will flow outside. Therefore, the flow rate at the tumor's periphery will increase. This causes the fluid velocity to increase. Correspondingly, p_0 may be elevated, which means TIFP in the entire tumor area will increase and Starling's law will adjust the leaky source until a new balance (steady state) is reached. Then, r_0=r_n before p_0 reaches p_m since there is no fluid source inside r_n. Whether p_0 can reach p_m or not depends on the drainage ability of the tumor. If p_0 reaches p_m, the radius r_0 will be between r_n and R (r_n<r_0<R), and only the blood vessels beyond r_0 can leak out fluid since those within have an elevated TIFP p, which is caused by the fact that they all satisfy the equation $J_s(r \le r_0)=LA(r \le r_0)(p_m-p)=0$. Thus, at steady state, the total fluid flux leaking from the blood vessels should be the same (balanced) as the rate of fluid outflow from the tumor. The weaker the drainage ability of the tumor periphery, the bigger the r_0. The fluid source and drain can become balanced this way. The schematic of the IFP in the central area (r<r_0) with different drainage abilities at tumor periphery is shown in Fig. 4.5.

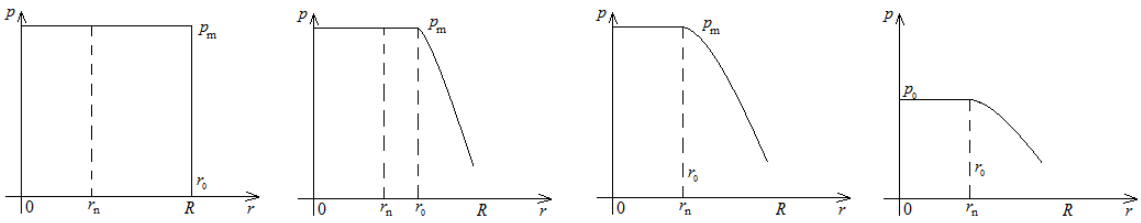

TIFP in a tumor with closed boundary

Variation of TIFP in the central area (flow rate at tumor periphery increases from left to right)

Fig. 4.5 Schematics of IFP in the central area (r<r_0)

4.3 TIFP in the Periphery

With pressure in the necrotic core gradually increasing, less fluid flows in while more fluid flows out. When the pressure in the necrotic core reaches the pressure barrier value p_0, no more fluid will flow inward; instead, they flow outward. During this process, if the lymphatics at the periphery are capable of draining the fluid away in time, the pressure $p(R)$ there may remain zero (relative to the atmosphere) or become the same as that of the environment. Otherwise, $p(R)$ may increase, which means p_0 will likely be elevated. Note that once p_0 changes, Starling's law will adjust the fluid flux to make the fluid source balance the sink/drain. A new steady state is then formed, but the fluid flux can still be described by equation (4.2). When R-r_0 is small, an approximate equation similar to equation (4.4) may be applied:

$$u(R) = 2K\frac{p_0 - p(R)}{R - r_0}, \quad \text{or} \quad p(R) = p_0 - \frac{(R - r_0)u(R)}{2K} \tag{4.6}$$

Equation (4.6) connects p_0, $p(R)$ and $u(R)$ together. Therefore, we can estimate the value of p_0 by measuring $p(R)$ and $u(R)$. Velocity $u(R)$ has been measured in the past through invasive means [81]. There is a potential for measuring $u(R)$ non-invasively by using a contrast enhanced imaging modality, such as computed tomography (CT), magnetic resonance imaging (MRI), and ultrasound (US) [134, 135]. MRI has a particularly high potential because it has the best spatial resolution. However, it does suffer from poor temporal resolution and the signal intensity is not linearly proportional to the amount of contrast agent in the tissue.

If $u(R)$ increases, p_0-$p(R)$ also increases. When $p(R) = 0$, $u(R) = 2Kp_0/(R\text{-}r_0)$. Therefore, if $u(R) \geq 2Kp_0/(R\text{-}r_0)$, $p(R) = 0$; if $u(R) < 2Kp_0/(R\text{-}r_0)$, $p(R)>0$. We define critical fluid velocity as $u_c(R) = 2Kp_0/(R\text{-}r_0)$. For instance, let p_0=15 mmHg, K=4.13×10^{-8} cm^2/mmHg.s [80, 85], r_0=0.9cm, and R=1.0cm. We get $u_c(R)$ = 0.124μm/s or 0.5mm/hour, which corresponds to the results for isolated tumors [80]. Butler et al. [136] measured the flow

rate of some solid tumors. Based on the data, Baxter and Jain [80] estimated that fluid velocity at the periphery of isolated tumors is 0.13-0.2μm/sec. For Gd-DTPA, a widely used MRI contrast agent, we would expect fluid flow in tumor to have an order of magnitude in millimetres per second. Depending on what iodide is bound to, the order of magnitude can be the same for iodinated contrast agents that are widely used in CT.

According to the discussion above, we may conclude that the TIFP $p(R)$ at the periphery is zero if the drainage ability of tumor lymphatics is large enough to ensure that maximum drainage Q_m is greater than the critical flow rate Q_c: $Q_m \geq Q_c = 4\pi R^2 u_c(R) = 8K\pi R^2 p_0/(R-r_0)$. For a tumor with R=1.0cm, $Q_c = 1.56\times10^{-4}$ml/sec. Therefore, if $Q_m < Q_c$, the drainage ability is small, meaning TIFP at the periphery will be high. When the TIFP at the periphery is too high, the tumor must find a way to release the pressure by creating channels that connect with normal tissue. Unfortunately, this may cause the breakdown of normal tissues at the interface or make it complicated. In this case, the fluid flux Q at a tumor edge satisfies the condition $Q_m < Q = 4\pi R^2 u(R) < Q_c$. The drainage ability Q_m may be a factor for determining whether the tumor is isolated or embedded. When $Q<Q_m$, no tumor fluid flows into normal tissue. It is limited to the tumor, and we define this kind of tumor as an isolated one. When $Q>Q_m$, tumor fluid flows into normal tissue and forms an intermediary region between tumor and normal tissue, making the structure complicated. The tumor appears to be enclosed by normal tissue, and is defined as an embedded tumor. Some fluid crosses over the edge ($r=R$) and flows into normal tissue. There, lymphatics are plenty and functional, so some of the fluid is drained away. Similar to Starling's law, the net fluid flux drained from the lymphatics may be expressed as [80]: $\Delta J_L = L_L \Delta A_L(r)(p - p_L)$, where $R<r<r_m$. L_L is the hydraulic conductivity of lymphatics, p_L the pressure in lymphatics, and r_m the maximum spreading radius (defined as the radius where pressure becomes the same as that of normal tissue). When balanced, the pressure p_L in lymphatics should be the same as that of the environment, p_∞. Total surface area of the lymphatics within radius r_m is $A_L(r_m)$. At steady state, the radius is a fixed value; therefore, $A_L(r_m)$ is fixed. Since no fluid collects outside the tumor, the total fluid flux across the tumor edge should be conserved. Assume that the lymphatics are uniformly distributed. A fraction of the volume contains the same

fraction of the surface area of the lymphatics. Thus, the fluid velocity $u(r)$ at the surface of radius r satisfies the following equation (since p is not uniform, we need to integrate the J_L):

$$Q = 4\pi R^2 u(R) = Q_m + 4\pi r^2 u(r) + \frac{3L_L A_L(r_m)}{4\pi(r_m{}^3 - R^3)} \int_R^r 4\pi r^2 (p - p_L) dr \qquad (R<r \le r_m) \qquad (4.7)$$

Considering $u(r)=-K\mathrm{d}p/\mathrm{d}r$, the derivative of eq. (4.7) can be written as:

$$r^2 \frac{d^2 p}{dr^2} + 2r \frac{dp}{dr} - \frac{3L_L A_L(r_m)}{4\pi K(r_m{}^3 - R^3)} r^2 (p - p_L) = 0 \qquad (4.7')$$

The boundary conditions are: $p\big|_{r=R} = p(R)$, $\left.\frac{dp}{dr}\right|_{r=R} = -\frac{Q - Q_m}{4\pi R^2 K}$, and $p\big|_{r=r_m} = p_L$. If we let $\Lambda = \frac{3L_L A_L(r_m)}{4\pi K(r_m{}^3 - R^3)}$, we get

$$p(r) = \frac{C_1 \sinh(\sqrt{\Lambda} r) + C_2 \cosh(\sqrt{\Lambda} r)}{r} \qquad (R< r \le r_m) \qquad (4.8)$$

where $C_1 = \frac{p(R)}{\sqrt{\Lambda}} \cosh(\sqrt{\Lambda} R) - R p(R) \sinh(\sqrt{\Lambda} R) - \frac{Q - Q_m}{4\pi K R \sqrt{\Lambda}} \cosh(\sqrt{\Lambda} R)$,

$$C_2 = -\frac{p(R)}{\sqrt{\Lambda}} \sinh(\sqrt{\Lambda} R) + R p(R) \cosh(\sqrt{\Lambda} R) + \frac{Q - Q_m}{4\pi K R \sqrt{\Lambda}} \sinh(\sqrt{\Lambda} R).$$

If the drainage of the lymphatics is small, the third term on the right hand side of (4.7) can be ignored. The solution is reduced to

$$p(r) = p(R) - \frac{4\pi R^2 u(R) - Q_m}{4\pi K} \left(\frac{1}{R} - \frac{1}{r}\right) \qquad (r > R) \qquad (4.8')$$

Here, $p(R)$ and $u(R)$ are related by equation (4.6). Usually, p_0 is determined by the distribution of the capillaries and their permeability. Therefore, if we know the velocity or pressure at the tumor edge $r=R$, we may find the pressure distribution in the interface area between tumor and normal tissue. Consequently, any noninvasive measurement of fluid flow velocity may enable us to find the TIFP.

Now let us determine the TIFP distribution in region $r_0<r<R$ more accurately. We may not be able to obtain the exact pressure distribution there since we do not know the pressure gradient. Also, the fluid flux is not conserved. However, we know the TIFP at surfaces $r=r_0$ and $r=R$, as well as their tangent values. We can use the continuity condition to determine a function of TIFP, which reflects the main features of the actual TIFP. Since this region is narrow, this approach should be good enough for describing real situations:

(1) The drainage ability Q_m is greater than the critical flow rate Q_c ($Q_m>Q>Q_c$). Under this condition, $p(r_0)=p_0$, $dp(r_0)/dr=0$ and $p(R)=0$. We can use a quadratic function to express the values and get:

$$p(r)=-\frac{p_0}{(R-r_0)^2}[r^2-2r_0r+R(2r_0-R)] \qquad (r_0<r<R) \tag{4.9}$$

(2) The fluid flux Q at the periphery is smaller than both the drainage ability Q_m and the critical flow rate Q_c: $Q<Q_m$ and $Q<Q_c$. Now, $p(r_0)=p_0$, $dp(r_0)/dr=0$ and $p(R)=p_\infty\neq 0$, which gives:

$$p(r)=-\frac{1}{(R-r_0)^2}[(p_0-p_\infty)r^2-2r_0(p_0-p_\infty)r-R^2p_0+2Rr_0p_0-r_0^2p_\infty] \qquad (r_0<r<R) \tag{4.9′}$$

Here we use p_∞ since it can be measured even though it may be related to Q_m and Q_c.

(3) The drainage ability Q_m is smaller than the fluid flux Q ($Q_m < Q < Q_c$). Under this condition, $p(r_0)=p_0$, $dp(r_0)/dr=0$, $p(R)$ value, and $dp(R^-)/dr=dp(R^+)/dr$. After we apply a cubic fit and combine it with equation (4.8), we get: $p(r)=ar^3+br^2+cr+d$, where

$$a=\frac{2[p_0-p(R)]-(R-r_0)A}{(R-r_0)^3};$$

$$b=\frac{(R+2r_0)(R-r_0)A-3(R+r_0)[p_0-p(R)]}{(R-r_0)^3};$$

$$c=\frac{6Rr_0[p_0-p(R)]-r_0(R-r_0)(2R+r_0)A}{(R-r_0)^3};$$

$$d=\frac{R^3p_0-r_0^3p(R)-3R^2r_0p_0+3Rr_0^2p(R)+Rr_0^2(R-r_0)A}{(R-r_0)^3};\qquad A=\frac{Q-Q_m}{4\pi R^2K}.$$

If we let p_0=15mmHg, K=4.13×10^{-8}cm^2/mmHgSec [80, 88], r_0=0.9cm, and R=1.0cm, we get $u_c(R)$=0.124μm/sec or Q_c=1.56×10^{-4}ml/sec. Fig. 4.6 shows TIFP distribution at steady state for different cases of flow rate: a) $Q_m \geq Q > Q_c$, which causes $p(R)$=0; b) $Q<Q_m$ and $Q<Q_c$, Q=5.19×10^{-5} ml/sec; and c) $Q_m<Q<Q_c$. Cases a) and b) are for "isolated" tumors and case c) is for "embedded" ones. The slope of the IFP outside the tumor is dependent on flow rate across the surface $Q(R)$ and the drainage ability at the periphery of the tumor.

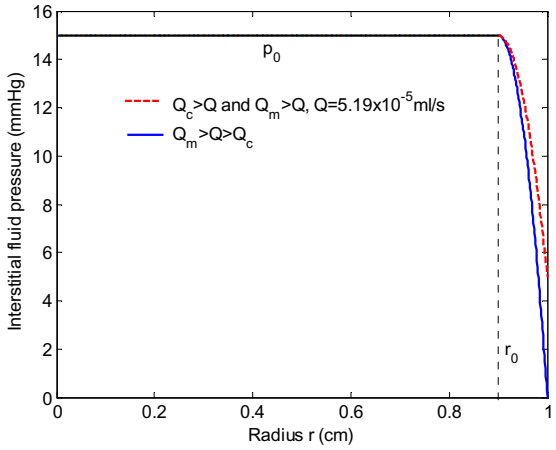

(a) $Q_m>Q$ ("Isolated" tumor)

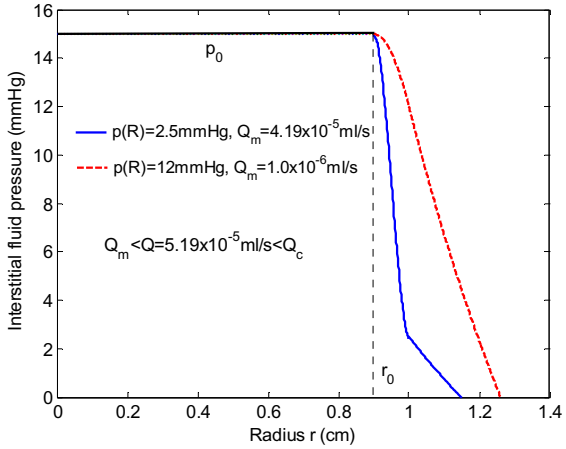

(b) $Q_m<Q$ ("Embedded" tumor)

Fig. 4.6 TIFP distribution at steady state

4.4 Time Dependent TIFP

For an incompressible fluid, the increase rate of its volume equals that of the fluid source plus the inflow rate minus the fluid sink/drain and outflow rate (here we ignore diffusion).

$$\frac{\partial V_F}{\partial t} = J_s + \oiint \vec{u}_1 \cdot d\vec{S}_1 - J_d - \oiint \vec{u}_2 \cdot d\vec{S}_2 \tag{4.10}$$

Here, V_F is the total fluid volume in the tumor area, J_s the fluid source and J_d the fluid drain/sink. There is no lymphatic drainage in the tumor, so J_d=0. Lymphatic drainage only exists at the periphery, and we take it as a constant, Q_m. The second term on the right side of equation (4.10) represents the fluid inflow rate, while the fourth term represents the outflow rate. Since no fluid flows into the tumor from the outside, equation (4.10) can be simplified as:

$$\frac{\partial V_F}{\partial t} = J_s(t) - J_d(t) - \oiint \vec{u}_{drain} \cdot d\vec{S} \tag{4.11}$$

In normal tissue, blood vessels grow harmoniously with the tissue and lymphatics are functional, so the interstitial fluid is balanced. We assume that all capillaries have the same L,σ, pressure difference p_V-p and osmotic pressure difference π_V-π. However, tumor capillaries are deformed, and different ones may have varying deformities. This means that they may have dissimilar L, σ and π_V-π, though p_V may stay the same. Also, the pressure p may be spatially dependent. The total fluid flux at time t can be expressed as:

$$J_s(t) = \sum_i J_i(t) = \sum_i L_i(t) A_i(t) [p_V - p_i(t) - \sigma_i \Delta\pi_i(t)] \tag{4.12}$$

where $\Delta\pi_i$ is the osmotic pressure difference. The faster a tumor grows, the more deformed the capillaries are. This causes the value of the hydraulic conductivity to increase; therefore, the permeability of the capillaries will also increase. The thinner the capillaries, the smaller the osmotic pressure difference. When the capillary is broken (or

there is a big hole in the capillary), the osmotic pressure $\Delta\pi_i$ becomes zero. Most capillaries are concentrated near the edge, and their conductivity in this area is greater than that in the central region. Also, the osmotic pressure difference is smaller in this area. The total fluid flux near the edge should be much greater than that in the central area. We use the total fluid flux near the edge to represent that of the tumor. In this narrow area, the values of the parameters (L, σ and $\Delta\pi$) should not change much. We take them as constants and use the average value to represent them. Thus,

$$J_s(t) = \overline{L}(t)[p_V - \overline{p}(t) - \overline{\sigma}\Delta\overline{\pi}(t)]\sum_i A_i(t) = \overline{L}(t)A(t)[p_V - \overline{p}(t) - \overline{\sigma}\Delta\overline{\pi}(t)] \tag{4.13}$$

where $A(t)$ is the total surface area of blood vessels at time t. Substituting equation (4.13) into equation (4.11), we have

$$\frac{\partial V_F(t)}{\partial t} = \overline{L}(t)A(t)[p_V - \overline{p}(t) - \overline{\sigma}\Delta\overline{\pi}(t)] - J_d(t) - \oiint \vec{u}_{drain} \cdot d\vec{S} \tag{4.14}$$

TIFP should be related to the accumulated amount of fluid in a tumor. As we know, the more the fluid accumulates, the higher the pressure rises. Reference [137] experimentally showed that TIFP is linearly related to tumor water content. We assume this content is proportional to the amount of accumulated fluid. The fluid's effect should be relative to tumor size. If the size is large, the pressure may not be high despite the large quantity of accumulated fluid. By contrast, if the tumor size is small, a slight amount of accumulated fluid may cause high pressure. We assume that the average pressure $\overline{p}(t)$ has a linear relationship with the ratio of the amount of accumulated fluid to the size (volume) of the tumor, and is expressed as $\partial\,\overline{p}\,/\partial t = \gamma \partial V / V_{\text{tumor}} \partial t$. Thus,

$$\frac{\partial \overline{p}(t)}{\partial t} = \gamma \frac{Cm_c}{m(t)}\{\overline{L}(t)A(t)[p_V - \overline{p}(t) - \overline{\sigma}\Delta\overline{\pi}(t)] - J_d(t) - \oiint \vec{u}_{drain} \cdot d\vec{S}\} \tag{4.15}$$

where γ is a coefficient and m_c the mass of a tumor cell. Angiogenesis is an important property of tumors. Therefore, $A(t)$ is different at various stages of tumor growth, and it usually increases with the progression of stage. When a tumor grows at a fast rate, its size (m) increases quickly, and the state of its blood vessels changes rapidly. This may cause $\overline{L}(t)$ to increase and $\Delta\overline{\pi}(t)$ to decrease. At the fast growth stage, it is difficult to

determine the parameters. However, when a tumor is almost mature ($m \approx M$), all parameters tend to remain constant. Thus,

$$\frac{\partial \bar{p}(t)}{\partial t} = \gamma \frac{Cm_c}{M} \{ \bar{L}A[p_V - \bar{p}(t) - \bar{\sigma}\Delta\bar{\pi}] - J_d(t) - \oiint \vec{u}_{drain} \cdot d\vec{S} \} \tag{4.16}$$

The solution for equation (4.16) depends on the boundary conditions and initial conditions. It is difficult to get a general analytical solution. We are interested in the spatial distribution of pressure in a tumor. Here we consider the steady state condition $\partial p(r,t)/\partial t = 0$, which gives the equation

$$\bar{L}A[p_V - \bar{p}(r) - \bar{\sigma}\Delta\bar{\pi}] - J_d - \oiint \vec{u}_{drain} \cdot d\vec{S} = 0 \tag{4.17}$$

Here we consider the spherical symmetry case and take the tumor as a porous medium. Based on the discussions in sections 4.1, 4.2 and 4.3, we divide the domain into three regions: $r<r_0$, $r_0<r<R$ and $r>R$. In the central region ($r<r_0$), fluid does not flow at steady state and $\boldsymbol{u}_{\text{drain}}=0$. The TIFP is uniform. Thus, equation (4.17) gives:

$$p(r) = p_0 = p_V - \bar{\sigma}\Delta\bar{\pi} - \frac{J_d}{\bar{L}A} \qquad (r<r_0) \tag{4.18}$$

This provides a constant solution. If $J_{\text{d}}=0$, the equation becomes $p(r) = p_0 = p_V - \bar{\sigma}\Delta\bar{\pi} = p_m$. The results correspond with the cases that were discussed in sections 4.1 and 4.2. Since the outflow velocity u_{drain} is unknown in the region $r_0<r<R$, we cannot use equation (4.17) to get its pressure distribution. At steady state, the fluid leaked from capillaries in the region $r>R$ should be equal to the total fluid flux across the edge ($r=R$):

$$\bar{L}A[p_V - \bar{p}(r) - \bar{\sigma}\Delta\bar{\pi}] = 4\pi R^2 u(R) \tag{4.19}$$

Considering lymphatic drainage, we can also derive equation (4.7) from equations (4.17) and (4.19). The results from section 4.3 can be applied, and are consistent with the situations that were discussed above.

According to the present model, p_0 and r_0 are the most important parameters. It represents the IFP in the central area of a tumor at steady state. When $r_0>r_{\text{n}}$ (including the case where there is no necrotic core, meaning $r_{\text{n}}=0$), $p_0=p_{\text{m}}=p_V-\sigma(\pi_V-\pi)$. In this case, IFP in

the central region is determined by the conditions of the vascular vessels in the tumor. When $r_0=r_n$, the situation becomes complicated, and p_0 is between 0 and p_m ($0<p_0<p_m$). The value can be estimated by using equation (4.6), as mentioned above in section 4.3. It is quite possible to estimate the values of r_0 and r_n through noninvasive means, such as MRI and CT. Lee et al. [137] found that tumor water content correlated significantly with TIFP. They actually showed that TIFP has a linear relationship with tumor water content. The line of best fit indicated that water content increased from 79% to 85% when TIFP increased from ~2 to ~14 mmHg for tumors (<500mm^3). Leunig et al. [138] also found that TIFP correlated with tumor water content after they applied photodynamic therapy (PDT) to the amelanotic melanoma of a hamster. Some MRI images also suggested that TIFP is related to tumor water content [123-1142]. Image contrast of MRI in the central region is distinct from that in the outer region. These results strongly imply that tumor central region contains more water (protons), which coincides with the present model at steady state. Lyng et al. [143] suggested that there is no correlation between TIFP and T_1 or T_2. Haider et al. [142] studied the correlations between DCE-MRI and IFP of cervical cancer in vivo and found that there is a moderate negative correlation between IAUC(60m), which is the initial area under the enhancement curve (relative to muscle), permeability (rk_{trans}), and IFP. Hassid et al. [140, 141] suggested that the steady-state distribution of Gd-DTPA concentration in tissues reflected the TIFP distribution. Gulliksrud et al. [139] concluded that DCE-MRI may be developed into a useful noninvasive method for assessing TIFP without necrosis through the relation between $E{\cdot}F$ and TIFP (where E is the initial extraction fraction of Gd-DTPA and F the blood perfusion). It is noteworthy that the water content can only relatively reflect the IFP in a tumor since MRI is based on the density of water (protons). It shows only the variation of IFP in that tumor. Two different tumors may not have the same IFP, even if they have the same water content. This is due to the differences between their size and fluid composition. For example, if some other incompressible matter such as collagens has occupied the volume in the central region of a tumor, water may not enter. Even so, it does not mean that the pressure is lower there. Even in the same tumor, the distribution of water in the central region may not be even. Less water density in a small local region might not mean a low IFP there. It may be more reliable to determine r_0 and r_n

noninvasively and then estimate the IFP. Though we use a spherical model to describe the distribution of interstitial fluid and the pressure for convenience's sake, it is not necessarily limited to a spherical structure. We may use the distribution difference of water content or the structure features of tumor to determine r_n, or more generally, the necrotic region; and use the properties of velocity to determine r_0 or the region with uniform IFP, p_0. Before reaching steady state, the contrast agent flows inwards in the region $r<r_0$ and outwards in the region $r>r_0$. After reaching steady state, the contrast agent is stationary in the region $r<r_0$ but flows outwards in the region $r>r_0$. Once we know r_0 and the pressure or velocity at R (meaning the value of R), we can find the TIFP distribution in the area from r_0 to R based on eq. (4.9) or (4.9'). However, currently there is no general formula for TIFP distribution, so we must calculate the values of different points or different gradient directions.

Ultrasound is also a method of noninvasive measurement. It is well established as a means of measuring blood flow/velocity [135]. Similarly, fluid velocity may also be estimated using the Doppler principle.

In the present work, we illustrate the relationship between TIFP and fluid flow. A dynamic measurement of contrast agent that is streaming away from a central mass may provide an estimation of fluid flow, and consequently of TIFP. This work may present a practicable method for determining TIFP quantitatively and noninvasively. Since TIFP is a critical predictor of tumor response to non-surgical cancer treatments, the methods proposed have a strong and practical clinical potential.

4.5 Noninvasive Measurement of TIFP with MRI

The principle of MRI is introduced in Appendix 3. We derive some formulae in order to better understand the principle of image contrast.

We should understand which variables relate MRI to TIFP and in what way when using it to measure the pressure. From the discussion above, we know that the image intensity of MRI is related to the equilibrium magnetization M_0, the relaxation constants T_1 and T_2, as well as the frequency of RF signal ω and its altitude B_1. Due to the formula for M_0, we find that it is also related to the density of protons N, the applied magnetic field B_z, the gyromagnetic ratio γ, and the temperature T. Unlike image intensity of MRI, TIFP in the central region is related to the amount of accumulated fluid [72]. Its distribution at the periphery of the tumor is related to the fluid flux Q (and correspondingly the fluid velocity) there, the pressure of the environment $p(R)$, the drainage ability Q_m, etc. Proton density N is the variable common to both high TIFP and image intensity of MRI. The more water is accumulated, the higher the TIFP in a given tumor. The problem is that we cannot determine the TIFP just by measuring the amount of water. Therefore, there must be a reference point for comparison where the TIFP is known. Since many factors affect the image intensity of MRI, it is necessary to keep some variables as constants. In fact, the water/proton density in the necrotic core is the largest. Correspondingly, the intensity/brightness of MRI in this area should be the strongest. Therefore, we can use the change in MRI brightness to determine the interface of the necrotic core (r_n) using spin density weighted MRI. Fluid flows outward outside r_0 and inward inside r_0, and the fluid velocity is zero at r_0 before reaching steady state. No more fluid flows inward afterwards. DCE-MRI and DSC-MRI (see appendix 4) may be used to measure fluid flow and determine the position of r_0, where the fluid is stationary.

A minimally invasive measurement of TIFP is possible based on the model presented. We illustrate the approach using an MRI protocol that could be a simple extension of current standard practice.

MRI diagnostic tests often use a vascular contrast agent to delineate a suspicious mass prior to a biopsy procedure. Depending on the imaging sequence used, the apparent tumor volume may vary and in fact appear to increase with duration (measured in minutes) after the administration of a contrast agent. This phenomenon is shown in figure 4.7 using a pulse sequence and image analysis technique sensitive to the presence of contrast. The result shown reflects a contrast agent wave front, which appears to

increase as a function of time while contrast agent streams at a velocity $u(R)$ from the tumor into surrounding normal tissue. The rate of flux of contrast agent is proportional to TIFP, which is relative to that of surrounding normal tissue (usually near zero).

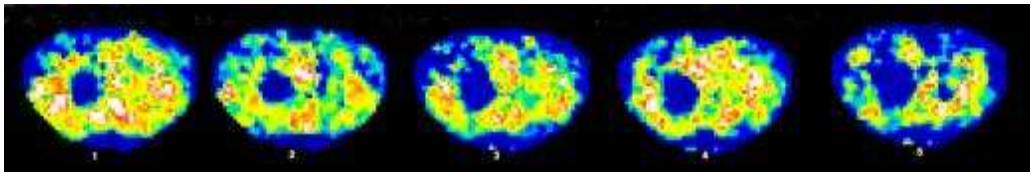

Fig. 4.7 Demonstration of the consequence of high TIFP on contrast agent kinetics in a rat 9L cerebral glioma acquired using a 7 Tesla MRI. The five panels are ratio images of T2* to T1 relaxivities, so called "Gamma-2 images", calculated from minute 3 to 15 at 2.5 minute intervals after the injection of a contrast agent (Gadomer) and shown from left to right. The movement of the contrast agent wave front (blue circular region) in normal tissue is clearly visualized across this time period.

Though a spherical model is used in the analysis presented, the theory is not limited to spherical geometry since contrast agent flux at irregular boundaries can be modeled at various gradient directions perpendicular to the tumor boundary. However, as an approximation, a simple spherical model may be adequate for describing the contrast agent kinetics at a distance away from most tumors. Usually, the shape of a tumor and its vascular distribution are not spherically symmetric. Even so, we can still determine the central area from the MRI despite its irregularity. However, now there is no general formula for TIFP distribution and we have to calculate the values of different points or different gradient directions.

Any imaging modality capable of monitoring the dynamics of a contrast agent can be used to determine TIFP, including MRI, CT, US and perhaps PET (Positron emission tomography) and SPECT (Single-photon emission computed tomography). For MRI (shown in Fig. 4.7), the dyed contrast agent can visualize the fluid flow, which is correlated to TIFP variation.

In conclusion, a model describing the formation and distribution of TIFP is presented with an experimental illustration of the kinetics of contrast agent, opening up the possibility of minimally invasive TIFP measurements.

In some cases of actual clinical application, we only need to know the variation in TIFP in order to judge the effects of therapy. In this case, the change in TIFP within the central area is most important since it reflects change in TIFP distribution and variation in fluid velocity. A contrast agent not only makes the fluid flux visible, but also strengthens, speeds up and magnifies the process of the tumor interstitial fluid movement. Before contrast agent is applied, TIFP in the central region might be uniform at a certain value. After a contrast agent is injected, more fluid leaks out from the capillaries in the tumor. Therefore, TIFP in the central region is smaller than the value of the pressure barrier p_0. Some of the fluid flows inward to the central area and accumulate there. Thus, r_0 becomes larger and pressure increases. With increase in time, the pressure in the central area eventually reaches p_0. A new balance is reached and r_0 becomes maximal. After this occurs, all fluid flows outwards. The change in p_0 affects TIFP distribution. Therefore, it causes variation in the motion of the fluid. This implies that if we can maintain the same amount of contrast agent and tumor environment conditions, we may compare the TIFP variation of a tumor before and after treatment by observing the movement of contrast agent, which can be shown clearly through MRI. Though this experiment may not be able to demonstrate the change in r_0, it clearly shows the motion of the fluid, which implies that MRI is a promising tool in tumor therapy. We may compare the rate of change in the dyed contrast agent area and predict the change in TIFP within the central area.

Chapter 5. Discussion and Conclusion

By decomposing cell proliferation rate into cell production and death rates and introducing cell additional death rate under therapy, we developed a general model for tumor growth, metastasis and response to therapy. For a multicellular system, we introduced rules for similarity of growth ($E_i/C_i = \beta^o$ and $M_i = x_i M$). If different types of cells satisfy these relations, the fractions will not change and they grow harmoniously. However, when they respond to treatment differently, we can detect the variation. As we have pointed out, normal cells usually satisfy the rules but tumor cells may not. This study confirms that there are some cells resistant to both radiation and chemotherapy in all experimental data, which is shown through curve fittings. Also, eq. (3.3.9) fits these experimental data better than any existing models. The results show us that some radioresistant cells (~1-10%) exist for both radiation and chemotherapy. For a two subpopulation system, we introduce a rule of equal ratio of α to β for different types of cells since they are under the same radiation field. This is different from the two component LQ model (which may cause the parameters to be redundant). This way, we use the least amount of parameters to get the best curve fit.

This model consistently explains cell response to both high and low LET radiations. It may also be applied to describe cell response to radiation and chemotherapy, both in vitro and in vivo. It also shows that the LQ model is an approximation of the present model under a specific condition: the total death rate, which includes additional death rate caused by treatment and natural death rate, is much greater than the production rate.

Through reading this dissertation, we know that there is a “universal” governing equation for an organism’s growth and development. It includes both biological (growth terms) and physical (mass flux terms) activities, and can be applied to tumor growth, metastasis as well as response to therapy. Therapies cause an additional death rate (relative to the natural death rate). The present model connects the consequence of treatment with the growth process of a biosystem. Based on this idea, we also applied this model to explain

the result of antiangiogenic therapy, which mainly controls the production rate by damaging nutrition supply. We may be able to apply this idea to cell mutation (change to other species with different M and $\beta°$) and other therapies.

The present model is based on the condition of constant number density. It is reasonable since the energy for maintaining the metabolism of a single cell is fixed. This means that the size of a single cell (m_{ck} and r_{ck}) is constant. Correspondingly, the number density of cells C_k is a constant. In West's model, M is the asymptotic mass for organism growth in unrestricted dietary conditions. Relation $E/C=aM^{-1/4}$ shows that the growth parameter a decreases when M decreases, which slows down the growth rate dm/dt. The system can still grow harmoniously and isotropically when this happens. We sort identical cells into a particular system (tissue/organ) and use the rules of similarities of growth to unite the systems. It is noteworthy that different types of normal cells follow the rules and grow harmoniously and isotropically, while cells in a benign tumor may but those in a malignant one may not. In fact, M must depend on nutrition concentration c_n and oxygen concentration c_o, which are very important for organism growth. We need further studies in order to determine the function $M=M(c_n,c_o)$. Nutrition supply might make organism growth complicated.

We also investigated the distribution of TIFP and its possible noninvasive measurement. Due to the drainage deficiency of the lymphatic system, the resistance of collagen and elastic fiber network, as well as their interactions, the leaked fluid forms a pressure barrier [72], which contributes to the elevated pressure in the central region. This pressure barrier worsens the metabolism and treatment of a biosystem. According to our model [72], the pressure barrier is formed by the leaky blood vessels in the vascularized region. This pressure barrier limits (even prevents) the exchange of substances, decreases (even damages) metabolism in the central region, and obstructs drug delivery. No nutrition or oxygen can be supplied and no waste can be carried out efficiently. Even if the central region had a lower TIFP [81] before steady state, leaked fluid can fill this region quickly and reach the same TIFP as the pressure barrier. Substances in the central region are nearly confined there. When a tumor grows larger, the vascular vessels develop outwards; therefore, the pressure barrier expands outwards. This aids in

enlarging the necrotic core. Based on our model, p_0 and r_0 are the two most important variables. At steady state, TIFP within area r_0 is uniform and equal to p_0. Before reaching steady state, the contrast agent flows inwards in the region $r<r_0$ but outwards in the region $r>r_0$. After reaching the steady state, the contrast agent stays still in the region $r<r_0$ but flows outwards in the region $r>r_0$. We may use the velocity property to determine r_0 or the uniform IFP p_0 region. We can estimate the value of p_0 by measuring $p(R)$ and $u(R)$, as shown in Ref. [72]. There is potential to measure $u(R)$ non-invasively using a contrast enhanced imaging modality, such as computed tomography (CT), magnetic resonance imaging (MRI), or ultrasound (US). Once we know p_0 and $p(R)$, we can estimate the gradient of TIFP and get the approximate distribution of TIFP at the tumor periphery.

Although the model described TIFP formation and distribution as well as its noninvasive measurement, a lot of work must be done before clinical application. Many parameters need to be determined in practice. Specifically, how to estimate the p_v and $\sigma\Delta\pi$ in the tumor area since they might be different from those in normal tissue. Can we use the parameters for normal tissue to speculate about those for a tumor? How can we determine the fluid drainage ability Q_m on the periphery of a tumor? To find solutions for these questions, we still need to study some typical experiments. In the present model, we used a spherical structure to derive the TIFP distribution. However, many tumors have an irregular necrotic core and outline of the periphery. How to deal with these conditions practically will also require further studying. Since the order of magnitude of the fluid velocity is small (~0.1μm/sec.), the method of measurement should have a very high definition. In addition, standardizing the parameters for non-invasive measurement is essential, which makes it easy to perform and operate. Exploring an economic way for non-invasive measurement will be beneficial and practical for clinical use.

References

[1] R. P. Araujo and D. L. S. McElwain, A history of the study of solid tumor growth: the contribution of mathematical modelling, Bulletin of Mathematical Biology 66 (2004) 1039-1091.

[2] James L Connolly, Stuart J Schnitt, Helen H Wang, Ann M Dvorak and Harold F Dvork, Principles of cancer pathology, Cancer Medicine, 5th edition, BC Decker (2000) chapter 29.

[3] http://health.nytimes.com/health/guides/disease/tumor/overview.html.

[4] A. K. Laird, Dynamics of tumor growth, British Journal of Cancer 18 (1964) 490–502.

[5] A. K. Laird, S. A. Tyler and A. D. Barton, Dynamics of normal growth, Growth 21 (1965) 233–248.

[6] Gompertz function, en.wikipedia.org/wiki/Gompertz_function.

[7] G. G. Steel, Growth Kinetics of Tumors, Oxford: Clarendon Press (1977).

[8] T. E. Wheldon, Mathematical Models in Cancer Research, Bristol, Adam hilger (1988).

[9] R. H. Thomlinson and L. H. Gray, The histological structure of some human lung cancers and the possible implications for radiotherapy. British Journal of Cancer 9 (1955) 539–549.

[10] Eric J. Hall, Amato J. Giaccia, Radiobiology for the Radiologist, 6th ed., Lippincott Williams & Wilkins, Philadelphia (2006).

[11] A. C. Burton, Rate of growth of solid tumours as a problem of diffusion, Growth 30 (1966) 157–176.

[12] H. P. Greenspan, Models for the growth of a solid tumor by diffusion, Studies in Applied Mathematics 52 (1972) 317-340.

[13] Tiina Roose, Jonathan S. Chapman, Philip K. Maini, Mathematical models of avascular tumor growth, SIAM 49 (2007) 179-208.

[14] S. C. Ferreira, Jr., M. L. Martins, and M. J. Vilela, Reaction-diffusion model for the growth of avascular tumor, Physical Review E 65 (2002) 021907.

[15] Alessandro Bertuzzi, Antonio Fasano, Alberto Gandolfi, Doriana Marangi, Cell kinetics in tumor cords studied by a model with variable cell cycle length, Mathematical Biosciences 177 (2002) 103-125.

[16] J. Ward and J. King, Mathematical modelling of avascular-tumor growth, IMA Journal of Mathematics Applied in Medicine and Biology 14 (1) (1997) 39–69.

[17] D Fernández Slezak, C Suárez, A Soba, M Risk and G Marshall, Numerical simulation of avascular tumor growth, Journal of Physics: Conference Series 90 (2007) 012049.

[18] M. A. J. Chaplain, L. Graziano and L. Preziosi, Mathematical modelling of the loss of tissue compression responsiveness and its role in solid tumor development, Mathematical Medicine and Biology 23 (2006) 197-229.

[19] Markus Basan, Thomas Risler, Jean-François Joanny, Xavier Sastre-Garau, and Jacques Prost, Homeostatic competition drives tumor growth and metastasis nucleation, HFSP J. 3 (2009) 265-272.

[20] Christophe Deroulers, Marine Aubert, Mathilde Badoual, and Basil Grammaticos, Modeling tumor cell migration: From microscopic to macroscopic models, Physical Review E 79 (2009) 031917.

[21] C.F. Lo, Stochastic Gompertz model of tumor cell growth, Journal of Theoretical Biology 248 (2007) 317–321.

[22] Peter S. Kim, Peter P. Lee, Doron Levy, A PDE Model for Imatinib-Treated Chronic Myelogenous Leukemia, Bulletin of Mathematical Biology 70 (2008) 1994–2016.

[23] Robert A. Gatenby and Thomas L. Vincent, Application of quantitative models from population biology and evolutionary game theory to tumor therapeutic strategies, Molecular Cancer Therapeutics 2 (2003) 919-927.

[24] Paul S. Albert and Joanna H. Shih, Modeling Tumor Growth with Random Onset, Biometrics 59 (2003) 897-906.

[25] P. P. Delsanto, C. A. Condat, N. Pugno, A. S. Gliozzi, and M. Griffa, A multilevel approach to cancer growth modeling, Journal of Theoretical Biology 250 (2008) 16–24.

[26] Helen Byrne and Dirk Drasdo, Individual-based and continuum models of growing cell populations: a comparison, Journal of Mathematical Biology 58 (2009) 657–687.

[27] Dominique Barbolosi, Assia Benabdallah, Florence Hubert,and Federico Verga, Mathematical and numerical analysis for a model of growing metastatic tumors, Mathematical Biosciences 218 (2009) 1–14.

[28] Philip Hahnfeldt, Dipak Panigrahy, Judah Folkman, and Lynn Hlatky, Cancer Research 59 (1999) 4770-4775.

[29] Rakesh K. Jain, Ricky T. Tong, and Lance L. Munn, Effect of Vascular Normalization by Antiangiogenic Therapy on Interstitial Hypertension, Peritumor Edema, and Lymphatic Metastasis: Insights from a Mathematical Model, Cancer Research 67 (2007) 2729.

[30] Robert M. Sutherland, Cell and Environment Interactions in Tumor Microregions: The Multicell Spheroid Model, Science 240 (1988) 177-184.

[31] E. D. Yorke, Z. Fuks, L. Norton, W. Whitmore, C. C. Ling, Modeling the development of metastases from primary and locally, recurrent tumors: comparison with a clinical database for prostatic cancer. Cancer Research 53 (1993) 2987–2993.

[32] M. Kleiber, Body size and metabolic rate, Physiological Reviews 27 (1947) 511-541.

[33] G. B. West, J. H. Brown, B. J. Enquist, A general model for ontogenetic growth. Nature 413 (2001) 628–631.

[34] Caterina Guiot, Piero Giorgio Degiorgis, Pier Paolo Delsanto, Pietro Gabriele, Thomas S. Deisboeck, Does tumor growth follow a “universal law”? Journal of Theoretical Biology 225 (2003) 147–151.

[35] James E. Talmadge and Isaiah J. Fidler, AACR centennial series: The biology of cancer metastasis: historical perspective, Cancer Research 70 (2010) 5649-5669.

[36] Erik Sahai, Illuminating the metastatic process, Nature Reviews Cancer 7 (2007) 737.

[37] Lance Allen Liotta, Jerome Kleinerman, and Gerald M. Saidel, Quantitative relationships of intravascular tumor cells, tumor vessels, and pulmonary metastasis following tumor implantation, Cancer Research 34 (1974) 997-1004.

[38] Lance Allen Liotta, Jerome Kleinerman, and Gerald M. Saidel, The significance of hematogenous tumor cell clumps in the metastatic process, Cancer Research 36 (1976) 889-894.

[39] Robert S. Kerbel, Antiangiogenic therapy: a universal chemosensitization strategy for cancer, Science 312 (2006) 1171.

[40] Melvin Astrahan, Some implications of linear-quadratic-linear radiation dose-response with regard to hypofractionation, Medical Physics 35 (2008) 4161.

[41] Bradly G. Wouters and J. Martin Brown, Cells at intermediate oxygen levels can be more important than the "hypoxic fraction" in determining tumor response to fractionated radiotherapy, Radiation Research 147 (1997) 541-550.

[42] Lourdes M. Garcia, David E. Wilkins, and Gijsbert P. Raaphorst, α/β ratio: a dose range dependence study, International Journal of Radiation Oncology Biology Physics 67 (2007) 587-593.

[43] Frederick W McKenna, Salahuddin Ahmad, Isoeffect calculations with the linear quadratic and its extensions: An examination of model-dependent estimates at doses relevant to hypofractionation, Journal of Medical Physics 36 (2011) 100-106.

[44] Mariana Guerrero, Marco Carlone, Mechanistic formulation of a linear-quadratic-linear (LQL) model: split-dose experiments and exponentially decaying sources, Medical Physics 37 (2010) 4173.

[45] Stanley B. Curtis, Lethal and potentially lethal lesions induced by radiation—a unified repair model, Radiation Research 106 (1986) 252-270.

[46] M. M. Elkind and H. Sutton, X-ray damage and recovery in mammalian cells in culture, Nature 184 (1959) 1293–1295.

[47] K. Stone, H. Wunderli, G. Mickey, and D. Paulson, Isolation of a human prostate carcinoma cell line (DU-145), International Journal of Cancer 21 (1978) 274–281.

[48] J. Leith et al., Radiobiological studies of PC-3 and DU-145 human prostate cancer cells, x-ray sensitivity in vitro and hypoxic fractions of xenografted tumors in vivo, International Journal of Radiation Oncology Biology Physics 25 (1993) 283–287.

[49] D. W. Siemann, Tumour size: a factor influencing the isoeffect analysis of tumour response to combined modalities, British Journal of Cancer 41 (1980), Suppl. IV, 294.

[50] L. D. Skargard, M. W. Skwarchuk, B. G. Wouters, The survival of asynchronous V79 cells at low radiation doses: modeling the response of mixed cell populations, Radiation Research 138 (1994) S72-S75.

[51] B. G. Wouters and L. D. Skarsgard, The response of a human tumor cell line to low radiation doses: evidence of enhanced sensitivity, Radiation Research 138 (1994) S76-S80.

[52] Lloyd D. Skarsgard, Andrew A. Hill and Deanna K. Acheson, Evidence for two forms of substructure in the cell survival curve, Acta Oncologica 38 (1999) 895-902.

[53] Roger W. Howell and Prasad V. S. V. Neti, Modeling multicellular response to nonuniform distribution of radioactivity: Differences in cellular response to self-dose and cross-dose, Radiation Research 163 (2005) 216-221.

[54] W. E. Powers and L. J. Tolmach, A multicomponent x-ray survival curve for mouse lymphosarcoma cells irradiated *in vivo*, Nature 197 (1963) 710-711.

[55] Jeremy N. Rich, Cancer Stem Cells in Radiation Resistance, Cancer Research 67 (2007) 8980-8984.

[56] Maximilian Diehn, Robert W. Cho, Neethan A. Lobo et al., Association of reactive oxygen species levels and radioresistance in cancer stem cells, Nature 458 (2009) 780-783.

[57] S.C. Barranco, Judy K. Novak and Ronald M. Humphrey, Response of mammalian cells following treatment with bleomycin and 1, 3-bis (2-chloroethyl)-1-nitrosourea during plateau phase, Cancer Research 33 (1973) 691-694.

[58] L. Roizin-Towle and E. J. Hall, Studies with bleomycin and misonidazole on aerated and hypoxic cells, British Journal Cancer 37 (1978) 254.

[59] S. C. Barranco and D. R. Flournoy, Modification of the response to actinomycin D-induced sublethal damage by simultaneous recovery from potentially lethal damage in mammalian cells, Cancer Research 36 (1976) 1634-1640.

[60] Norma H. Rubin, Cacilda Casartelli, B. Gail Macik, W. R. Boerwinkle, and S.C. Barranco, *In vitro* cellular characteristic and survival responses of human astrocytoma clones to chloroethyl-nitrosoureas and dianhydrogalactitol, Investigational New Drugs 1 (1983) 129.

[61] James A. Belli and Anthony J. Piro, The interaction between radiation and adriamycin damage in mammalian cells, Cancer Research 37 (1977) 1624-1630.

[62] Gowhar Shafi, Anjana Munshi, Tarique N Hasan, Ali A Alshatwi, A Jyothy and David KY Lei, Induction of apoptosis in HeLa cells by chloroform fraction of seed extracts of Nigella sativa, Cancer Cell International 9:29 (2009) doi:10.1186/1475-2867-9-29.

[63] Vesna Todorovic, Gregor Sersa, Vid Mlakar, Damjan Glavac, Karel Flisar and Maja Cemazar, Metastatic potential of melanoma cells is not affected by electrochemotherapy, Melanoma Research 21 (2011) 196-205.

[64] Ioannis Alagkiozids, Andrea Facciabene, Marinos Tsiatas et al., Time-dependent cytotoxic drugs selectively cooperate with IL-18 for cancer chemoimmunotherapy, Journal of Translational Medicine 2011, 9:77.

[65] Sandeep Sanga, John P Sinek, Hermann B Frieboes, Mauro Ferrari, John P Fruehauf and Vittorio Cristini, Mathematical modeling of cancer progression and response to chemotherapy, Expert Review of Anticancer Therapy 6 (2006) 1361-1376.

[66] Ardith W. El-Kareh and Timothy W. Secomb, Two-mechanism peak concentration model for cellular pharmacodymics of doxorubicin, Neoplasia 7 (2005) 705-713.

[67] Ardith W. El-Kareh and Timothy W. Secomb, A mathematical model for cisplatin cellular pharmacodymics, Neoplasia 5 (2003) 161-169.

[68] Awad O, Yustein JT, Shah P, Gul N, Katuri V, et al., High ALDH Activity Identifies Chemotherapy-Resistant Ewing's Sarcoma Stem Cells That Retain Sensitivity to EWS-FLI1 Inhibition. PLoS ONE (2010) 5(11): e13943. doi:10.1371/journal.pone.0013943.

[69] Gentao Liu, Xiangpeng Yuan, Zhaohui Zeng et al., Analysis of gene expression and chemoresistance of $CD133^{+}$ cancer stem cells in glioblastoma, Molecular Cancer (2006) 5:67 doi:10.1186/1476-4598-5-67.

[70] Cosse JP, Michiels C, Tumor hypoxia affects the responsiveness of cancer cells to chemotherapy and promotes cancer progression, Anti-cancer Agents in Medical Chemistry 8 (2008) 790-797.

[71] Chiche J, Rouleau M, Gounon P, Brahimi-horn MC, Pouysséqur J, Mazure NM, Hypoxic enlarged mitochondria protect cancer cells from apoptotic stimuli, Journal of Cellular Physiology 222 (2010) 648-657.

[72] L. J. Liu, S. L. Brown, J. R. Ewing, M. Schlesinger, Phenomenological model of interstitial fluid pressure in a solid tumor, Physical Review E 84 (2011) 021919.

[73] Stephane Ferretti, Peter R. Allegrini, Mike M. Becquet and Paul M.J. McSheehy, Tumor interstitial fluid pressure as an early-response marker for anticancer therapeutics, Neoplasia 11 (2009) 874-881.

[74] Alexei V. Salnikov, Vegard V. Iversen, Markus Koisti, Christian Sundberg, Lars Johasson, Linda B. Stuhr, Mats Sjöquist, Hakan Ahlström, Rolf K. Reed, and Kristofer Rubin, Lowering of tumor interstitial fluid pressure specifically augments efficacy of chemotherapy, The FASEB Journal 17 (2003) 1756.

[75] Sarah Jane Lunt, Tuula MK Kalliomaki, Allison Brown, Victor X Yang, Michael Milosevic and Richard P Hill, Interstitial fluid, vascularity and metastasis in ectopic, orthotopic and spontaneous tumors, BMC Cancer 8: 2 (2008) doi:10.1186/1471-2407-8-2.c

[76] Einar K. Rofstad, Else-Beate M. Ruud, Berit Mathiesen, and Kanthi Galappathi, Associations between radiocurability and interstitial fluid pressure in human tumor xenografts without hypoxic tissue, Clinical cancer research 16 (2010) 936.

[77] Seung-Gu Yeo, Jun-Sang Kim, Moon-June Cho, Ki-Hwan Kim, and Jae-Sung Kim, Interstitial fluid pressure as a prognostic factor in cervical cancer following radiation therapy, Clinical cancer research 15 (2009) 6201.

[78] Terence P.F. Gade, Ian M. Buchanan, Matthew W. Motley, Yousef Mazaheri, William M. Spees, and Jason A. Koutcher, Imaging Intratumoral Convection: Pressure-Dependent Enhancement in Chemotherapeutic Delivery to Solid Tumors, Clinical cancer research 15 (2009) 247.

[79] Sarah Jane Lunt, Anthony Fyles, Richard P Hill & Michael Milosevic, Interstitial fluid pressure in tumors: therapeutic barrier and biomarker of angiogenesis, Future Oncolology 4 (2008) 793-802.

[80] Laurence T. Baxter and Rakesh K. Jain, Transport of fluid and macromolecules in tumors I. Role of interstial pressure and convection, Microvascular Research 37(1) (1989) 77-104.

[81] Y. Boucher, L. T. Baxter, and R. K. Jain, Interstitial pressure gradients in tissue-isolated and subcutaneous tumors: implications for therapy, Cancer Research 50 (1990) 4478-4484.

[82] Rakesh K. Jain, Ricky T. Tong, and Lance L. Munn, Effect of Vascular Normalization by Antiangiogenic Therapy on Interstitial Hypertension, Peritumor Edema, and Lymphatic Metastasis: Insights from a Mathematical Model, Cancer Research 67 (2007) 2729.

[83] Jani Pusenjak and Damijan Miklavcic, Modeling of interstitial fluid pressure in solid tumor, Simulation Practice and Theory 8 (2000) 17-24.

[84] Malisa Sarntinoranont, Frank Rooney, and Mauro Ferrari, Annals of Biomedical Engineering 31 (2003) 327-335.

[85] Wiig H, Tveit E, Hultborn R, Reed RK, and Weiss L. Interstitial fluid pressure in DMBA-induced rat mammary tumours, Scandinavian Journal of Clinical and Laboratory Investigation 42 (1982) 159-164.

[86] C Pozrikidis, DA Farrow, A model of fluid flow in solid tumors. Annals Biomedical Engineering 31 (2003) 181–194.

[87] C. Pozrikidis, Numerical simulation of blood and interstitial flow through a solid tumor, Journal of Mathematic Biology 60 (2010) 75-94.

[88] James W. Baish and Rakesh K. Jain, Fractals and cancers, Cancer Research 60 (2000) 3683.

[89] M. A. J. Chaplain, S. R. McDougall and A. R. A. Anderson, Mathematical modeling of tumor-induced angiogenesis, Annual Review Biomedical Engineering 8 (2006) 233-257.

[90] Matthew R. Dreher, Wenge Liu, Charles R. Michelich, Mark W. Dewhirst, Fan Yuan, Ashutosh Chilkoti, Tumor Vascular Permeability, Accumulation, and Penetration of Macromolecular Drug Carriers, Journal of the National Cancer Institute 98 (2006) 335.

[91] Raffi Karshafian, Peter N Burns and Mark R Henkelman, Transit time kinetics in ordered and disordered vascular trees, Physics in Medicine and Biology 48 (2003) 3225-3237.

[92] Maciej Z. Pindera, Hui Ding, Zhijian Chen, Convected element method for simulation of angiogenesis, Journal of Mathematical Biology 57 (2008) 467-495.

[93] Colombo F, Baldan F, Mazzucchelli S, Martin-Padura I, Marighetti P, et al. (2011) Evidence of Distinct Tumour-Propagating Cell Populations with Different Properties in Primary Human Hepatocellular Carcinoma. PLoS ONE 6(6): e21369. doi:10.1371/journal.pone.

[94] Isabel González-García, Richard V. Solé, and José Costa, Metapopulation dynamics and spatial heterogeneity in cancer, PNAS 99 (2002) 13085-13089.

[95] Philip Hahnfeldt, Dipak Panigrahy, Judah Folkman, and Lynn Hlatky, Tumor development under angiogenic signaling: A dynamical theory of tumor growth, treatment response, and postvascular dormancy, Cancer Research 59 (1999) 4770-4775.

[96] Aicha Demidem, Daniel Morvan, Janine Papon, Monique De Latour, and Jean Claude Madelmont, Cystemustine induces redifferentiation of primary tumor and confers protection against secondary tumor growth in a melanoma murine model, Cancer Research 61 (2001) 2294.

[97] Geoffrey B. West, James H. Brown, Brian J. Enquist, The fourth dimension of life: fractal geometry and allometric scaling of organisms, Science 284 (1999) 1677-1679.

[98] Geoffrey B. West, James H. Brown, Brian J. Enquist, A general model for the origin of allometric scaling laws in biology, Science 276 (1997) 122-126.

[99] Van M. Savage, Andrew P. Allen, James H. Brown, James F. Gillooly, Alexander B. Herman, William H. Woodruff, and Geoffery B. West, Scaling of number, size, and metabolic rate of cells with body size in mammals, The National Academy of Sciences of the USA 104 (2007) 4718-4723.

[100] K. Schmidt-Nielsen, Scaling: why is animal size so important, Cambridge University Press (1984), Cambridge.

[101] W. A. Calder III, Size, function and life history, Harvard university press (1984), Cambridge, MA.

[102] H. A. Feldman and T. A. McMahon, The 3/4 mass exponent for energy metabolism is not a statistical artefact, Respiration Physiology 52 (1983) 149.

[103] E. L. Charnov, Life History Invariants: Some Explorations of Symmetry in Evolutionary Ecology, Oxford Univ. Press (1993), Oxford.

[104] S. C. Stearns, The Evolution of Life Histories, Oxford Univ. Press (1992), Oxford.

[105] M. J. Reiss, The allometry of growth and reproduction, Cambridge Univ. Press (1989), Cambridge.

[106] L. von Bertalanffy, Quantitative laws in metabolism and growth, The Quarterly Review Biology 32 (1957) 217-231.

[107] Al-Hajj M,Wicha MS, Benito-Hernandez A, Morrison SJ, Clarke MF, Prospective identification of tumorigenic breast cancer cells, PNAS 100 (2003) 3983.

[108] Reya T, Morrison SJ, Clarke MF, Weissman IL, Stem cells, cancer, and cancer stem cells, Nature 414 (2001) 105-111.

[109] Lapidot T, Sirard C, Vormoor J, Murdoch B, Hoang T, Caceres-Cortes J, Minden M, Paterson B, Caligiuri MA, Dick JE, A cell initiating human acute myeloid leukaemia after transplantation into SCID mice, Nature 367 (1994) 645-648.

[110] Singh SK, Clarke ID, Terasaki M, Bonn VE, Hawkins C, Squire J, Dirks PB, Identification of a cancer stem cell in human brain tumors, Cancer Research 63 (2003) 5821-5828.

[111] George Pentheroudakis, Evangelos Briasoulis, Nicholas Pavlidis, Cancer of Unknown Primary Site: Missing Primary or Missing Biology? The Oncologist 12 (2007) 418-425.

[112] Evangelos Briasoulis and Nicholas Pavilidis, Cancer of unknown primary origin, The Oncologist 2 (1997) 142-152.

[113] Bernard Fisher, Nurten Gunduz, and Elizabeth A. Saffer, Influence of the interval between primary tumor removal and chemotherapy on kinetics and growth of metastases, Cancer Research 43 (1983) 1488-1492.

[114] K. H. Chadwick, and H. P. Leenhouts, A molecular theory of cell survival, Physics in Medicine and Biology 18 (1973) 78-87.

[115] G. W. Barendsen, C. J. Koot, G. R. van Kersen, D. K. Bewley, S. B. Field and C. J. Parnell, The effect of oxygen on impairment of the proliferative capacity of human cells in culture by ionizing radiations of different LET, International Journal of Radiation Biology 10 (1966) 317-327.

[116] Nicolas J. McNally, Jennifer de Ronde and Melvyn Folkard, Interaction between X-ray and α-particle damage in V79 cells, International Journal of Radiation Biology 53 (1988) 917-920.

[117] Tatiana Wenzl and Jan J Wilkens, Modelling of the oxygen enhancement ratio for ion beam radiation therapy, Physics in Medicine and Biology 56 (2011) 3251-3268.

[118] L. Hieber, G. Ponsel, H. Roos, S. Fenn, E. Fromke, and A. M. Kellerer, Absence of a dose-rate effect in the transformation of C3H 10T1/2 cells by α-particles, International Journal of Radiation Biology 52 (1987) 859-869.

[119] Lindsay A Beaton, Trevor Burn, Trevor J Stocki, Vinita Chauhan and Ruth C Wilkins, Development and characterization of an *in vitro* alpha radiation exposure system, Physics in Medicine and Biology 56 (2011) 3645-3658.

[120] M. Durante, G. F. Grossi, G. Gialanella, M. Pugliese, M. Nappo, T. C. Yang, Effects of α-particles on survival and chromosomal aberrations in human mammary epithelial cells, Radiation and Environmental Biophysics 34 (1995) 195-204.

[121] Stewart G. Martin, Richard C. Miller, Charles R. Geard and Eric J. Hall, The biological effectiveness of radon-progeny alpha particles. IV. Morphological transformation of Syrian hamster embryo cells at low doses, Radiation Research 142 (1995) 70-77.

[122] Patricia Thomas, Bliss Tracy, Tilly Ping, Anar Baweja, Mark Wickstrom, Narinder Sidhu and Linda Hiebert, Relative biological effectiveness (RBE) of alpha radiation in cultured porcine aortic endothelial cells, International Journal of Radiation Biology 83 (2007) 171-179.

[123] E. L. Lloyd, M. A. Gemmell, C. B. Henning, D. S. Gemmell, and B. J. Zabransky, Transformation of mammalian cells by alpha particles, International Journal of Radiation Biology 36 (1979) 467.

[124] Hongning Zhou, Gerhard Randers-Pehrson, Charles A. Waldren, Diane Vannais, Eric J. Hall, and Tom K. Hei, Induction of a bystander mutagenic effect of alpha particles in mammalian cells, PNAS 97 (2000) 2099-2104.

[125] Tom K. Hei, Li-Jun Wu, Su-Xian Liu. Diane Vannais, Charles A. Waldren, Mutagenic effects of a single and an exact number of α particles in mammalian cells, PNAS 94 (1997) 3765.

[126] Malgorzaza A. Walicka, G. Vaidyanathan, Michael R. Zalutsky, S. James Adelstein and Amin I. Kassis, Survival and DNA damage in Chinese hamster V79 cells exposed to alpha particles emitted by DNA-incorporated astatine-211, Radiation Research 150 (1998) 263-268.

[127] E. J. Hall, W. Gross, R. F. Dvorak, A. M. Kellerer, and H. H. Rossi, Survival curves and age response functions for Chinese hamster cells exposed to x-ray or high LET alpha-particles, Radiation Research 52 (1972) 88-98.

[128] H. C. Newman, K. M. Prise, M. Folkard and B. D. Michael, DNA double-strand break distributions in X-ray and α-particle irradiated V79 cells: evidence for non-random breakage, International Journal of Radiation Biology 71 (1997) 347-363.

[129] Detlef Blöcher, DNA double-strand break repair determines the RBE of α-particles, International Journal of Radiation Biology 54 (1988) 761-771.

[130] Alfredo Berruti, Paola Sperone, Elisa Bellini et al., Metronomic Therapy Concepts in the Management of Adrenocortical Carcinoma, Hormones and Cancer, DOI 10.1007/s12672-011-0087-1.

[131] G. Bocci, M. Tuccori, U. Emmenegger et al., Cyclophosphamide-methotrexate 'metronomic' chemotherapy for the palliative treatment of metastatic breast cancer: A comparative pharmacoeconomic evaluation, Annals of Oncology 16 (2005) 1243–1252.

[132] Rakesh K. Jain, Transport of molecules in the tumor interstitium: a review, Cancer Research 47 (1987) 3039.

[133] Helge Wiig, Olav Tenstad, Per Ole Iversen, Raghu Kalluri, and Rolf Bjerkvig, Interstitial fluid: the overlooked component of the tumor microenvironment? Fibrogenesis & Tissue Repair 3:12 (2010) doi: 10.1186/1755-1536-3-12.

[134] F. Stuart Foster, Peter N. Burns, David H. Simpson, Stephanie R. Wilson, Donald A. Christopher, David E. Goertz, Ultrasound for the visualization and quantification of tumor microcirculation, Cancer and Metastasis Review 19 (2000) 131-138.

[135] Adrianus J. de Langen, Vivian E. M. van den Boogaart, J. Tim Marcus, Mark Lubberink, Use of H215O-PET and DCE-MRI to measure tumor blood flow, The Oncologist 13 (2008) 631.

[136] Thomas P. Butler, Flora H. Grantham, and Pietro M. Gullino, Bulk transfer of fluid in the interstitial compartment of mammary tumors, Cancer Research 35 (1975) 3084-3088.

[137] Intae Lee, Yves Boucher, and Rakesh K. Jain, Nicotinamide can lower tumor interstitial fluid pressure: mechanistic and therapeutic implications, Cancer Research 52 (1992) 3237.

[138] Leunig M, Goetz AE, Gamarra F, Zetterer G, Messmer K and Jain RK, Photodynamic therapy-induced alterations in interstitial fluid pressure, volume and water content of an amelanotic melanoma in the hamster. British Journal of Cancer 69 (1994) 101-103.

[139] Kristine Gulliksrud, Kjetial G. Brurberg, Einar K. Rofstad, Dynamic contrast-enhanced magnetic resonance imaging of tumor interstitial fluid pressure, Radiotherapy and Oncology 91 (2009) 107-113.

[140] Yaron Hassid, Erez Eyal, Raanan Margalit, Edna Furman-Haran, Hadassa Degani, Non-invasive imaging of barriers to drug delivery in tumors, Microvascular Research 76 (2008) 94.

[141] Yaron Hassid, Edna Furman-Haran,Raanan Margalit, Raya Eilam, and Hadassa Degani, Noninvasive Magnetic Resonance Imaging of Transport and Interstitial Fluid Pressure in Ectopic Human Lung Tumors, Cancer Research 66 (2006) 4159.

[142] Masoom A. Haider, Igor Sitartchouk, Timothy P.L. Roberts, Anthony Fyles, Ali T Hashmi, and Michael Milosevic, Correlations Between Dynamic Contrast-Enhanced Magnetic Resonance Imaging–Derived Measures of Tumor Microvasculature and Interstitial Fluid Pressure in Patients with Cervical Cancer, Journal of Magnetic Resonance Imaging 25 (2007) 153-159.

[143] H Lyng, I Tufto, A Skretting and EK Rofstad, Proton relaxation times and interstitial fluid pressure in human melanoma xenografts. British Journal of Cancer 75 (1997) 180-183.

Appendices:

1. Introduction of several anticancer agents

1) Bleomycin—$C_{55}H_{84}N_{17}O_{21}S_3$

As an anticancer agent, bleomycin works mainly by inducing DNA strand breaks. The chemical structural formula is shown in Fig. A1. It is usually used in the treatment of squamous cell carcinomas and testicular cancer. It is also used in the treatment of plantar warts. When it is used as a component in the treatment of Hodgkin's lymphoma, it is combined with doxorubicin since these two drugs have an additive and complementary effect on DNA. In this case, doxorubicin acts by intercalating between DNA strands and on topoisomerase II enzyme for relaxing the topoisomerase complexes. The most serious side effects are pulmonary fibrosis and impaired lung function. Other side effects include: fever, rash, dermatographism, alopecia (hair loss) and Raynaud's phenomenon (discoloration of fingers and toes) [A1].

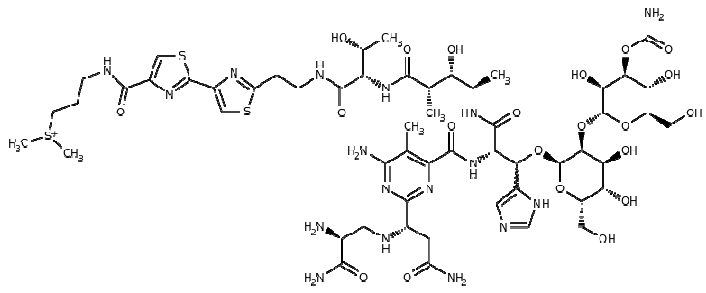

Fig. A1 Chemical structural formula of bleomycin [A1]

2) Actinomycin D—$C_{62}H_{86}N_{12}O_{16}$

Actinomycin D is one of the older chemotherapy drugs and most commonly used in treatment of a variety of cancers, including gestational trophoblastic neoplasia, Wilms' tumor and rhabdomyosarcoma. It is highly toxic and causes damage to genetic material, thus inhibiting cell proliferation [A2]. The chemical structural formula is shown in Fig. A2.

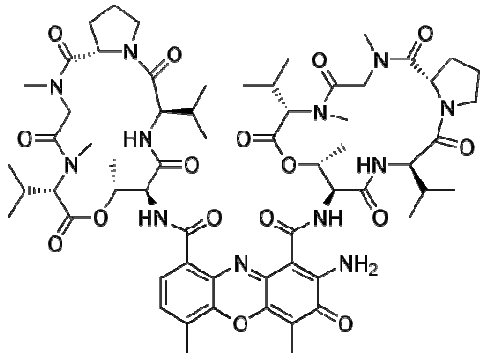

Fig. A2 Chemical structural formula of actinomycin D [A2]

3) BCNU—$C_5H_9C1_2N_3O_2$

Carmustine or BCNU (bis-chloroethynitrosourea) is used as an alkylating agent in chemotherapy. It is able to form interstrand crosslinks in DNA, which prevents DNA transcription. The chemical structural formula is shown in Fig. A3. It is used in the treatment of several brain cancers (such as glioma, glioblastoma multiforme, medulloblastoma and astrocytoma), multiple myeloma and lymphoma. Side effects include: pulmonary toxicity, hematologic toxicity, gastrointestinal toxicity, hepatotoxicity, and nephrotoxicity [A3].

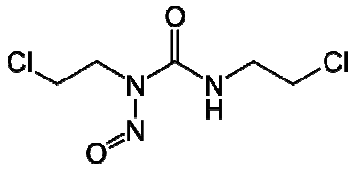

Fig. A3 Chemical structural formula of BCNU [A3]

4) MeCCNU—$C_{10}H_{18}C1N_3O_2$

Methyl-CCNU, 1-(2-chloroethyl)-3-(4-methylcyclohexyl)-1-nitrosourea (MeCCNU), has been used to treat malignant melanoma and cancer of the brain, lung, and digestive tract. It is an experimental tumorigen [A4]. The structural formula is shown in Fig. A4.

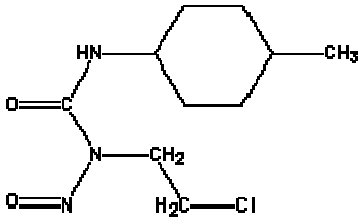

Fig. A4 Chemical structural formula of MeCCNU [A4]

5) PCNU—$C_8H_{11}C1N_4O_4$

PCNU is an alkylating chemotherapeutic agent. It inhibits DNA synthesis by alkylating DNA and causing DNA crosslinks. Side effects include pulmonary, hepatic and hematologic toxicities [A5]. The structural formula is shown in Fig. A5.

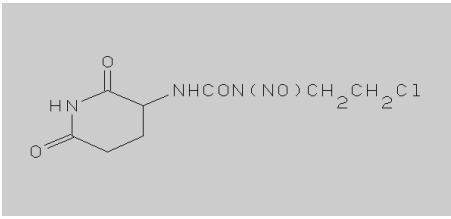

Fig. A5 Chemical structural formula of PCNU [A5]

6) CDDP –$PtC1_2(NH_3)_2$

CDDP (Cisplatin) is a chemotherapy drug. It is used to treat various types of cancers, including sarcomas, carcinomas such as small cell lung cancer and ovarian cancer, lymphomas, and germ cell tumors. The platinum complexes react *in vivo*, binding to and causing crosslinking of DNA, which ultimately triggers apoptosis (programmed cell death). Side effects are: Nephrotoxicity (kidney damage), which is a major concern; neurotoxicity; nausea and vomiting; ototoxicity (hearing loss); electrolyte disturbance; myelotoxicity (causing bone marrow suppression); and hemolytic anemia [A6]. The structural formula is shown in Fig. A6.

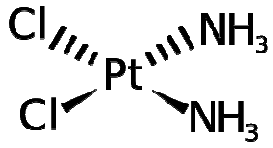

Fig. A6 Chemical structural formula of CDDP [A6]

7) Adriamycin (ADRM)—$C_{27}H_{29}NO_{11}$

Adriamycin is also named doxorubicin, a drug used in cancer chemotherapy. It works by intercalating DNA. It is commonly used in the treatment of a wide range of cancers, including hematological malignancies, many types of carcinoma, and soft tissue sarcomas. Its most serious adverse effect is life-threatening heart damage. It can also cause neutropenia, complete alopecia (hair loss), and discoloration of the urine (which can turn bright red for up to 48 hours after dosing). Due to the side effects and its red color, its nickname is “red devil” or “red death” [A7]. The structural formula is shown in Fig. A7.

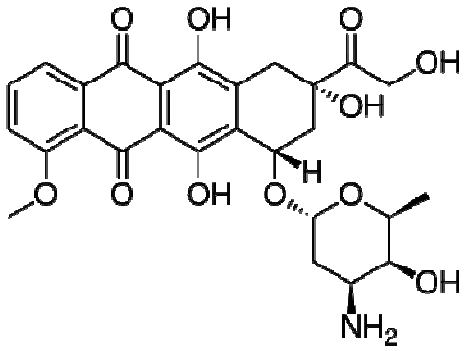

Fig. A7 Chemical structural formula of ADRM [A7]

2. Confluent hypergeometric function and the general solution for the equation of cell response to radiation and chemotherapy

Eq. (5.10) can be written as

$$\frac{dm}{dt}=\frac{EM^{1/4}}{C}m^{3/4}-\frac{\kappa n}{C}mt-\frac{E+\nu}{C}m \tag{A1}$$

Let $m^{1/4}=x$, so $m=x^4$, $dm/dt=4x^3dx/dt$. Eq. (A1) becomes

$$\frac{dx}{dt}=\frac{EM^{1/4}}{4C}-\frac{\kappa n}{4C}x(t+\frac{E+\nu}{\kappa n}) \tag{A2}$$

Let $t+\frac{E+\nu}{\kappa n}=T$, and $\frac{4C}{EM^{1/4}}x=X$, we have

$$\frac{dX}{dT}=1-\frac{\kappa n}{4C}XT=1-\eta XT \tag{A3}$$

where $\eta=\kappa n/(4C)$. Assume $X=\sum_{i=0}^{\infty}a_iT^i$ and substitute it in eq. (A3). We get

$$\sum_{i=0}^{\infty}a_iiT^{i-1}=1-\eta\sum_{i=0}^{\infty}a_iT^{i+1} \tag{A4}$$

Equivalently, $$a_1+\sum_{i=1}^{\infty}a_{i+1}(i+1)T^i=1-\eta\sum_{i=1}^{\infty}a_{i-1}T^i \tag{A4'}$$

By comparison, we have: $a_1=1$, and

$$(i+1)a_{i+1}=-\eta a_{i-1} \qquad (i=1, 2, 3, \ldots) \tag{A5}$$

Equivalently, $(2k+1)a_{2k+1}=-\eta a_{2k-1}$, $2ka_{2k}=-\eta a_{2k-2}$ $(k=1, 2, 3,\ldots)$ (A5')

For even terms,

$$\begin{cases} 2a_2=-\eta a_0 \\ 4a_4=-\eta a_2 \\ \vdots \\ 2ka_{2k}=-\eta a_{2k-2} \end{cases}$$

For odd terms,

$$\begin{cases} 3a_3=-\eta a_1 \\ 5a_5=-\eta a_3 \\ \vdots \\ (2k+1)a_{2k+1}=-\eta a_{2k-1} \end{cases}$$

$$a_{2k}=\frac{(-\eta)^k}{2^k k!}a_0 \qquad a_{2k+1}=\frac{(-\eta)^k}{(2k+1)!!}a_1 \tag{A6}$$

where $(2k+1)!!=1\cdot3\cdot5\cdots(2k+1)$ and $k=1,2,3\ldots$

Let $X = X_{even} + X_{odd}$

$$X_{even} = \sum_{k=0}^{\infty} a_{2k} T^{2k} = a_0 \sum_{k=0}^{\infty} \frac{1}{k!}\left(\frac{-\eta T^2}{2}\right)^k = a_0 \exp(-\eta T^2/2) \tag{A7}$$

$$X_{odd} = \sum_{k=0}^{\infty} a_{2k+1} T^{2k+1} = T\sum_{k=0}^{\infty} \frac{(-\eta)^k}{(2k+1)!!} T^{2k} = T\sum_{k=0}^{\infty} \frac{k!}{(k+1/2)!} \cdot \frac{(-\eta T^2/2)^k}{k!}$$

$$X_{odd} = T\sum_{k=0}^{\infty} \frac{(1)_k}{(3/2)_k} \cdot \frac{(-\eta T^2/2)^k}{k!} = T \cdot M(1, \frac{3}{2}, -\eta T^2/2) \tag{A8}$$

where $M(a,b,Z) = {}_1F_1(a,b,Z) = \sum_{k=0}^{\infty} \frac{(a)_k}{(b)_k} \cdot \frac{Z^k}{k!}$, $(a)_k = a(a+1)(a+2)\cdots(a+k-1)$ [A8, A9]

and $$M(a,b,Z) = \exp(Z) M(b-a, b, -Z)$$

$M(a, b, Z)$ is confluent hypergeometric function [A8, A9]. Therefore,

$$X = a_0 \exp(-\frac{\eta}{2} T^2) + T \cdot M(1, \frac{3}{2}, -\frac{\eta}{2} T^2) \tag{A9}$$

$$m = x^4 = \left(\frac{EM^{1/4}}{4C}\right)^4 X^4 = \left(\frac{EM^{1/4}}{4C}\right)^4 \cdot [a_0 \exp(-\frac{\eta}{2} T^2) + T \cdot M(1, \frac{3}{2}, -\frac{\eta}{2} T^2)]^4$$

$$m = \left(\frac{EM^{1/4}}{4C}\right)^4 \cdot \{a_0 \exp[-\frac{\kappa n}{8C}(t + \frac{E+\nu}{\kappa n})^2] + (t + \frac{E+\nu}{\kappa n}) M[1, \frac{3}{2}, -\frac{\kappa n}{8C}(t + \frac{E+\nu}{\kappa n})^2]\}^4$$

$$= \left(\frac{EM^{1/4}}{4C}\right)^4 \exp[-\frac{\kappa n}{2C}(t + \frac{E+\nu}{\kappa n})^2] \{a_0 + (t + \frac{E+\nu}{\kappa n}) M[\frac{1}{2}, \frac{3}{2}, \frac{\kappa n}{8C}(t + \frac{E+\nu}{\kappa n})^2]\}^4 \tag{A10}$$

When t=0, $T = \frac{E+\nu}{\kappa n}$, m=M_0, $X = \frac{4C}{E}\left(\frac{M_0}{M}\right)^{1/4}$. Therefore,

$$a_0 = \exp[\frac{(E+\nu)^2}{8C\kappa n}] \{\frac{4C}{E}\left(\frac{M_0}{M}\right)^{1/4} - \frac{E+\nu}{\kappa n} M[1, \frac{3}{2}, -\frac{(E+\nu)^2}{8C\kappa n}]\}$$

$$= \frac{4C}{E}\left(\frac{M_0}{M}\right)^{1/4} \exp[\frac{(E+\nu)^2}{8C\kappa n}] - \frac{E+\nu}{\kappa n} M[\frac{1}{2}, \frac{3}{2}, \frac{(E+\nu)^2}{8C\kappa n}] \tag{A11}$$

By calculating numerically through a program, we find if Z≥45,

$$M(1, \frac{3}{2}, -Z) \to \frac{1}{2Z}\left[\sum_{n=0}^{R-1} \frac{(1/2)_n}{Z^n} + O(1/Z^R)\right] \tag{A12}$$

Program for testing the Z of confluent hypergeometric function:

```
    Program ConfluentHyp
    implicit real*16 (a-h, o-z)
    Write (*,*) “Input of Z, should be greater than zero”
    Read (*,*) Z
    If (Z .LE. 0) Then
      Write (*,*)  'Z is less than 0'
      Stop
    End if
    call chf(z,nl1,ch1,nl2,ch2)
    open (1, file='chf.dat')
    write(1, 1000)z,nl1,CH1
    WRITE(1, 2000)NL2,CH2
1000 FORMAT(1X,F6.2,1X,I8,2X,D30.20)
2000 FORMAT(1X,7X,I8,2X,D30.20)
    END

    SUBROUTINE CHF(Z,NL1,CH1,NL2,CH2)
    IMPLICIT REAL*16 (A-H,O-Z)
    NL1=0
    NL2=0
    CH1=0.D0
    CH2=0.D0
    IF (Z.GT.30.D0) THEN
      S=1.0D0
      F=1.0D0
      NL=INT(Z)-1
      DO 10 N=1, NL
      F=(N-.5D0)*F/Z
      S=S+F
```

```
          IF(F/S.LT.1.D-20)THEN
            CH2=S/Z*.5D0
            NL2=N
            GO TO 15
          ENDIF
   10 CONTINUE
          NL2=NL
          CH2=S/Z*.5D0
   15 ENDIF
C**       IF(Z.GT.55) GO TO 80
          S=1.0D0
          F=1.0D0
          N=0
  100 N=N+1
          F=Z*F*(2*N-1)/(N+2*N*N)
          S=S+F
          IF(F/S.GT.1.D-20) GO TO 100
          NL1=N
          CH1=S*EXP(-Z)
   80 RETURN
          END
```

3. Principle of MRI

Magnetic resonance imaging (MRI), or nuclear magnetic resonance imaging (NMRI) [A10], applies the properties of nuclear magnetic resonance (NMR) in order to obtain images of atomic nuclei of tissues within the body. For a nucleus with a magnetic moment $\vec{\mu}$ and an angular momentum $\hbar\vec{I}$, there is a relation of $\vec{\mu} = \gamma\hbar\vec{I}$, where γ is a magnetogyric (or gyromagnetic) ratio and a nucleus-dependent constant [A11].

There is a fixed magnetic moment for a particular nucleus. Different kinds of nuclei have different magnetic moments. When there is no external magnetic field, the magnetic moment $\vec{\mu}$ distributes in random directions. The total magnetic moment is zero ($\sum\vec{\mu}_i = 0$). When there is an external magnetic field $\vec{B}_0$, the nuclei will be magnetized. They will gradually align to $\vec{B}_0$ (parallel or antiparallel to it). If we let $\vec{B}_0 = B_0\hat{z}$, then the energy level of each nucleus is determined by the equation

$$E = -\vec{\mu}\cdot\vec{B}_0 = -\gamma\hbar B_0 I_z = -m_I\gamma\hbar B_0 . \tag{A13}$$

$m_I = I, I-1, \cdots, -I$. The I is the nuclear spin.

Only nuclei with a specific number of protons and/or neutrons have a non-zero spin. 1) If the number of neutrons and the number of protons are both even, then the nucleus has a spin of zero; 2) If the number of neutrons plus the number of protons is odd, then the nucleus has a half-integer spin (i.e. 1/2, 3/2, 5/2); 3) If the number of neutrons and the number of protons are both odd, then the nucleus has an integer spin (i.e. 1, 2, 3).

In the human body, which is largely made of water (or matter that contains hydrogen), there are many hydrogen nuclei (protons). A proton has a spin of I=½, so m_I=±½. This means that the energy level splits into two levels (two energy eigenstates, known as the Zeeman effect) since it splits into 2I+1 levels ($\Delta E = \gamma\hbar B_0$), as shown in Fig. A8. If ΔE denotes the energy difference between the two levels, then

$$\hbar\omega_0 = \gamma\hbar B_0 , \quad \omega_0 = \gamma B_0 \tag{A14}$$

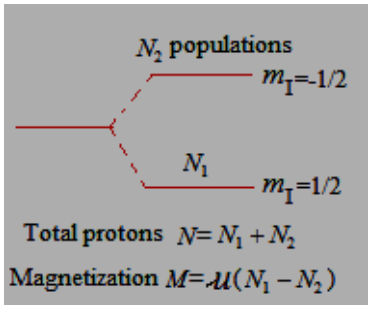

Fig. A8 Energy level splitting in a magnetic field

Eq. (A14) is the fundamental condition for magnetic resonance absorption. For protons,

γ=2.675×10^8($s^{-1}T^{-1}$), and $\upsilon(MHz)=\omega_0/2\pi=42.58B_0(Tesla)$.

The gyroscopic equation of nuclei in a magnetic field **B** is

$$\hbar\frac{d\vec{I}}{dt}=\vec{\mu}\times\vec{B} \qquad \text{or} \quad \frac{d\vec{\mu}}{dt}=\gamma\vec{\mu}\times\vec{B}=-\gamma\vec{B}\times\vec{\mu}=\vec{\omega}\times\vec{\mu} \tag{A15}$$

If a specimen is in a high magnetic field $\mathbf{B}_0$ long enough, protons in the sample will align themselves along the direction of the external magnetic field $\mathbf{B}_0$, creating a macroscopic nuclear magnetization. However, if perturbed magnetization is caused by an external field that is in a different direction to $\mathbf{B}_0$ (e.g. a perpendicular pulse $\mathbf{B}_1$), the magnetic moment of the magnetized nuclei and the total magnetic field **B** will be in different directions. Then, the magnetic moment of protons will precess about the total magnetic field **B**, which is shown by equation (A15). The frequency of precession is $\vec{\omega}=-\gamma\vec{B}$. We apply a uniform magnetic field $\mathbf{B}_0$, which is the principal field, as well as a radio frequency magnetic field $\mathbf{B}_1$. Then,

$$\vec{B}=\vec{B}_0+\vec{B}_1 \qquad (\boldsymbol{B}_1\perp\boldsymbol{B}_0) \tag{A16}$$

$$\vec{B}_0=B_0\hat{z} \qquad \vec{B}_1=\hat{x}B_1\cos\omega t-\hat{y}B_1\sin\omega t \qquad (B_0>>B_1) \tag{A17}$$

The precession frequency is approximately ω_0, which is mainly determined by $\mathbf{B}_0$ as shown in equation (A14).

For the effect of all nuclei in a magnetic field, the nuclear magnetization $\boldsymbol{M}$ is the sum $\Sigma\boldsymbol{\mu}_i$ over the total amount of nuclei in a unit volume.

$$\vec{M} = \sum_i \vec{\mu}_i \tag{A18}$$

If there is only one type of isotope, we have

$$\frac{d\vec{M}}{dt} = \gamma \vec{M} \times \vec{B} \tag{A19}$$

When there is a magnetic field $\mathbf{B}_1$, we get the equation

$$\vec{B} = \vec{B}_0 + \vec{B}_1 = B_0\hat{z} + \hat{x}B_1 \cos\omega t - \hat{y}B_1 \sin\omega t \qquad (B_0 >> B_1), \tag{A20}$$

All nuclei magnetons precess about $\mathbf{B}$ (~$\mathbf{B}_0$). When there is no $\mathbf{B}_1$ ($\mathbf{B}_1$ is a RF pulse), the nuclei are in a static field $\vec{B}_0 = B_0\hat{z}$. The magnetization will gradually restore itself to a state of equilibrium. At temperature T, the equilibrium magnetization is:

$$\vec{M} = M_0\hat{z} = \chi_0 B_0 \hat{z} \approx CB_0 / T\hat{z} \tag{A21}$$

where χ_0 is magnetic susceptibility and the Curie constant $C = N\mu^2 / k_B$. Here, N represents the number of protons in a unit volume.

More accurately, for nuclei with I=1/2, the equilibrium magnetization is

$$M_0 = (N_1 - N_2)\mu \tag{A22}$$

Considering the relation $N = N_1 + N_2$, and Boltzmann distribution

$$N_2 / N_1 = \exp(-2\mu B_0 / k_B T)\ ] \tag{A23}$$

We get

$$M_0 = N\mu \tanh(\mu B_0 / k_B T) \tag{A24}$$

At thermal equilibrium, the lower energy level will contain slightly more nuclei than the higher level due to small energy difference. It is possible to excite these nuclei into the higher level using electromagnetic radiation. Transitions between these two energy levels can be induced by applying an alternating magnetic field $\mathbf{B}_1$. When the radio frequency ω of $\mathbf{B}_1$ is adjusted so that it is the same as ω_0, which is given by equation (A14), resonance absorption of energy occurs and the maximum number of protons in the lower energy level can be excited to the higher level. When there is no RF magnetic field $\mathbf{B}_1$, the protons will recover to their thermal equilibrium. It is assumed that the rate of recovery is proportional to the rate of departure from the equilibrium value M_0. Therefore,

$$\frac{dM_z}{dt} = \frac{M_0 - M_z}{T_1} \tag{A25}$$

T_1 is called the longitudinal relaxation time or the spin-lattice relaxation time (the relaxation time describes the rate at which the nuclear spins to return to equilibrium).

If the frequency ω of the 90° pulse $\mathbf{B}_1$ is ω_0, the number of excited nuclei in the higher energy level reaches maximum (saturated state), and the protons are equally distributed in the two energy levels. The magnetization in the z-axis direction is zero (M_z=0). M_z will then gradually recover to M_0 after the pulse. Therefore,

$$M_z(t) = M_0[1 - \exp(-t / T_1)] \tag{A26}$$

With a pulse of $\mathbf{B}_1$, the total magnetic field becomes $\boldsymbol{B}(t)$=($B_x(t)$, $B_y(t)$, B_0+$B_z(t)$) and the magnetization is $\boldsymbol{M}(t)$=($M_x(t)$, $M_y(t)$, $M_z(t)$). Taking into account equation (A25), the z component of the equation of motion (A19) becomes [A11]

$$\frac{dM_z(t)}{dt} = \gamma[\vec{M}(t) \times \vec{B}(t)]_z + \frac{M_0 - M_z(t)}{T_1} \tag{A27}$$

The transverse magnetization component M_x (or M_y) will decay to zero when there is no $\mathbf{B}_1$, only $\mathbf{B}_0$. This is because M_x and M_y are zero at thermal equilibrium. Therefore [A11],

$$\frac{dM_x(t)}{dt} = \gamma[\vec{M}(t) \times \vec{B}(t)]_x - \frac{M_x(t)}{T_2} \tag{A28}$$

Similarly, $$\frac{dM_y(t)}{dt} = \gamma[\vec{M}(t) \times \vec{B}(t)]_y - \frac{M_y(t)}{T_2} \quad \text{(A29)}$$

T_2 is called the transverse relaxation time. It is a time constant that describes the rate of signal decay.

In a maintained field $\vec{B} = \vec{B}_0 + \vec{B}_1 = B_0\hat{z} + \hat{x}B_1 \cos\omega t - \hat{y}B_1 \sin\omega t$, the Bloch equations are:

$$\frac{dM_x(t)}{dt} = \gamma B_0 M_y(t) + \gamma B_1 M_z \sin\omega t - \frac{M_x(t)}{T_2}$$

$$\frac{dM_y(t)}{dt} = -\gamma B_0 M_x + \gamma B_1 M_z \cos\omega t - \frac{M_y(t)}{T_2}$$

$$\frac{dM_z(t)}{dt} = -\gamma B_1 (M_x \sin\omega t + M_y \cos\omega t) + \frac{M_0 - M_z(t)}{T_1}$$

Because $B_0 >> B_1$, we ignore the terms $\gamma B_1 M_x$ and $\gamma B_1 M_y$. The solutions of transverse components can be expressed as:

$M_x(t) = m\cos(\omega t + \varphi)$ and $M_y(t) = m\sin(\omega t + \varphi)$

$$\tan\varphi = -\frac{1}{(\omega_0 - \omega)T_2},$$

$$\cos\varphi = \frac{(\omega_0 - \omega)T_2}{[1 + (\omega_0 - \omega)^2 T_2^{\,2}]^{1/2}},$$

$$\sin\varphi = -\frac{1}{[1 + (\omega_0 - \omega)^2 T_2^{\,2}]^{1/2}}$$

$$m = \frac{\gamma B_1 M_z T_2}{(\omega_0 - \omega)T_2 \cos\varphi - \sin\varphi} = \frac{\gamma M_z T_2 B_1}{[1 + (\omega_0 - \omega)^2 T_2^{\,2}]^{1/2}}$$

After the pulse, the recovery process of M_z as well as the decay process of M_x and M_y are very important. They are used to form images of different tissues. When $\boldsymbol{B}_1$ ends, $\vec{B} = \vec{B}_0 = B_0\hat{z}$. Equations (A24), (A25) and (A26) are then reduced to

$$\frac{dM_x(t)}{dt} = \gamma B_0 M_y(t) - \frac{M_x(t)}{T_2};$$

$$\frac{dM_y(t)}{dt} = -\gamma B_0 M_x - \frac{M_y(t)}{T_2};$$

$$\frac{dM_z(t)}{dt} = \frac{M_0 - M_z(t)}{T_1}$$

$$M_x(t) = m\exp(-t/T_2)\cos\omega t;$$

$$M_y(t) = -m\exp(-t/T_2)\sin\omega t$$

$$M_z(t) = M_0 - [M_0 - M_z(0)]\exp(-t/T_1)$$

Due to the RF magnetic field $\mathbf{B}_1$, the power absorption is [A11]

$$P(\omega) = <\vec{B}_1 \cdot \frac{d\vec{M}}{dt}> = -\omega B_1 m\sin\varphi = \frac{\omega\gamma M_z T_2}{1+(\omega_0-\omega)^2 T_2^{\,2}} B_1^{\,2} \qquad \text{(A30)}$$

When $\omega=\omega_0$, resonance absorption of energy occurs. The resonance (maximum) power is

$$P_0 = P(\omega_0) = \omega_0\gamma M_z T_2 B_1^{\,2}$$

Based on equation (4.38), the half-width of the resonance at half-maximum power can be found as shown in Fig. A9:

$$\frac{\omega}{1+(\omega_0-\omega)^2 T_2^{\,2}} = \frac{\omega_0}{2} \quad \rightarrow \quad \frac{\omega_0 \pm \Delta\omega}{1+(\Delta\omega)^2 T_2^{\,2}} = \frac{\omega_0}{2}$$

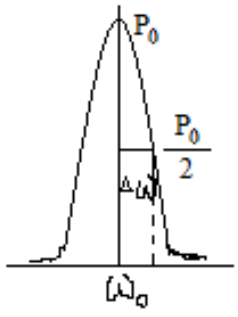

Fig. A9 Resonance power absorption

When $\Delta\omega << \omega_0$, we find that the half width of resonance is $\Delta\omega \approx 1/T_2$.

When we apply a 90° pulse $\mathbf{B}_1$ (which is perpendicular to $\mathbf{B}_0$), the total magnetic field (or effective field) is $\mathbf{B}_1$ at resonant frequency since $\omega_0 = \gamma B_0$.

$$\vec{B}_{eff} = (B_0 - \omega_0 / \gamma)\hat{z} + \hat{x}B_1 \cos\omega_0 t - \hat{y}B_1 \sin\omega_0 t = \vec{B}_1 \tag{A31}$$

In this case, the magnetization only exists in the xy plane, and $M_z(0) = 0$. It corresponds to the saturation situation where the proton population is the same on both energy levels. When there is no $\mathbf{B}_1$, the z-component M_z of magnetization will recover to its thermal equilibrium value M_0 with a time constant T_1. Equation (A26) shows the recovery process. In the meantime, the xy plane components, M_x and M_y, will decay to zero with a time constant T_2. Thus, T_1-weighted or T_2-weighted imaging can be used for better contrast.

When we apply a 180° pulse ($\mathbf{B}_1$//-$\mathbf{B}_0$), there will be no xy plane components for both magnetic field and magnetization (M_x=M_y=0). When there is no $\mathbf{B}_1$, M_z will recover to M_0 from -M_0. In this case, only T_1-weighed imaging can be applied [A12].

$$M_z(t) = M_0[1 - 2\exp(-t / T_1)] \tag{A32}$$

After a 90° RF pulse, the transverse magnetization components produce an oscillating magnetic field, as shown in Fig. A10 (a), which induces a small current in the receiver coil. This natural process of signal decay is called the Free Induction Decay (FID). In an idealized system, all nuclei precess with the same frequency in a fixed magnetic field (meaning there is no magnetic field gradient). Therefore, the FID signal decays to zero with a time constant T_2. However, in real systems, there are minor differences in the environment of nuclei, which cause a magnetic field gradient. In a practical MRI system, a magnetic field gradient can actually be applied for the sake of contrast. This can lead to a distribution of resonant frequencies around the ideal one. Over time, this distribution can lead to a dispersion of the tight distribution of magnetic spin vectors, and a loss of signal [A12].

$$\frac{1}{T_2^*} = \frac{1}{T_2} + \frac{1}{T_{in\,\mathrm{hom}}} = \frac{1}{T_2} + \gamma\Delta B_0 \tag{A33}$$

Here, γ represents the gyromagnetic ratio, and ΔB_0 is the difference in strength of the locally varying magnetic field. This process leads to a smaller decay time constant T_2^* than that under ideal conditions ($T_2^* < T_2$), and loss of signal due to phase dispersion. The time constant T_2 is important for spin echo sequences, while T_2^* is critical for gradient echo sequences. In practical MRI, T_2^*-weighted imaging uses the same concept as T_2-weighted imaging. The difference is that there is no 180° refocusing pulse in a T_2^*-weighted sequence. This means that T_2^*-weighting is a natural loss of phase coherence, resulting in an exponential T_2^* signal decay due to magnetic field inhomogeneities. In the T_2-weighted case, after a time period TE/2 of dephasing after the initial 90° RF pulse, a 180° RF pulse is applied. All protons are now flipped in phase and begin rephasing. After a time period TE, all spins are in phase again. Figs. A10 and A11 show the differences [A13, A14].

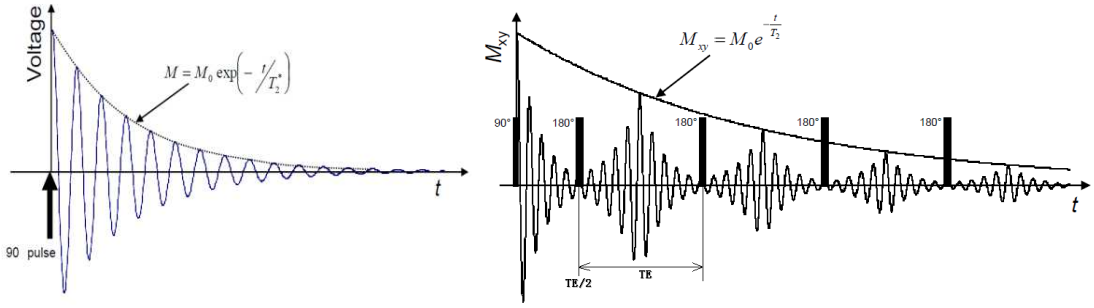

(a) T_2^*-weighting process (b) T_2-weighting process

Fig. A10 The difference between T_2^*-weighting process and T_2-weighting process

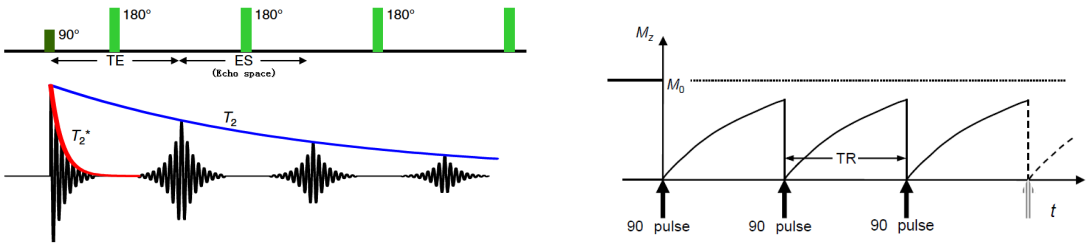

(a) Comparing T_2-weighting and T_2^*-weighting processes [A14] (b) T_1-weighting process [A13]

Fig. A11 The difference between T_1-weighting process and T_2-weighting process

The basic factor for determining the tissue brightness in an image is the number of hydrogen atoms (or protons), per unit volume of tissue, since the signal intensity after an RF pulse is proportional to the proton density in a scan with a long TR and a short TE. Weighting by relaxation time can be done by either short repetition time (TR) to give T_1-weighting, or by long echo time (TE) to give T_2-weighting.

T_1-weighted scans use a gradient echo sequence, with short echo time (TE) and short repetition time (TR). It indirectly measures the longitudinal magnetization by using a receiver coil to detect the voltage induced by the recovering longitudinal magnetization. Therefore, T_1 indirectly affects the amplitude of the signal, which reflects the brightness of the tissue in MRI. TR is chosen to give the best contrast. This is one of the basic ways of providing contrast, and is commonly used in clinical scanning. The T_1-weighting can be increased (thus improving contrast) with the use of an 180° pulse. Due to the short repetition time (TR), this scan can be run very quickly. For instance, T_1-weighted scans provide a good gray/white matter contrast in brain imaging.

T_2-weighted imaging creates image contrast (differences in tissue brightness) that depends on variations in T_2. After a 90° pulse, the magnetization lies in the *xy* plane and generates maximum voltage in the receiver coil. This voltage first dies away and then, if a 180° pulse is applied, reforms as an echo at time TE. The amplitude of the echo depends only on the T_2 of the tissue. T_2-weighted scans use a spin echo (SE) sequence, with long TE and long TR. They have long been the clinical workhorse, as the spin echo sequence is less susceptible to inhomogeneities in the magnetic field. They are particularly well suited to edema imaging since they are sensitive to water content.

T_2^*-weighted scans use a gradient echo sequence, with long TE and long TR. The gradient echo sequence does not have the extra refocusing pulse that exists in spin echo, so it is subjected to additional losses above the normal T_2 decay. All of these taken together are called T_2^*. This also makes it more prone to susceptibility losses at air/tissue boundaries, but can increase contrast for certain types of tissue, such as venous blood.

Spin (or proton) density weighted scans try not to have contrast from either T_2 or T_1 decay. The only signal change comes from differences in the amount of available spins

(hydrogen nuclei in water). It uses a spin echo, or sometimes a gradient echo sequence, with short TE and long TR.

Diseased tissues, such as tumors, can be detected because the protons in different tissues return to their equilibrium state at different rates. Changing the parameters on the scanner can create contrast between different types of body tissue. Careful design of the imaging pulse sequence allows one contrast mechanism to be emphasized while the others are minimized. In the brain, T_1-weighting causes the nerve connections of white matter to appear white, and the congregations of neurons of gray matter to appear gray, while cerebrospinal fluid (CSF) appears dark. The contrast of white matter, gray matter and cerebrospinal fluid is reversed using T_2 or T_2^* imaging, whereas proton-density-weighted imaging provides little contrast in healthy subjects. To improve image contrast, certain contrast agents may be used for particular tissues. For example, superparamagnetic contrast agents such as iron oxide nanoparticles appear very dark on T_2-weighted images and may be used for liver imaging. This is because normal liver tissue retains the agent, while abnormal areas such as scars and tumors do not. Additionally, functional parameters such as cerebral blood flow (CBF), cerebral blood volume (CBV) and blood oxygenation can affect T_1, T_2 and T_2^*, so they can be encoded with suitable pulse sequences.

In order to generate an image, it is necessary to measure the spatial variation of MR parameters, such as spin density and the spin-lattice relaxation time T_1. These measurements are made by degrading the uniformity of the static magnetic field so that the magnetization precesses at different frequencies. Therefore, there is a variation of resonant frequency across the sample. We may modify the uniformity of the field $\boldsymbol{B}_0$ by applying linear magnetic field gradients across the sample. In practice, a constant magnetic field gradient **G**(**r**) is applied in x, y and z directions, and encodes spins differently at varying locations by spatially modulating the Larmor frequency of protons. It is expressed as:

$$\vec{B}(\vec{r}) = \vec{B}_0 + \vec{G}(\vec{r}) \cdot \vec{r} \quad \text{and} \quad \omega_0(\vec{r}) = \gamma[B_0 + \vec{G}(\vec{r}) \cdot \vec{r}] \tag{A34}$$

For example, if a linear gradient in the z-direction is employed, the resulting magnetic field parallel to the uniform field is $B_z = B_0 + z\partial B_z / \partial z$. Therefore, the variation of the resonant frequency with regard to position is [A15]

$$\omega_0(z) = \gamma B_z = \gamma(B_0 + z\frac{\partial B_z}{\partial z}) = \gamma(B_0 + G_z z)$$

In this way, the detected signal contains spatial information. Conventionally, it is assumed that the region of interest has uniform sensitivity since signal excitation and detection are performed using a single RF channel. Therefore, the received signal can be expressed as [A16]:

$$S(t) \propto \int_{FOV} \rho(\vec{r}) e^{i\Delta\omega t} d\vec{r}$$

Here, FOV stands for the field of view; ρ (**r**) is the proton density at position **r**, and it is proportional to the number N(**r**) of protons in a unit volume; and $\Delta\omega$ is the frequency of **M** precessing about $\mathbf{B}_0$ in the rotating frame. Mathematically, $\Delta\omega = \omega_0 - \gamma B_0 = \gamma\vec{G}\cdot\vec{r}$.

The k-space (Fourier domain) transformation is very important for MRI signal processing. The MR signal $S(t)$ is generated by freely precessing nuclear spins in the presence of a linear magnetic field gradient **G**. It is the Fourier transform of the effective spin density, and is given by [A10, A15, A16]:

$$S(t) \equiv \int d\vec{r}\rho(\vec{r}) \exp[i\vec{k}(t)\cdot\vec{r}] \tag{A35}$$

where $\vec{k}(t) \equiv \gamma\int_0^t d\tau\vec{G}(\tau)$. For a linear magnetic field gradient (**G**=constant), $\vec{k} = \gamma\vec{G}t$.

From the basic k-space formula, we can reconstruct an image I(**r**) simply by taking the inverse Fourier transform of the sampled data:

$$I(\vec{r}) \equiv \int d\vec{k}S(\vec{k}(t)) \exp[-i\vec{k}(t)\cdot\vec{r}] \tag{A36}$$

In summary, Clinical Magnetic Resonance Imaging uses the magnetic properties of hydrogen and its interaction with both a large external magnetic field and radiowaves to produce highly detailed images of the human body. The body is largely composed of water molecules, each containing two hydrogen nuclei or protons. When a person goes inside the powerful magnetic field of the scanner, the magnetic moments of these protons

align with the direction of the field. A radio frequency electromagnetic field is then briefly turned on, causing the protons to alter their alignment relative to the field. As the RF pulse continues at a frequency around the resonant frequency ω_0, which is determined by equation (2), some of the spins in the lower energy state absorb energy from the RF field and make a transition into the higher energy state. This has the effect of "tipping" the net magnetization toward the transverse plane. When there is no RF field, the protons return to the original magnetization alignment. These alignment changes create a signal, which can be detected by the scanner. Because the frequency at which the protons resonate depends on the strength of the magnetic field, the position of protons in the body can be determined by applying an additional magnetic field during the scan, allowing an image of the body to be built up. This additional magnetic field is a gradient one, and we control it by turning gradient coils on and off while scanning (the gradient field is in the RF field rather than the static field).

The principle of signal detection is based on Faraday's law, which states that a varying magnetic field induces an electric field that can be detected by the receiver coil. In homogeneous media, the total magnetic field after a RF pulse is:

$$\vec{B}(\vec{r}) = B_0\hat{z} + G_x x\hat{x} + G_y y\hat{y} + G_z z\hat{z} + \mu_0\vec{M}(\vec{r}) \tag{A37}$$

where $\mathbf{B}_0$ is the primary magnetic field, while G_x, G_y and G_z are respectively the gradient coefficients of magnetic field along x, y and z-axes. $\mathbf{M}(\mathbf{r})$ is the magnetization of protons at position $\mathbf{r}$. When we use eq. (A35) to deal with the MRI signal, all modulating factors such as T_1/T_2-weighting and diffusion-weighting (which are all important for image contrast) are ignored [A16]. Also, MRI signal depends on the design of the receiver coil.

In order to better understand the principle of image contrast, we consider these factors and derive some formulae. The signal detected by the receiver coil can be expressed by Faraday's law. In a very small area, we take soft tissues to be homogeneous and use the average proton density to represent the proton density at that spot. This area is big enough in a microcosmic system, but small enough to be a small spot in a macrocosmic system.

$$V = \sum_i \oint E_i \cdot d\vec{l}_i = -\sum_i \iint (\partial\vec{B}_i / \partial t) \cdot d\vec{A}_i = -\sum_i \mu_0 \iint (d\vec{M}_i / dt) \cdot d\vec{A}_i \tag{A38}$$

The voltage of the received signal represents the intensity of the brightness of MRI images.

$$V_i = \mu_0 \iint d\vec{A} \cdot [m \exp(-\frac{t}{T_2})(\omega \sin \omega t + \frac{1}{T_2} \cos \omega t)\hat{x} + m \exp(-\frac{t}{T_2})(\omega \cos \omega t - \frac{1}{T_2} \sin \omega t)\hat{y}$$

$$+ \frac{M_0 - M_z(0)}{T_1} \exp(-\frac{t}{T_1})\hat{z}]$$

Since there is a gradient of magnetic field, M_0, m and the resonant frequency ω_0 are all spatially dependent. However, only at the resonant frequency ω_0 can m have the largest value. Therefore, just like a factor of delta function $\delta(\mathbf{R}\text{-}\mathbf{r})$, transverse magnetization M_{xy} has a large value only when the frequency is equal to or around ω_0. Due to the gradient of magnetic field $G_z(r)$, different places have different resonant frequencies $\omega_0(r)$. We can only detect a strong signal at or around the point with the resonant frequency. At any other place, the strength of the signal can be ignored. We introduce a weight factor η to express the effect of the signal in the resonance area. Therefore, based on the value of resonant frequency, we can locate where the signal originates from. This way, the computer system records the signal information point by point. Compared to B_0, the gradient is very small, so M_z may not change much spatially. The area of the receiver coil is fixed, but the direction is not. Therefore, we have:

$$V \approx \mu_0 A(\alpha\hat{x} + \beta\hat{y} + \gamma\hat{z}) \cdot [\eta M_z T_2 B_1 \exp(-\frac{t}{T_2})(\omega_0 \sin \omega_0 t + \frac{1}{T_2} \cos \omega_0 t)\hat{x}$$

$$+ \eta M_z T_2 B_1 \exp(-\frac{t}{T_2})(\omega_0 \cos \omega_0 t - \frac{1}{T_2} \sin \omega_0 t)\hat{y} + \frac{M_0 - M_z(0)}{T_1} \exp(-\frac{t}{T_1})\hat{z}] \quad \text{(A39)}$$

where α, β, and γ are the azimuth factors of the receiver coil. When the normal direction of the receiver coil is the same as the magnetization direction, the voltage of the coil reaches maximum.

$$V_{max} \approx \mu_0 A \cdot [(\eta M_z T_2 B_1)^2 \exp(-\frac{2t}{T_2})(\omega_0^2 + \frac{1}{T_2^2}) + \frac{M_0 - M_z(0)}{T_1^2} \exp(-\frac{2t}{T_1})]^{1/2} \quad \text{(A40)}$$

When the normal direction of the receiver coil is perpendicular to $\mathbf{B}_0$, then

$$V_{xy} = V_{\perp} \approx \mu_0 A \eta M_z T_2 B_1 \exp(-\frac{t}{T_2})(\omega_0^{\ 2} + \frac{1}{T_2^{\ 2}})^{1/2} \tag{A41}$$

When the normal direction of the receiver coil is parallel to $\mathbf{B}_0$, then

$$V_z = V_{//} \approx \mu_0 A \frac{M_0 - M_z(0)}{T_1} \exp(-\frac{t}{T_1}) \tag{A42}$$

The contrast between tissues "a" and "b" should be proportional to $\Delta V = V_a - V_b$.

$$(\Delta V_{xy})_{ab} = \mu_0 A \eta B_1 [M_{za} T_{2a} \exp(-\frac{t}{T_{2a}})(\omega_{0a}^{\ 2} + \frac{1}{T_{2a}^{\ 2}})^{1/2} - M_{zb} T_{2b} \exp(-\frac{t}{T_{2b}})(\omega_{0b}^{\ 2} + \frac{1}{T_{2b}^{\ 2}})^{1/2}] \tag{A43}$$

$$(\Delta V_z)_{ab} = \mu_0 A [\frac{M_{0a} - M_{za}(0)}{T_{1a}} \exp(-\frac{t}{T_{1a}}) - \frac{M_{0b} - M_{zb}(0)}{T_{1b}} \exp(-\frac{t}{T_{1b}})] \tag{A44}$$

By letting $d(\Delta V)/dt = 0$, we can discover at what time the image contrast is maximum. For T_1 or T_2 weighted process, if we take this time as the TE or TR, the optimal time is TE_0 or TR_0. This causes a maximum contrast between the two tissues. Usually, $M_z(0) = 0$, so

$$TE_0 = \frac{T_{2a} T_{2b}}{T_{2b} - T_{2a}} [\ln(\frac{M_{za}}{M_{zb}}) + \frac{1}{2} \ln(\frac{\omega_{0a}^{\ 2} + 1/T_{2a}^{\ 2}}{\omega_{0b}^{\ 2} + 1/T_{2b}^{\ 2}})] \tag{A45}$$

$$TR_0 = \frac{T_{1a} T_{1b}}{T_{1b} - T_{1a}} [\ln(\frac{M_{0a}}{M_{0b}}) + 2\ln(\frac{T_{1b}}{T_{1a}})] \tag{A46}$$

Correspondingly, the maximum contrast can be expressed as:

$$(\Delta V_{\perp ab})_{\max} = \mu_0 A \eta B_1 [M_{za} T_{2a} (\omega_{0a}^{\ 2} + \frac{1}{T_{2a}^{\ 2}})^{1/2} (\frac{M_{za}}{M_{zb}})^{\frac{T_{2b}}{T_{2b} - T_{2a}}} (\frac{\omega_{0b}^{\ 2} + 1/T_{2b}^{\ 2}}{\omega_{0a}^{\ 2} + 1/T_{2a}^{\ 2}})^{\frac{T_{2b}}{2(T_{2b} - T_{2a})}}$$

$$- M_{zb} T_{2b} (\omega_{0b}^{\ 2} + \frac{1}{T_{2b}^{\ 2}})^{1/2} (\frac{M_{za}}{M_{zb}})^{\frac{T_{2a}}{T_{2b} - T_{2a}}} (\frac{\omega_{0b}^{\ 2} + 1/T_{2b}^{\ 2}}{\omega_{0a}^{\ 2} + 1/T_{2a}^{\ 2}})^{\frac{T_{2a}}{2(T_{2b} - T_{2a})}}] \tag{A47}$$

$$(\Delta V_{//ab})_{\max} = \mu_0 A [\frac{M_{0a}}{T_{1a}} (\frac{M_{0b} T_{1a}^{\ 2}}{M_{0a} T_{1b}^{\ 2}})^{\frac{T_{1b}}{T_{1b} - T_{1a}}} - \frac{M_{0b}}{T_{1b}} (\frac{M_{0b} T_{1a}^{\ 2}}{M_{0a} T_{1b}^{\ 2}})^{\frac{T_{1a}}{T_{1b} - T_{1a}}}] \tag{A48}$$

In MRI, we use T_1 or T_2 weighting process and choose the TE and TR that give the best contrast, as shown in Fig. A12.

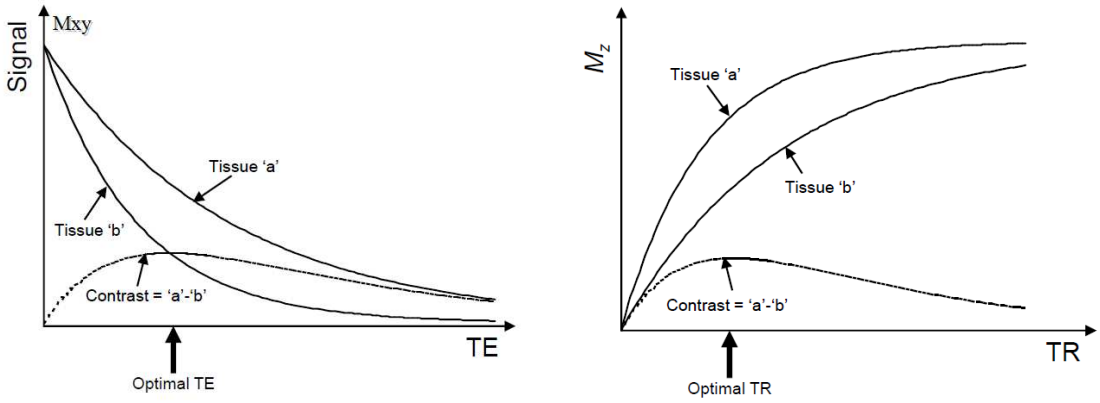

Fig. A12 Schematics of image contrast between tissue a and tissue b [A13]

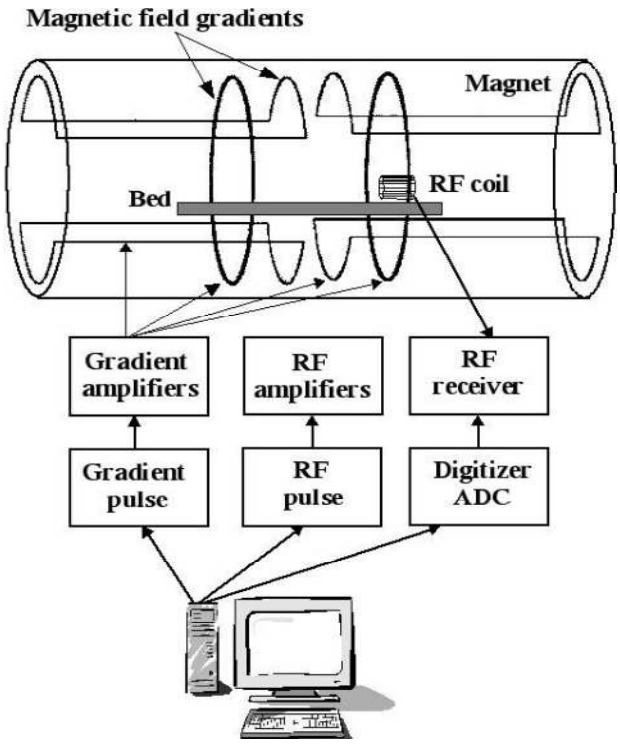

Fig. A13 Structure schematic of MRI [A15]

Rodríguez [A15] described the schematic structure of the MRI system concisely. An MRI system consists of five major components: a) a magnet, b) gradient systems, c) an RF coil system, d) a receiver, and e) a computer system. The structure schematic of MRI is shown in Fig. A13 [A15].

a) Magnet. The magnet aligns the nuclei into low energy (parallel) and high energy (anti parallel) states. Therefore, a strong magnet is necessary to generate a high magnetic field ($\boldsymbol{B}_0$), which should be uniform over a volume of interest. A high-field magnet provides better SNR resolution both in frequency and spatial domains. However, the main requirement for the $\boldsymbol{B}_0$ field is that its field uniformity should be very good. A few parts per million over a spherical volume, 50 cm in diameter, are required for a great variety of clinical applications. The optimal field strength and the type of magnet for imaging are dependent on the application, so permanent, resistive, or superconducting magnets may be used. For most clinical MRI systems, $\boldsymbol{B}_0$ varies from 0.05 to 3.0 Tesla, and permanent and superconducting magnets are mainly used. Superconducting magnets are made of a niobium-titanium alloy and are cooled to temperatures below 12 K by immersion in liquid helium, whose boiling point is 4.2 K. The main magnet rarely produces a field of sufficient uniformity by itself, so a shim system is necessary for maintaining the magnetic field homogeneity.

b) Gradient coils. All type of MRI modalities require deliberate alteration of field uniformity by applying a magnetic field gradient $G_z(r)$, which varies linearly with position r to spatially encode the NMR signal. Such gradients are generated by passing currents through specially arranged coils of wire, each placed on the former coil that surrounds the imaging subject. Three separate coils are needed in order to produce a linear variation of the z-component of the magnetic field along each of the three Cartesian directions. Many clinical MR systems are capable of producing 40mT.m^{-1} gradients to this end.

c) RF coil system. In MRI, it is necessary to irradiate the sample under test with an RF field ($\boldsymbol{B}_1$), in order to flip the magnetization away from its equilibrium state and generate a detectable NMR signal. This is usually done with an RF transmitter, which is responsible for pulse shape, duration, power, and timing (repetition rate). Since the

imaging subject is excited with an RF field, each spin produces a sinusoidal signal at a frequency dependent on the local magnetic field. To detect the signal coming from the spins, it is necessary for a device to couple the nuclei to some external circuitry. These devices are called RF coils/resonators/probes. RF coils can be divided into two main groups: volume and surface coils. Volume coils are typically cylindrical-shaped structures, and the most efficient volume coil at the present time is the so called bird-cage coil. Surface coils can be subdivided into single-loop coils and array coils (phased-array coils and array of independent coils for ultra-fast imaging schemes).

d) Receiver system. In order to convert the received RF signal from the RF coil into a form suitable for an analog-to-digital converter (ADC) or digitizer, some receiver circuitry is often employed. The signal is first amplified with a low noise amplifier, and then transmitted to a remote location to form an image via computer processing. The rest of the process involves signal demodulation using a superheterodyne style circuit. This is normally done with respect to the same frequency as the emitted RF radiation.

e) Computer system. This system represents the interface through which the user initiates measuring system functions (system test, display images, measure functions) and usually retrieves images. Particularly, for the reconstruction process, the computing requirement varies according to the imaging method used, but almost universally some form of Fourier transform (FT) is required. The best algorithm for FT is the fast Fourier transform (FFT), which can be used for two or three-dimensional images. The computer system should also be able to display images on a high-quality monitor.

4. DCE-MRI and DSC-MRI

The advanced applications of MRI include dynamic contrast enhanced magnetic resonance imaging (DCE-MRI), dynamic susceptibility contrast magnetic resonance imaging (DSC-MRI), and diffusion magnetic resonance imaging (Diffusion MRI).

Dynamic contrast enhanced magnetic resonance imaging (DCE-MRI) is a novel approach to the identification and assessment of tumors in living bodies. DCE-MRI scans show the flow of the contrast agent, and therefore the blood flow, between vascular space and extracellular extravascular space (EES) since the contrast agent is too large to enter the cells. Growth of a tumor depends on its ability to initiate formation of new blood vessels that can grow inside it—a process called angiogenesis. So tumors are regions of high blood flow and of high fraction of vascular space, and therefore can be detected via DCE-MRI. Also, DCE-MRI can assess tumor perfusion, microvascular vessel wall permeability and extravascular-extracellular volume fraction. Analysis of DCE-MRI data is usually based on indicator dilution theory, which requires knowledge of the concentration of the contrast agent in the blood plasma, which is the arterial input function (AIF). In T_1-weighted DCE-MRI, an intravenous bolus of gadolinium contrast agent enters tumour arterioles, passes through capillary beds and then drains via tumour veins. Gadolinium ions are paramagnetic and interact with nearby hydrogen nuclei to shorten T_1-relaxation times in local tissue water. This causes an increase in signal intensity of T_1-weighted images to a variable extent within each voxel. The degree of signal enhancement is dependent on physiological and physical factors, including tissue perfusion, arterial input function (AIF), capillary surface area, capillary permeability and the volume of the extracellular extravascular leakage space (EES). T_1-weighted DCE-MRI analysis generates parameters that represent one of, or combinations of these processes, and can be used to measure abnormalities in tumour vessel flow, blood volume, permeability, tortuosity and interstitial pressure.

A major goal in functional magnetic resonance imaging is to evaluate tissue perfusion, or fluid flow, and the exchange between tissues and blood, or vessel permeability. The theory is based on the fact that the solution can be expressed as a convolution of the

arterial input function (AIF) with a single exponential function. Based on Fick's principle [119],

$$\frac{dC_{tissue}(t)}{dt} = K_1 C_{plasma}(t) - k_2 C_{tissue}(t) \tag{A49}$$

C_{tissue} is the concentration of a flow tracer or contrast agent in tissue; K_1 is the plasma to tissue transport rate constant; C_{plasma}, AIF, is the tracer concentration in plasma; and k_2 is the tissue to plasma rate constant. C_{plasma} is effectively equal to C_{blood} because of the rapid exchange between blood cells and plasma [119]. This equation is depicted schematically in Fig. A14.

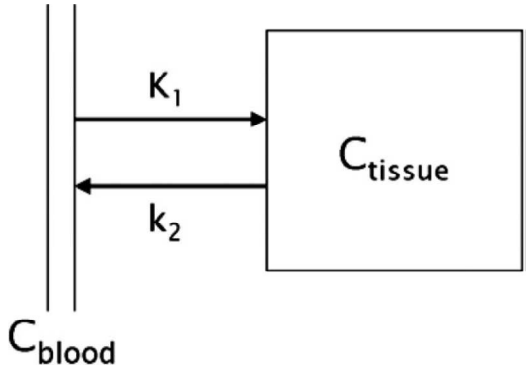

Fig. A14 Schematic of the relation between C_{tissue} and C_{blood} [119]

$$K_1 = E \cdot F = (1 - e^{-PS/F}) \cdot F \tag{A50}$$

E is the extraction fraction, F represents flow, P is the permeability and S is the surface. In DCE-MRI studies, K_1 is also called K^{trans} or K^{PS} (Volume transfer constant between plasma and EES). It is a function of blood flow (F), permeability (P), and the vascular surface (S). The term K^{trans} is generally used to describe the kinetics of contrast agents with a high PS product, thus mainly representing perfusion, whereas K^{PS} is used for contrast agents with a lower PS product and thus represents a mixed effect of perfusion and permeability. Equation (A13) can also be written as:

$$\frac{dC_{tissue}(t)}{dt} = K^{trans} C_{plasma}(t) - k_{ep} C_{tissue}(t) \qquad \text{(A51)}$$

Here, k_{ep} is the rate constant between EES and plasma, which is the ratio of the transfer constant to the EES ($k_{ep}=K_{trans}/v_e$). It represents the reflux coefficient or the transfer of contrast agent from tissue back to the blood. The solution of equation (A15) is

$$C_{tissue}(t) = (1 - fPV) \cdot K^{trans} \cdot \exp(-k_{ep} t) \otimes C_{plasma}(t) + fPV \cdot C_{plasma}(t) \qquad \text{(A52)}$$

Here, *fPV* is the fraction of plasma volume related to whole tissue volume.

Dynamic susceptibility contrast magnetic resonance imaging (DSC-MRI) uses rapid measurements of MR signal change following the injection of a bolus of a paramagnetic MRI contrast agent. The signal loss resulting from passage of this bolus, seen on T_2^*-weighted images, can be used to calculate the change in contrast concentration occurring in each pixel. These data can be used to produce calculated estimates of cerebral blood volume (CBV), mean transit time (MTT) and cerebral blood flow CBF. DSC-MRI is simple to perform in a clinical environment and is currently the most commonly used MR perfusion technique in clinical studies. The analysis of DSC-MRI data is based on the assumption that the contrast agent remains within the vascular space throughout the examination, acting as a blood pool marker. This assumption is untrue except within the brain, where there is no contrast leakage due to the blood–brain barrier (and in the testes where a similar barrier also exists). The application of DSC-MRI was therefore initially limited to studies of normal brain, although modifications of the technique have subsequently allowed its use in enhancing tissues. One of the main aims of DSC-MRI is the production of image based measurements of blood flow.

5. Program for calculating TIFP

```
Program TIFP distribution
Implicit none
Real :: Q, Qm, Qc, r0, p0, R1, p1, r, p  ! R1=R, p1=p(R)--the pressure of the environment.
Real :: A0, a, b, c, d, K, LL, AL, pL
Real, parameter :: pi=3.1415927
Print *, “Fluid flux at tumor edge Q=?”
Read *, Q
Print *, “Lymphatic drainage’ ability Qm=?”
Read *, Qm
Print *, “The critical flow rate Qc=?”
Read *, Qc
Print *, “The radius where fluid velocity is zero r0=?”
Read *, r0
Print *, “Pressure barrier p0=?”
Read *, p0
Print *, “Tumor radius R1=?”
Read *, R1
Print *, “Tumor pressure at the edge/environment p1=?”
Read *, p1
Print *, “The hydraulic conductivity of the interstitium K=?”
Read *, K
Print *, “The hydraulic conductivity of lymphatics LL=?”
Read *, LL
Print *, “Total surface area of the lymphatics with in radius rm AL=?”
! rm is the maximum radius that the fluid from the tumor can spread.
Read *, AL
Print *, “The pressure in lymphatics pL=?”
Read *, pL
A0=(Q-Qm)/(4*pi*K*R1**2)-LL*AL*(p1-pL)/(4*pi*K*R1**2)
a=(2*(p0-p1)-(R1-r0)*A0)/(R1-r0)**3
```

```
b=((R1+2*r0)*(R-r0)*A0-3*(R1+r0)*(p0-p1))/(R1-r0)**3
c=(6*R1*r0*(p0-p1)-r0*(R1-r0)*(2*R1+r0)*A0)/(R1-r0)**3
d=(R1**3*p0-r0**3*p1-3*R1*r0**2*p1+R1*r0**2*(R1-r0)*A0)/(R1-r0)**3
Print *, "r=?"
Read *, r
IF (r<=r0) Then
    Write(*,*)  "p=", p0
Else if (r>R1) Then
    Write(*,*)  "p=", pL+(Q-Qm)/LL*AL-((Q-Qm)/(LL*AL)-p1+pL)&
                    *exp(LL*AL*(1-R1/r)/(4*pi*K*R1))            !(r>R)
Else if (Qm>=Qc) Then
    Print *, "r=?"     ! r0<r<R
    Read *, r
    Write(*,*)  "p=", -p0*(r*r-2*r0*r+R1*(2*r0-R1))/(R1-r0)**2    !(r0<r<=R)
Else if (Qm>=Q .and. Qm<Qc) Then
    Print *, "r=?"     ! r0<r<R
    Read *, r
    Write(*,*)  "p=", -((p0-p1)*r*r-2*r0*(p0-p1)*r-R1**2*p0+2*R1*r0*p0-r0**2*p1)&
                    /(R1-r0)**2             !(r0<r<=R)
Else if (Q>Qm .and. Q<Qc) Then
    Print *, "r=?"     ! r0<r<R
    Read *, r
    Write(*,*)  "p=", a*r**3+b*r*r+c*r+d          !(r0<r<=R)
Else
     Write(*,*)  "not calculated"
End If
End Program
```

References

[A1] http://en.wikipedia.org/wiki/Bleomycin.

[A2] http://en.wikipedia.org/wiki/Actinomycin

[A3] http://en.wikipedia.org/wiki/Carmustine

[A4] http://www.iephb.nw.ru/~spirov/hazard/meccnu.html

[A5] http://dtpws4.ncifcrf.gov/data/compounds/95466.html

[A6] http://en.wikipedia.org/wiki/Cisplatin

[A7] http://en.wikipedia.org/wiki/Doxorubicin

[A8] John Pearson, Computation of Hypergeometric Functions, MSc. Thesis, University of Oxford, 2009.

[A9] Muller, K. (2001). Computing the confluent hypergeometric function, M(a, b, x), Numerische Mathematik 90(1), 179–196.

[A10] http://en.wikipedia.org/wiki/Magnetic_resonance_imaging.

[A11] Charles Kittel, Introduction to Solid State Physics, 8th edition, chap 13, John Wiley & Sons (2005) 361—390.

[A12] http://en.wikipedia.org/wiki/Relaxation_(NMR)

[A13] Mark A. Horsfield, Basis of MR contrast (MR Imaging in White Matter Diseases of the Brain and Spinal Cord / edited by Massimo Filippi, Nicola de Stefano, Vincent Dousset, Joseph C. McGowan), Springger-Verlag (2005), Berlin, Heidelberg.

[A14] M Lepage and J C Gore, Contrast mechanisms in magnetic resonance imaging, Journal of Physics: Conference Series 3 (2004) 78–86.

[A15] A. O. Rodríguez, Principle of magnetic resonance imaging, Revista Mexicana de FÍSICA 50 (2004) 272-286.

[A16] L. Ying, Zhi-Pei Liang, Parallel MRI using phased array coils, Signal Processing Magazine, IEEE 27 (2010) 90-98.

Vita Auctoris

NAME: Long Jian Liu

BORN: Sichuan, China, 1963

EDUCATION: Lanzhou University, Lanzhou, China

1982-1986 B. Sc.

Fudan University, Shanghai, China

1990-1993 M. Sc.

University of Windsor, Windsor, Canada

2007-2009 M. Sc.

2009-2012 Ph. D. Sc.